University of New Mexico
UNM Digital Repository

Nuclear Engineering ETDs | Engineering ETDs

12-9-1971

Techniques for Active 3He Activation Analysis for Carbon and Oxygen

William Mort Sanders

Follow this and additional works at: https://digitalrepository.unm.edu/ne_etds

 Part of the Nuclear Engineering Commons

www.manaraa.com

UNIVERSITY OF NEW MEXICO-UNIVERSITY LIBRARIES
A14429 092001

LD
3781
N564S.562
cop. 2

ACTIVE ^{3}HE ACTIVATION ANALYSIS

SANDERS

THE UNIVERSITY OF NEW MEXICO
ALBUQUERQUE, NEW MEXICO 87106

Policy on Use of Theses and Dissertations

Unpublished theses and dissertations accepted for master's and doctor's degrees and deposited in the University of New Mexico Library are open to the public for inspection and reference work. *They are to be used only with due regard to the rights of the authors.* The work of other authors should always be given full credit. Avoid quoting in amounts, over and beyond scholarly needs, such as might impair or destroy the property rights and financial benefits of another author.

To afford reasonable safeguards to authors, and consistent with the above principles, anyone quoting from theses and dissertations must observe the following conditions:

1. Direct quotations during the first two years after completion may be made only with the written permission of the author.

2. After a lapse of two years, theses and dissertations may be quoted without specific prior permission in works of original scholarship provided appropriate credit is given in the case of each quotation.

3. Quotations that are complete units in themselves (e.g., complete chapters or sections) in whatever form they may be reproduced and quotations of whatever length presented as primary material for their own sake (as in anthologies or books of readings) ALWAYS require consent of the authors.

4. The quoting author is responsible for determining "fair use" of material he uses.

This thesis/dissertation by Wm. Mort Sanders has been used by the following persons whose signatures attest their acceptance of the above conditions. (A library which borrows this thesis/dissertation for use by its patrons is expected to secure the signature of each user.)

NAME AND ADDRESS	DATE

July 1971—1,000—GS

This dissertation, directed and approved by the candidate's committee, has been accepted by the Graduate Committee of The University of New Mexico in partial fulfillment of the requirements for the degree of

DOCTOR OF PHILOSOPHY

TECHNIQUES FOR ACTIVE ^{3}He ACTIVATION ANALYSIS FOR CARBON AND OXYGEN

Title

Wm. Mort Sanders

Candidate

NUCLEAR ENGINEERING

Department

Charles L. Bechel

Dean

December 9, 1971

Date

Committee

Glen A. Cox

Chairman

Harold D. Southward

Dale M. Hahn

Morris E. Battat

TECHNIQUES FOR ACTIVE ^{3}He ACTIVATION ANALYSIS FOR CARBON AND OXYGEN

BY
WM. MORT SANDERS

B.S., Kansas State University, 1961
M.S., University of New Mexico, 1966

DISSERTATION

Submitted in Partial Fulfillment of the
Requirements for the Degree of
Doctor of Philosophy in Nuclear Engineering
in the Graduate School of
The University of New Mexico
Albuquerque, New Mexico
December, 1971

UNIVERSITY OF NEW MEXICO LIBRARY

LD
3781
N564Sa562
cop. 2

ACKNOWLEDGMENTS

I am grateful to Drs. Barry K. Barnes, Frank W. Clinard, Jr., Dale M. Holm, and Morris E. Battat of the Los Alamos Scientific Laboratory and Drs. Glenn A. Whan and Harold D. Southward of the University of New Mexico for their counsel, assistance, and guidance during the course of this research.

I wish also to thank the Los Alamos Scientific Laboratory for the assistance given by its professional staff (particularly those members of Groups K-1, J-12, P-9, T-1, and C-1 that contributed to this effort) and for the equipment that was used. I am very grateful to Mrs. Paul Robyn and Mrs. Maynard E. Smith for their assistance in the preparation and typing of the manuscript, to Mr. James Witkovic for his assistance with the illustrations, and to the Operations Staff at the Van de Graaff for their patience and help during the irradiations.

596271

TECHNIQUES FOR ACTIVE ^{3}He ACTIVATION ANALYSIS FOR CARBON AND OXYGEN

BY
WM. MORT SANDERS

B.S., Kansas State University, 1961
M.S., University of New Mexico, 1966

ABSTRACT OF DISSERTATION

Submitted in Partial Fulfillment of the
Requirements for the Degree of
Doctor of Philosophy in Nuclear Engineering
in the Graduate School of
The University of New Mexico
Albuquerque, New Mexico
December, 1971

ABSTRACT

The surface and body concentrations of carbon and oxygen have been measured in various materials using ^{3}He activation. Channeling techniques have been used to differentiate between interstitial and substitutional location of these impurities.

Thin target excitation functions were determined for (^{3}He,p) reactions with carbon and oxygen over a ^{3}He energy range from 2.5 to 9.0 MeV. These data were used to calculate the activation curves for various combinations of incident particle energy, impurity distributions, and material.

Information on several computer codes used during this study is presented.

TABLE OF CONTENTS

	Page
LIST OF FIGURES	ix
LIST OF TABLES	xiii
CHAPTER	
I. INTRODUCTION	1
II. EXPERIMENTAL PROCEDURE	8
Introduction	8
Sample Preparation	8
Experimental Area at the Van de Graaff	10
Alignment of Germanium Crystals	17
III. CALIBRATION USING PASSIVE ANALYSES	25
Introduction	25
Data Acquisition	26
Decay Curve Analysis	32
Calculation of the Target Thicknesses	35
Prompt Proton Data	38
Results	41
IV. CALCULATIONS AND DATA ANALYSIS	42
Introduction	42
Energy Loss Calculations	43
Thin Target Excitation Functions	44
Nuclear Energy Levels	48
Interpolation and Smoothing with Cubic Splines	60
Nuclear Reaction Kinematics	62
V. CHANNELING	67
Introduction	67
Channeling Experiments with Single-Crystal Thoria	68

TABLE OF CONTENTS - continued

	Page
VI. RESULTS	78
Introduction	78
Thick Target Calculations	78
Thin Oxygen Calibration Data	81
Thick Carbon and Oxygen Samples	84
Activation Analysis of Tantalum	87
Channeling Irradiations	90
Errors	98
VII. CONCLUSIONS	100
APPENDIX	
A. DECAY CURVE ANALYSIS CODE	103
Main Program DECURA	104
Subroutine BSS	105
Subroutine DINSET	105
Live-Time Calculation	106
Input Formats and Data	106
Subroutine MAZGN	110
Subroutine OUTGN	112
Subroutine PHICAL	112
Subroutine PLOTGN	114
Subroutine YP	116
Sample Problem	116
B. SURFACE AND VOLUMETRIC CONCENTRATIONS FROM CHARGED-PARTICLE ACTIVATION CODE	127
Main Program SVCCPA	127
Function GFN(A,C,D,E)	131
Subroutine FSIGE	134
Subroutine TFOX	134
Sample Problem	135
C. GAUSSIAN WITH HIGH AND LOW EXPONENTIAL TAILS FIT CODE	141
Main Program GHLET	141
Subroutine DATA	141
Subroutine DINSET	142
Subroutine MAZCS	144
Subroutine OUTCS	145
Subroutine PLTZ	146
Subroutine SITRE	146
Subroutine YP	146
Sample Problem	147

TABLE OF CONTENTS - continued

	Page
APPENDIX	
D. C24HE3P COMPUTER CODE	153
Main Program C24HE3P	153
Subroutine DATAIN	154
Subroutine LSRMZ	157
Subroutine OUTRAN	157
Subroutine PHICAL	157
Subroutine PIONIZ	157
Subroutine PLTZ	157
Subroutine PROMPT	158
Subroutine PRTNEY	158
Subroutine YP	160
Sample Problem	160
E. INTERPOLATORY CUBIC SPLINES	166
REFERENCES	169
CURRICULUM VITAE	173

LIST OF FIGURES

Figure		Page
1.	Classical coulomb barriers for ^{3}He reactions.	2
2.	^{3}He energy and total oxygen activation cross section versus sample depth for 7-MeV ^{3}He particles incident randomly on germanium.	4
3.	Proton spectrum from the irradiation of a germanium crystal after its surface was allowed to oxidize in air.	11
4.	Proton spectrum from the irradiation of a germanium crystal that was etched and then dried in a vacuum prior to the irradiation.	11
5.	The beam tube and experimental area at the Van de Graaff that was used for the ^{3}He irradiations.	12
6.	Close-up view of one of the slit assemblies and its viewing port.	13
7.	View of the goniometer and the mechanical feed-throughs used for crystal orientation.	16
8.	Schematic drawing of the standard target chamber.	18
9.	Schematic drawing showing the wiring and electronic equipment used in the Van de Graaff control room.	19
10.	Plot of the backscattered ^{3}He pulse-height distribution from the irradiation of a germanium crystal in a nonchanneling orientation.	20
11.	Plot of the backscattered ^{3}He pulse-height distribution from the irradiation of a germanium crystal in a channeling orientation.	20
12.	Data obtained during the alignment of a germanium crystal.	22
13.	Plot of the count rate from the high-energy backscattered ^{3}He as the goniometer was rotated across the $\langle 111 \rangle$ axis of a germanium crystal.	24
14.	Large 4π NaI(Tl) detector system.	27
15.	Schematic diagram of the electronics used with the 4π detector system.	28
16.	Background from the 4π detector system.	30

Figure		Page
17.	Spectrum from ^{3}He irradiated carbon sample placed in the 4π detector system.	31
18.	Unfolded complex decay curve from activated carbon sample.	34
19.	Analytical representation of the $^{12}C(^{3}He,\alpha)^{11}C$ cross section.	36
20.	Prompt proton pulse-height distribution from the carbon activation.	39
21.	Prompt proton pulse-height distribution from the oxygen activation.	40
22.	Proton and ^{3}He energy loss in germanium.	45
23.	Proton spectrum from the thin carbon calibration sample.	46
24.	Proton spectrum from the thin oxygen calibration sample.	47
25.	Excitation functions for the ground state through the 3rd excited state for the $^{12}C(^{3}He,p)^{14}N$ reaction.	49
26.	Excitation functions for the 4th through 7th excited states for the $^{12}C(^{3}He,p)^{14}N$ reaction.	50
27.	Excitation functions for the 8th and 9th excited states for the $^{12}C(^{3}He,p)^{14}N$ reaction.	51
28.	Excitation functions for the ground state through the 3rd excited state for the $^{16}O(^{3}He,p)^{18}F$ reaction.	52
29.	Excitation functions for the 4th through 7th excited states for the $^{16}O(^{3}He,p)^{18}F$ reaction.	53
30.	Excitation functions for the 8th through 11th excited states for the $^{16}O(^{3}He,p)^{18}F$ reaction.	54
31.	Excitation functions for the 12th through 15th excited states for the $^{16}O(^{3}He,p)^{18}F$ reaction.	55
32.	Excitation functions for the 16th through 19th excited states for the $^{16}O(^{3}He,p)^{18}F$ reaction.	56
33.	Prompt gamma-ray spectrum from a carbon irradiation.	57
34.	Prompt gamma-ray spectrum from an oxygen irradiation.	59
35.	Pulse-height distribution that was smoothed with cubic splines.	61

Figure		Page
36.	Reaction kinematics for experimental geometry.	63
37.	Reaction proton energy versus ^{3}He energy for the $^{12}C(^{3}He,p)^{14}N$ reaction at 160°.	65
38.	Reaction proton energy versus ^{3}He energy for the $^{16}O(^{3}He,p)^{18}F$ reaction at 160°	66
39.	Ion paths in an ordered lattice.	69
40.	Pulse-height distributions from ^{3}He particles backscattered by copper and oriented single-crystal thoria.	71
41.	Channeling dip for the $\langle 111 \rangle$ axis of thoria from backscatter techniques.	73
42.	Background pulse-height distributions from the copper mask.	75
43.	Pulse-height distributions from oriented single-crystal thoria.	76
44.	Analysis of prompt proton spectrum from a thin oxygen sample using the IMP code.	83
45.	Analysis of prompt proton spectrum from a thick carbon sample using the IMP code.	85
46.	Analysis of prompt proton spectrum from a thick oxygen sample using the IMP code.	86
47.	Unfolded prompt proton spectrum from a ^{3}He irradiated calcite sample.	88
48.	Unfolded prompt proton spectrum from a tantalum activation sample.	89
49.	Ratio of channeling to nonchanneling ^{3}He backscatter pulse-height distributions from irradiations along the $\langle 111 \rangle$ axis of single-crystal thoria.	91
50.	Ratio of channeling to nonchanneling ^{3}He backscatter pulse-height distributions from irradiations along the $\langle 110 \rangle$ axis of single-crystal thoria.	92
51.	Ratio of channeling to nonchanneling prompt proton pulse-height distributions from irradiations along the $\langle 111 \rangle$ axis of single-crystal thoria.	93
52.	Ratio of channeling to nonchanneling prompt proton pulse-height distributions from irradiations along the $\langle 110 \rangle$ axis of single-crystal thoria.	94

Figure		Page
53.	Unfolded prompt proton spectrum from the nonchanneling irradiation of single-crystal germanium.	96
54.	Unfolded prompt proton spectrum from the channeling irradiation of single-crystal germanium along the ⟨111⟩ axis.	97
55.	Basic assumptions for the cubic spline problem.	167

LIST OF TABLES

Table		Page
1.	NUCLEAR REACTIONS, THEIR HALF-LIVES AND Q VALUES	25
2.	RESULTS FROM ANALYSIS OF CARBON ACTIVATION SAMPLE	35
3.	RESULTS OF PASSIVE CALIBRATION	41
4.	NUCLEAR LEVELS IN ^{14}N AND ^{18}F	58
5.	PARAMETERS FOR LEAST-SQUARES ANALYSIS	82
6.	CARBON AND OXYGEN CONCENTRATIONS IN TANTALUM	87
7.	GERMANIUM ACTIVATIONS	98
8.	POSSIBLE INTERFERENCE REACTIONS	101
9.	MAIN PROGRAM DECURA VARIABLES	105
10.	SUBROUTINE DINSET VARIABLES	107
11.	SUBROUTINE MAZGN VARIABLES	111
12.	SUBROUTINE OUTGN VARIABLES	113
13.	SUBROUTINE PHICAL VARIABLES	114
14.	SUBROUTINE PLOTGN VARIABLES	115
15.	SUBROUTINE YP VARIABLES	116
16.	MAIN PROGRAM SVCCPA VARIABLES	132
17.	BOUNDS ON PARAMETERS MAZCS	145
18.	REACTIONS DEFINED IN C24HE3P CODE	153
19.	LIST OF VARIABLES IN PIONIZ SUBROUTINE	158
20.	LIST OF VARIABLES IN PROMPT SUBROUTINE	159
21.	LIST OF VARIABLES IN PRTNEY SUBROUTINE	159

CHAPTER I

INTRODUCTION

Carbon and oxygen, two common low-Z impurities that are found in metals and semiconductors, can influence the behavior of these materials. For example, oxygen impurities greatly affect the manufacture of large Ge(Li) detectors from germanium (Ref. 1). Techniques need to be developed that will allow the experimenter to determine the distribution and concentration of these impurities in materials. The ^{3}He-induced nuclear reactions with carbon and oxygen and their subsequent reaction products present several ways of studying the distributions and concentrations of these impurities. These include the prompt emission of charged particles, the prompt emission of gamma rays, and the delayed positron and gamma-ray emission of the reaction products. In general, nuclear reactions are not sensitive to the chemical composition of the impurity and can be quite selective if the proper reaction and irradiation parameters are used.

The ^{3}He reactions and other charged-particle reactions have been used by many experimenters in activation analysis work (Refs. 2-6). The coulomb electrostatic repulsion of high-Z nuclei effectively prevents interaction between them and the ^{3}He particles. Thus, small concentrations of low-Z impurities, which do allow nuclear interactions, may be studied in the presence of large amounts of high-Z materials. The classical coulomb barrier vs the atomic number is shown in Fig. 1. It should be noted, however, that some activation is obtained at particle energies below the classical barrier due to tunneling effects.

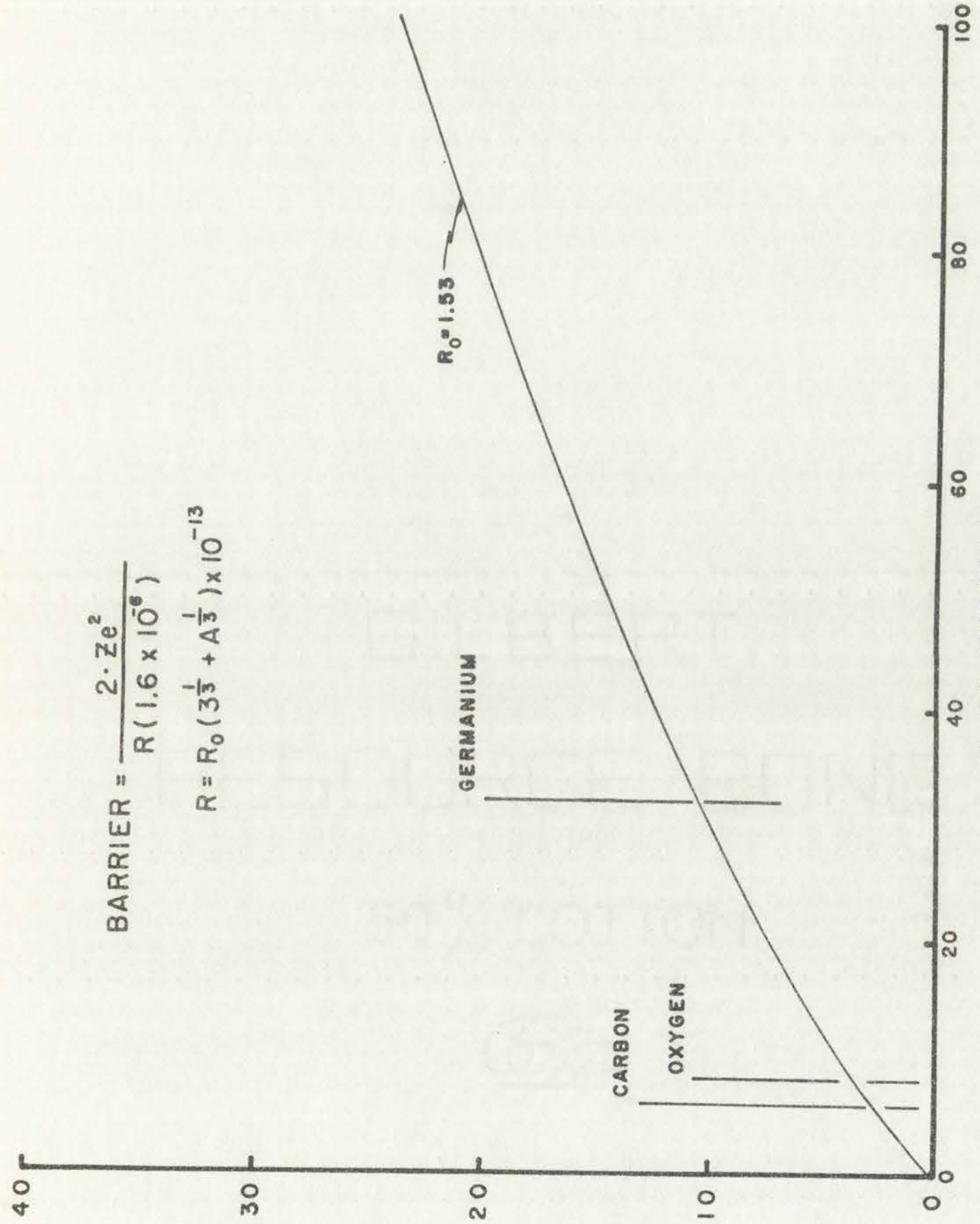

Fig. 1. Classical coulomb barriers for ^{3}He reactions.

There are several other reasons why ^{3}He is attractive for studying low-Z impurities in a high-Z matrix or substrate:

1. ^{3}He does not have an excess of neutrons; therefore, complicating secondary reactions from (^{3}He,n) reactions are not common as for (d,n) and (t,n) reactions;
2. ^{3}He has a low binding energy that leads to energetic reactions in which the reaction products have high kinetic energies;
3. The short range of the ^{3}He particles makes them particularly suitable for measuring surface concentrations and distributions. However, this may be a detriment if one is interested in measuring the bulk concentration of the impurity and the distribution of the impurity is not uniform throughout the material; and
4. The background associated with the prompt charged-particle activation analysis techniques is extremely low.

The total ^{16}O to ^{18}F cross section and the average ^{3}He energy vs sample penetration are shown in Fig. 2 for a 7 MeV ^{3}He irradiation of germanium in a nonchanneling orientation. Recoil and energy straggling effects have been ignored. The cross section has decreased to half its peak value at 10 μ. There is essentially no activation at sample depths exceeding 25 μ. ^{3}He activation and autoradiographic techniques have been used for studying the surface concentrations and distributions of carbon and oxygen on various materials (Ref. 7). Similar activation techniques were used to determine the carbon gradient from a carburized stainless steel sample (Ref. 8).

Variations in the surface distributions and surface gradients can cause discrepancies in activation analysis results with charged particles.

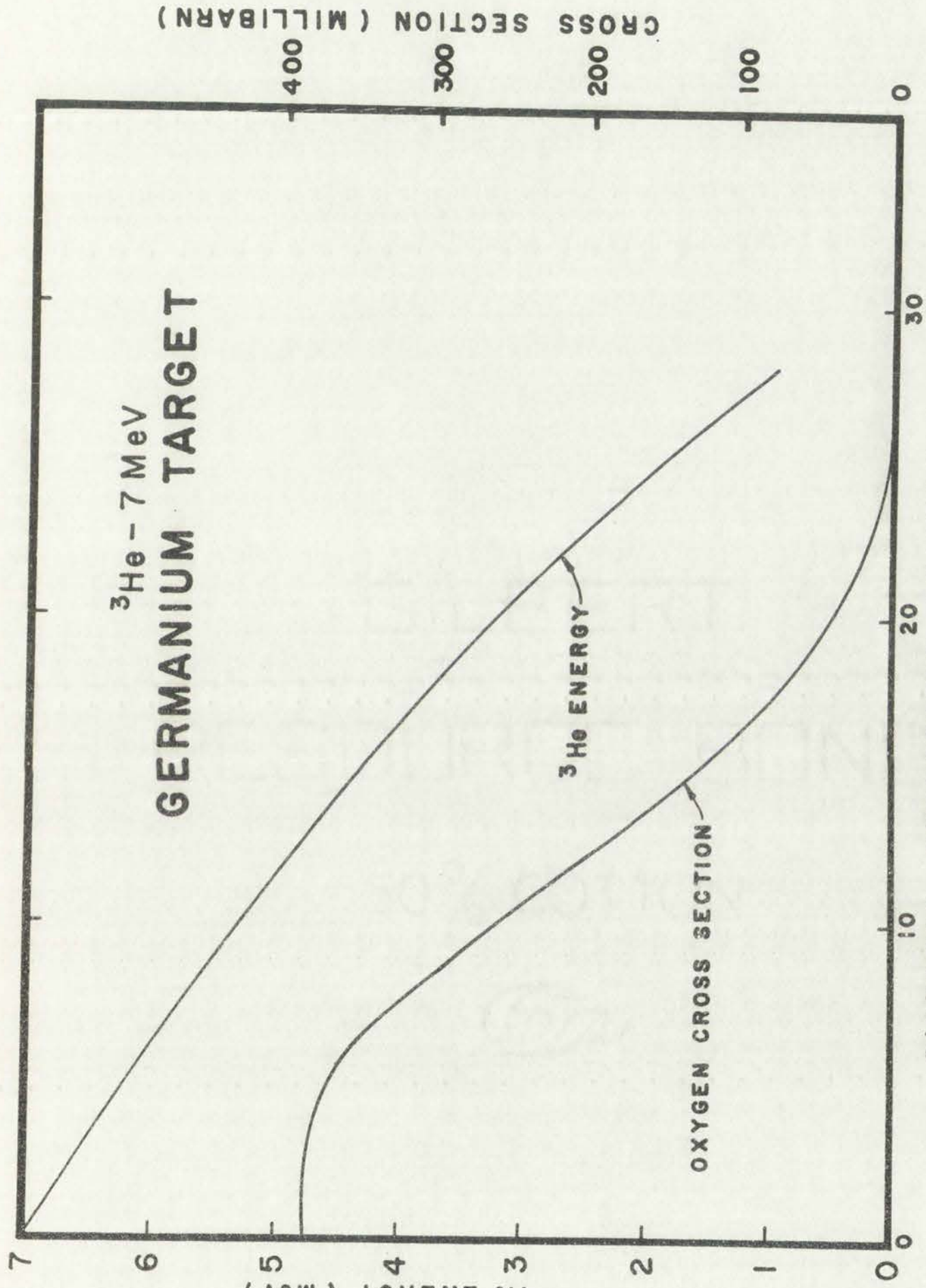

Fig. 2. ^{3}He energy and total oxygen activation cross section versus sample depth for 7-MeV ^{3}He particles incident randomly on germanium.

References 6 and 8 above show that the carbon and oxygen can be preferentially concentrated at grain boundaries or surface defects in the material. This can cause a large variation in results if the irradiated area or volume is small.

The existence of large gradients in the concentration of the impurity from the surface of the material or discontinuities from surface layers can cause extraneous results if these are not considered in the analysis of the data. If the sample oxidizes readily, as is the case for germanium, surface oxide layers may be present during the irradiation. For passive analyses, these can be removed by either chemical or mechanical means after the bombardment. However, it is difficult to remove precisely a given amount from the surface; and, if the range of the incident particle is small, as is the case for ^{3}He, the error introduced can be quite large. If the matrix is a single-crystal or polycrystalline material, channeling of the recoil impurity atoms from the surface layer into the matrix material may increase their range so that the heavy ions travel distances comparable with those traveled by the incident particle (Ref. 9). These displaced surface atoms will cause extraneously high results.

The techniques presented in this paper solve some of these problems. The samples were bombarded with ^{3}He particles, and the energy spectrum from the reaction protons was recorded after the protons had passed through an absorber to remove the backscattered ^{3}He ions. The range of the heavy recoil reaction products was immaterial. From the kinematics of the reaction, the cross sections of the reaction, and the absorber thickness, the proton spectrum and the sample depths that correspond to the proton energies can be calculated. Therefore, from the proton spectra, information about the distribution of the impurity atoms in the beam direction can be determined.

In reality, the activation curve or detector response is a function of the matrix material, the incident particle energy, the detector geometry, the impurity cross sections, and the distribution of the impurity on or in the matrix. In order to have the capability of calculating the detector response for various materials and distributions of the impurity atoms in these materials at various ^{3}He energies, the thin target excitation functions had to be determined. Knowing the thin target excitation functions, one can calculate the activation curves or detector response for any matrix for which the stopping-power data can be calculated and for any ^{3}He energies for which the excitation functions have been determined. Other methods of analyzing charged-particle activation data are the "equivalent thickness" method (Ref. 10) and the transform technique (Ref. 11). Neither of these techniques has the flexibility of the method presented in this paper. The "equivalent thickness" method is based on an established activation curve for a given reaction in a given material. The second method transforms a well-determined activation curve, using the different stopping powers, for use with different experimental cases.

The largest uncertainty in the method presented in this paper is the effect that energy straggling of the ^{3}He particles and of the protons in the sample and foil may have on the final resolution of the proton energy spectrum. This has been empirically resolved by defining a Gaussian resolution function whose width is a function of the proton energy of the reaction and the proton energy at the detector.

Qualitative information on the location of impurities in crystal matrices can be obtained if the sample is oriented so that the incident particles channel between the rows and planes of the structure (Ref. 12). Several such irradiations were performed on single-crystal germanium and

thoria samples. The parameters that affect channeling are too numerous to allow simple quantitative calculations. The sample temperature, irradiation damage history, number of defects, and sample alignment are a few of these parameters.

CHAPTER II

EXPERIMENTAL PROCEDURE

Introduction

The ^{3}He irradiations were performed on the Los Alamos vertical Van de Graaff accelerator with particle energies ranging from 2.6 to 9.0 MeV. Doubly ionized ^{3}He was accelerated exclusively to prevent possible contamination of the beam from $^{3}T^{+}$ and $^{3}(HD)^{+}$ which might be present in the source but could not be separated by the magnet since they have the same charge-to-mass ratio as singly ionized ^{3}He. The $^{3}He^{++}$ target currents were below 500 nA and were typically about 100 nA. These low target currents were due to the high beam collimation.

Anodized tantalum was used for the "thin" oxygen samples, and carbon evaporated on tantalum was used for the "thin" carbon samples. In addition to these, thick Ta_2O_5, carbon, and germanium samples were irradiated.

Pulse-height distributions of the prompt gamma rays and prompt protons from ^{3}He-induced nuclear reactions in these materials were recorded and analyzed. In addition, passive analyses of the delayed positron decay were made. Germanium samples were irradiated in channeling and non-channeling orientations to determine the effects of channeling in crystalline materials on activation-type analyses.

Sample Preparations

The "thin" oxygen and carbon samples used in these experiments were not self-supporting. Carbon was evaporated onto tantalum disks to form "thin" carbon samples (Ref. 13), and "thin" oxygen samples were formed by anodizing tantalum disks. The tantalum disks used were 0.86 mm thick

and about 5 cm diam. The high-Z and corresponding high-coulomb barrier of the tantalum prevented significant interactions of the ^{3}He ions with the tantalum nuclei. Therefore, the tantalum did not contribute greatly to the signals being measured, and these "thin" samples were similar to the actual surface layers that were to be investigated. The carbon, oxygen and other low-Z impurities present in the tantalum were of low enough concentration that they presented negligible interference. The most significant interference from the tantalum was in the prompt-gamma detector system. A gamma ray, apparently from excitation of a nuclear level in ^{181}Ta of approximately 136 keV, was present in the prompt-gamma spectra at the higher ^{3}He energies. The high count rate from this gamma degraded the resolution of the Ge(Li) detector system.

Carbon was evaporated in a vacuum directly onto one side of the tantalum. This gave a thin uniform carbon layer that was typically 15 μg-carbon/cm^2 thick. Oxygen targets were prepared by anodizing the tantalum in a very dilute H_2SO_4 solution (few drops of H_2SO_4 per 100 ml H_2O). The maximum current used in the anodization process was approximately 100 mA. The thicknesses of the anodic oxide films were varied by using various anodizing voltages. The thickest film corresponded to an anodizing voltage of 150 V and was measured to be 47.6 μg-oxygen/cm^2. The measurement of these surface layer thicknesses is described in Chapter III.[1] Prior to the deposition of the carbon and oxygen, the tantalum disks were etched in a solution of 25 parts 70% HNO_3, 55 parts 95% H_2SO_4, and 20 parts 48% HF for a few minutes to remove surface oxide layers and grease.

---

[1] The corresponding thicknesses that are consistent with the cross sections presented in Chapter IV are 18.8 and 33.6 μg/cm^2.

Special preparations were made on the germanium samples prior to their irradiation because the germanium surface readily oxidized upon exposure to air. The germanium samples were lapped with #600 grit silicon carbide paper and then etched in a solution of 3 parts HNO_3 and 1 part HF for about 30 sec. They were then placed directly into the target chamber and were allowed to dry in a vacuum of about 10^{-6} mm-Hg for 70 min to remove water from the sample surfaces before they were irradiated. Figure 3 shows the proton pulse-height distribution from an irradiated germanium crystal that had been exposed to the atmosphere for about four months after lapping and etching. The most significant peaks in this spectrum are from oxygen in the oxide surface layer on the sample. Figure 4 shows the corresponding spectrum from the irradiation of a germanium sample that had been lapped and etched just prior to the irradiation. The total current on the etched sample was four times that incident on the unetched sample. The pulse-height distribution in this case does not contain the peaks that are indicative of surface oxygen. The distribution in this latter case is indicative of a volumetric distribution of the oxygen. Both of these irradiations were in nonchanneling orientations. These data were taken before extensive cold trapping was done in the target area to prevent carbon deposition on the target by the beam during the irradiation. The carbon peaks present in both of these spectra were from carbon deposited on the target during the irradiation.

Experimental Area at the Van de Graaff

The beam tube and the experimental area used at the Van de Graaff are shown in Fig. 5. The ^3He beam was collimated by using the two slit assemblies shown in the picture. A close-up picture of a slit assembly and its associated viewing port is shown in Fig. 6. The slits were

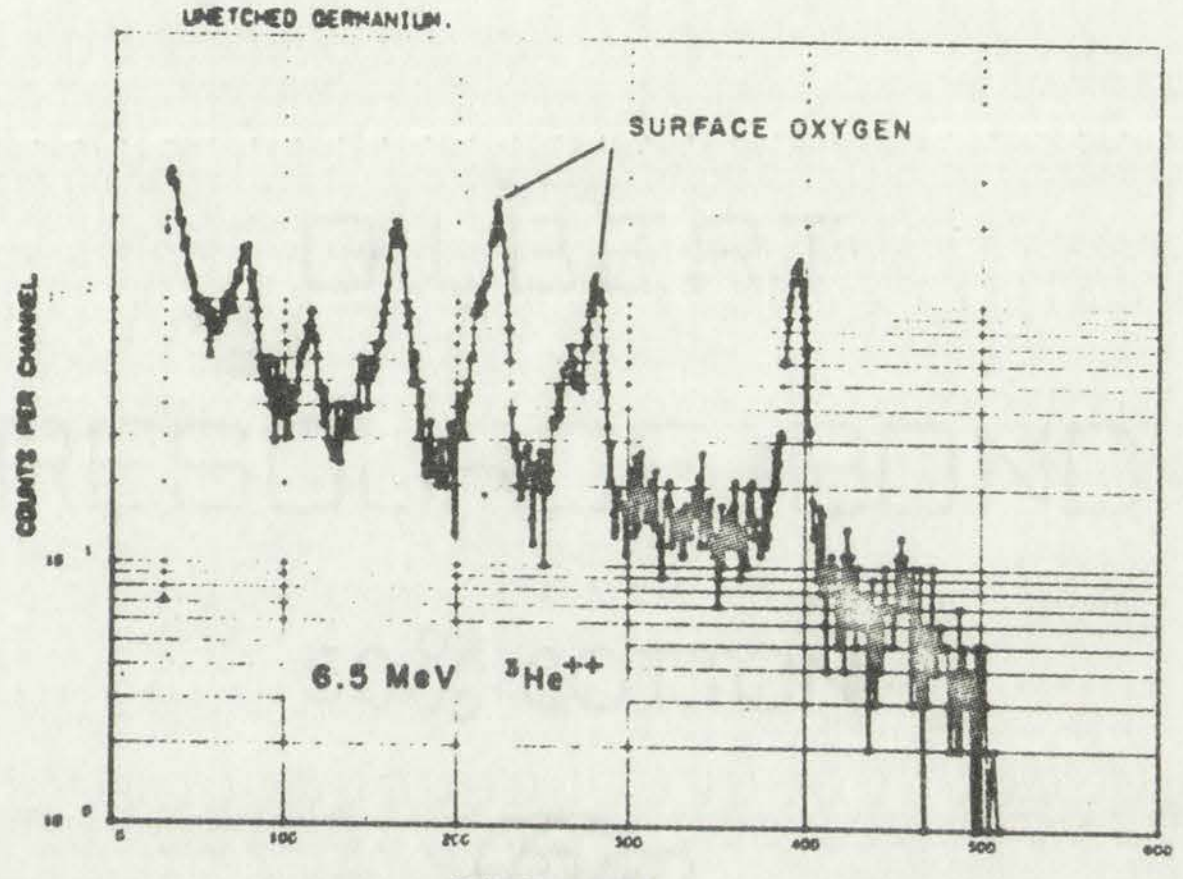

Fig. 3. Proton spectrum from the irradiation of a germanium crystal after its surface was allowed to oxidize in air.

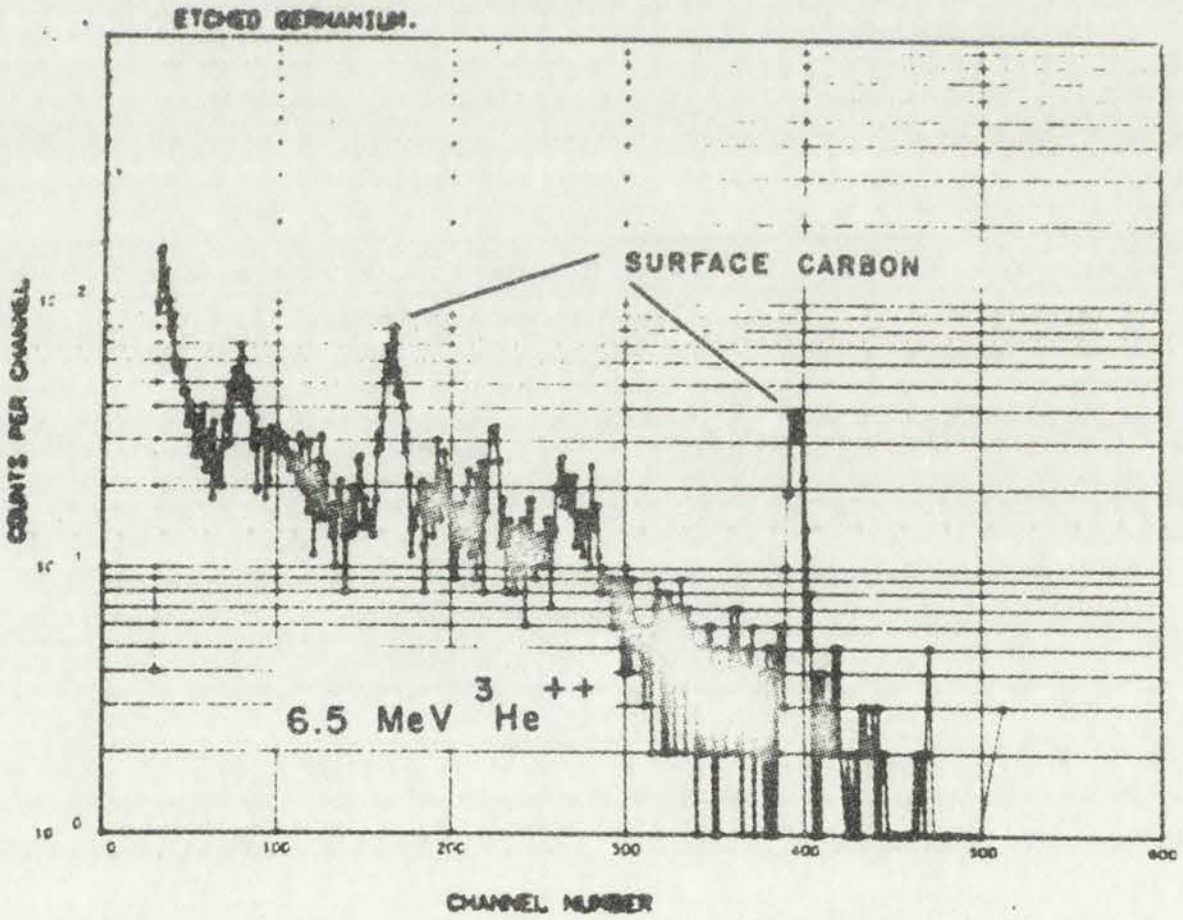

Fig. 4. Proton spectrum from the irradiation of a germanium crystal that was etched and then dried in a vacuum prior to the irradiation.

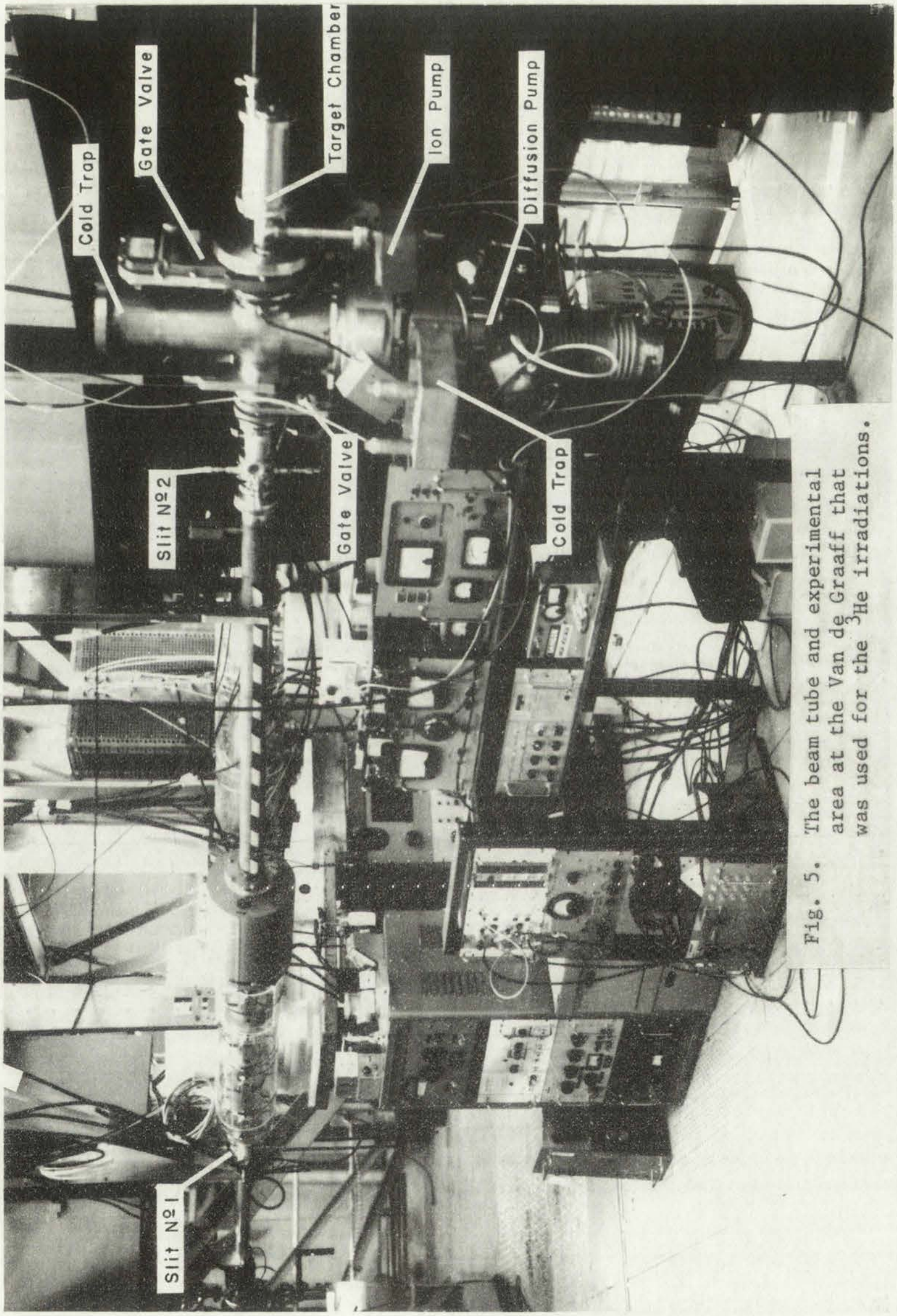

Fig. 5. The beam tube and experimental area at the Van de Graaff that was used for the ^{3}He irradiations.

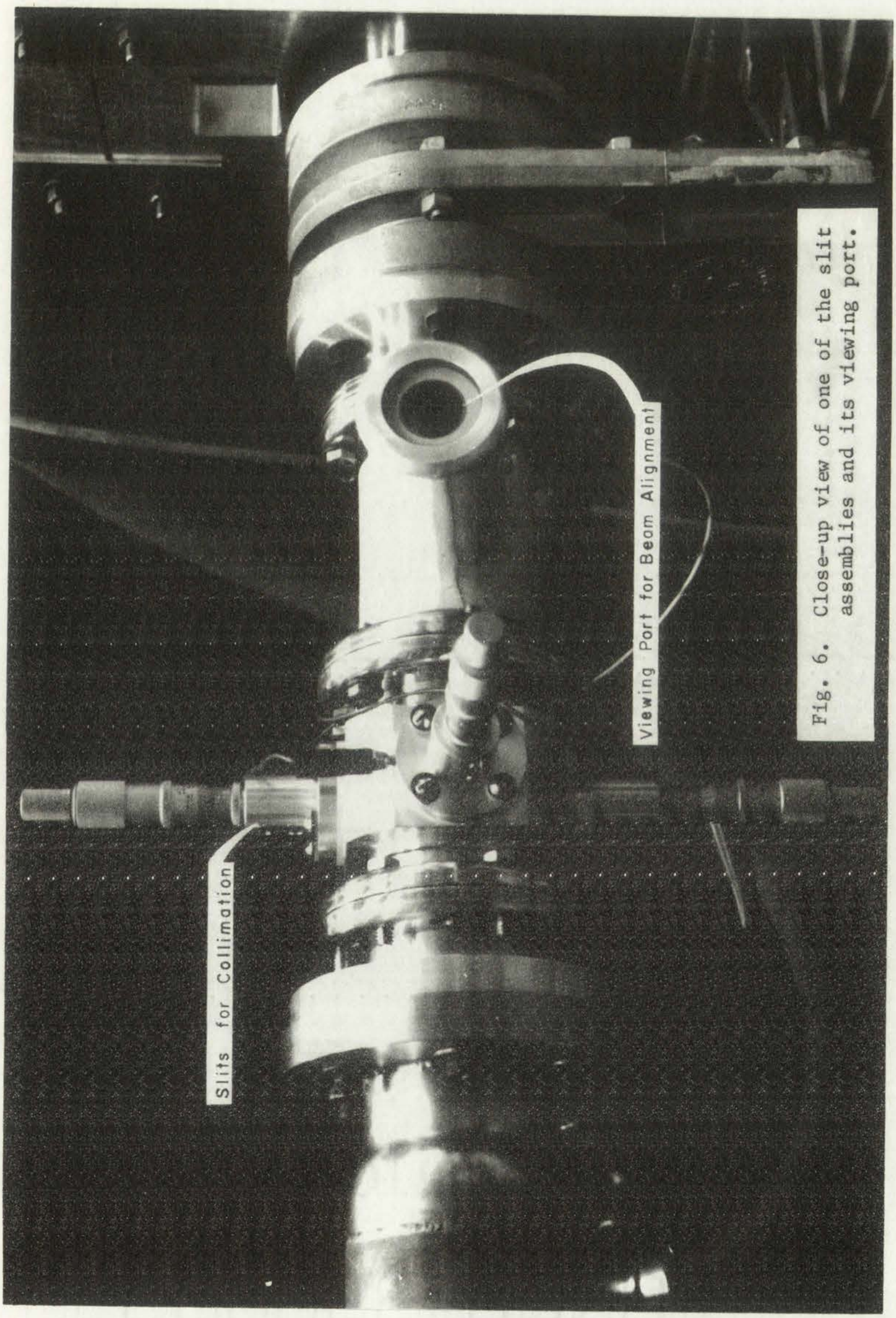

Fig. 6. Close-up view of one of the slit assemblies and its viewing port.

50% COTTON

3.34 m apart and had square apertures approximately 1.36 mm on a side. This corresponds to a beam divergence of about 4×10^{-4} rad. This high collimation, and the fact that no steering or focusing was used between the collimating slits, greatly limited the fraction of the beam striking the target. It was extremely difficult to steer the beam properly and to align the accelerator with this collimation. The viewing ports shown directly behind the collimating slits were used during the beam alignment. A quartz glass could be slid into the beam and the scintillations in the glass could then be used to indicate the beam profile after it had passed through the slit. The quartz glass was insulated from the beam tube so that the beam current through the slit could be measured directly and this signal could be used to maximize the current. The individual sides of the slits were insulated from the beam tube and each other so that the beam striking each of the four sides of the slit assembly could be measured. It was quite useful during the beam alignment to be able to determine where the beam was striking to obtain maximum current on the target.

Carbon buildup on the targets and slits was a problem during these experiments. To minimize this buildup on the targets, vacuum pumps and cold traps were placed near the target chambers. One pump was an oil diffusion vacuum pump with two liquid nitrogen cold traps. The top cold trap was specially designed so the ^{3}He beam passed through it. A second vacuum pump was placed directly on the standard target chamber. These special precautions did not completely eliminate the carbon buildup, but they did minimize it.

Two target chambers were used in these experiments. One chamber, referred to as the standard chamber, was used in determining the

excitation functions and for the calibration runs. The other chamber, with similar detector arrangements, contained a goniometer so that oriented irradiations could be made on germanium crystals. The outer wall of the standard chamber was 30 mil aluminum and designed so a Ge(Li) detector system could be placed near the target but outside the chamber so the prompt gamma-ray spectrum could be recorded during the irradiations. A collimated silicon surface barrier detector was located inside the chamber at 160° from the direction of the incident beam and was used to detect protons from ^{3}He-induced nuclear reactions. Thin aluminum foils (1 mil each) were placed between the target and detector so the backscattered ^{3}He particles and reaction alphas would not be detected. The resistivity of the detectors was about 25,000 Ω/cm and they were operated at 100 V. This gave a maximum full-energy detection range to about 11.0 MeV for protons. An electron suppressor operated at -300 V was placed in front of the target to repel the scattered electrons back to the target so that the full charge was collected.

The goniometer target chamber is shown in Fig. 7. This chamber was mounted directly behind the second gate valve shown in Fig. 3. Two silicon surface barrier detectors were mounted in front of the gate valve next to the cold trap. One detector was collimated and had aluminum foils between it and the target so that only the prompt protons were detected. The other detector was bare and was used to detect the backscattered ^{3}He particles during the alignment of the single crystals. The variations in the backscattered ^{3}He spectrum can be correlated with the various crystal planes and axes for the channeling experiments.

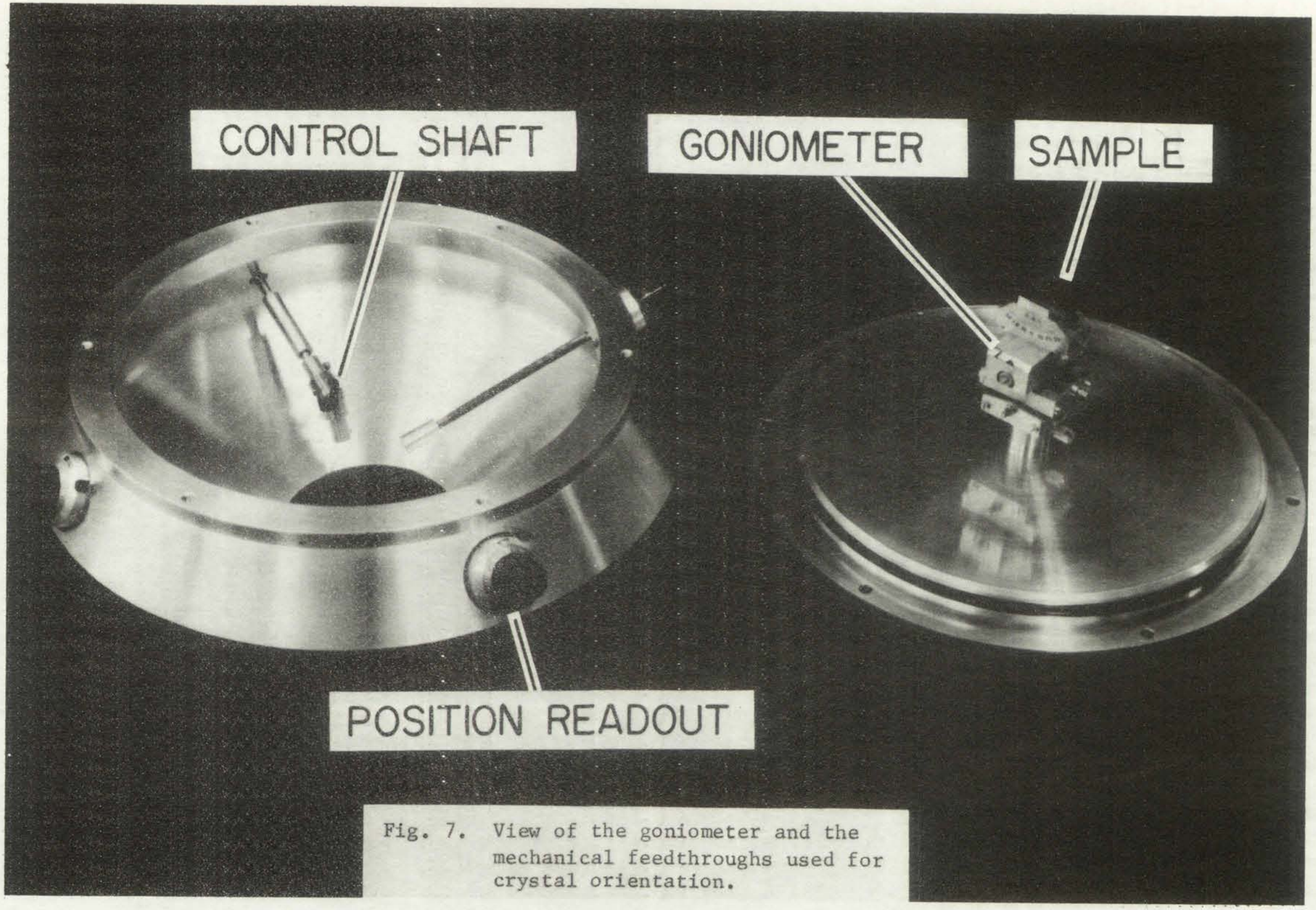

Fig. 7. View of the goniometer and the mechanical feedthroughs used for crystal orientation.

Schematic drawings of the standard target chamber and of the electronic systems are shown in Figs. 8 and 9. Standard low-noise preamplifiers and linear amplifiers were used. Signals from these were digitized using a 2048-channel ADC for the prompt gamma-ray signal and a 512-channel ADC for proton and charged-particle detector systems. The ADC's were connected to the on-line computer system at the accelerator (Refs. 14 and 15). Data from the irradiations were recorded on a high-speed printer, a magnetic tape and plotted directly. In addition to the spectral data, the length of the irradiation, time of day, total current and dead time were recorded for each spectrum. The magnetic tape output was processed using the central computer facilities at the Los Alamos Scientific Laboratory.

Alignment of Germanium Crystals

Channeling irradiations were performed on single-crystal germanium samples. The samples were roughly aligned with their $\langle 111 \rangle$ axis parallel to the beam when they were mounted on the goniometer in the target chamber. The goniometer was adjusted to orient the crystal in the various channeling directions. The goniometer adjustments would allow translation of the crystal in two directions, perpendicular to the beam and perpendicular to each other, and rotation of the sample about these axes. The translation was limited to 1 cm. One rotation was limited to 30° and the other was limited to 25°.

A bare silicon surface barrier detector was used to detect the backscattered ^{3}He pulse-height distribution that was used for sample alignment. Figure 10 shows the pulse-height distribution from the backscattered ^{3}He during a nonchanneling irradiation. Figure 11 shows the corresponding pulse-height distribution that was obtained when the sample

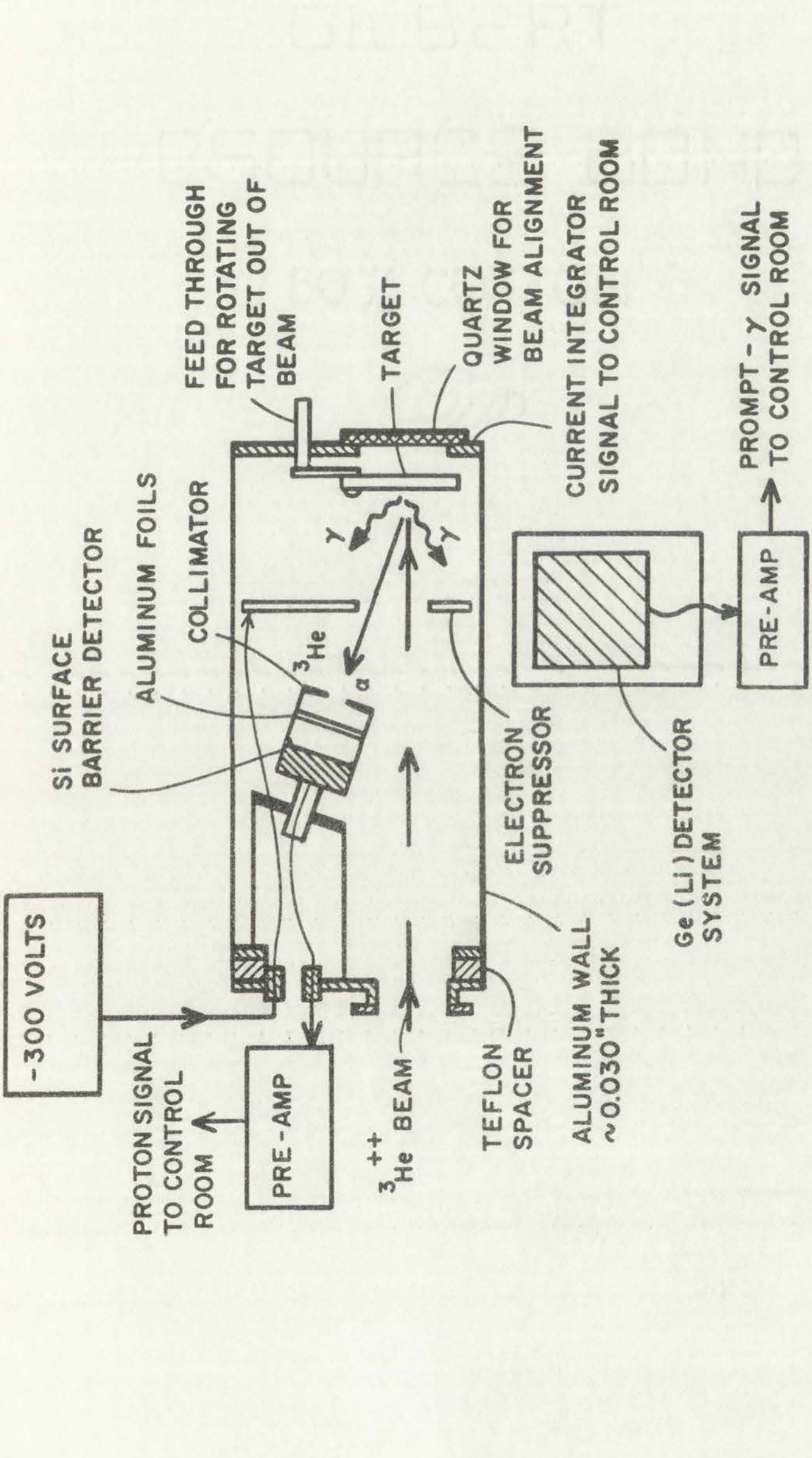

Fig. 8. Schematic drawing of the standard target chamber.

SCHEMATIC
OF
ACCELERATOR ELECTRONICS

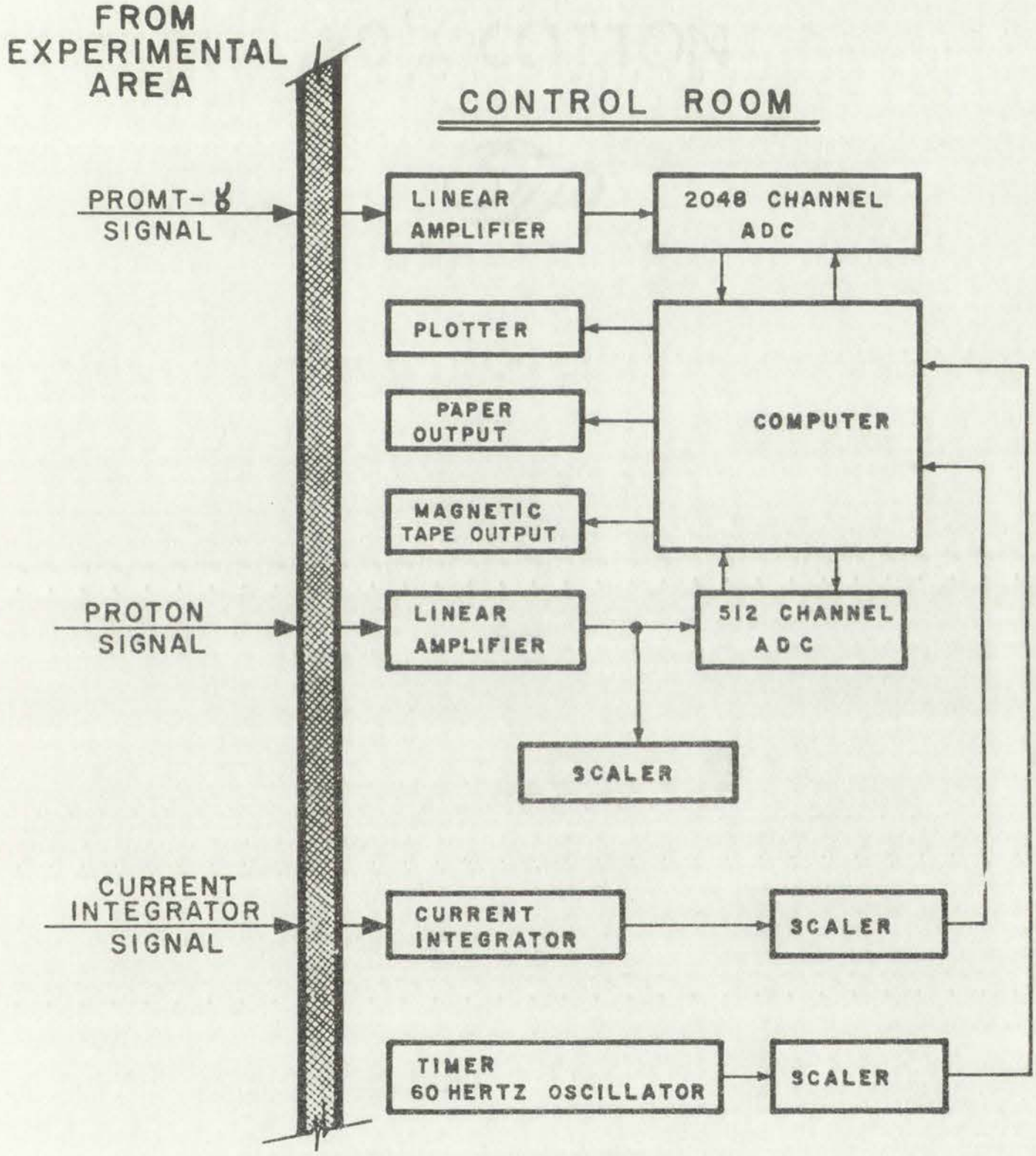

Fig. 9. Schematic drawing showing the wiring and electronic equipment used in the Van de Graaff control room.

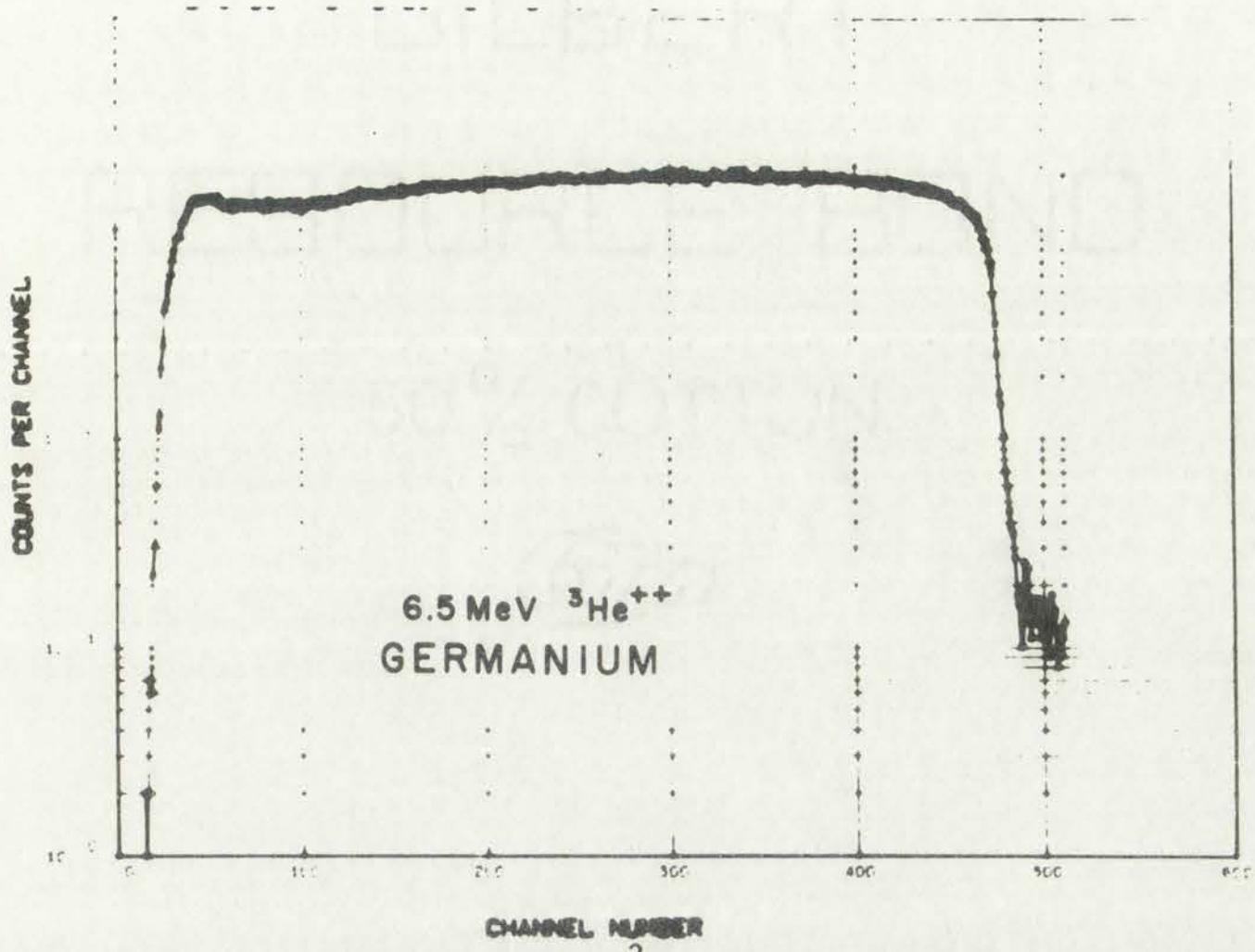

Fig. 10. Plot of the backscattered ^{3}He pulse-height distribution from the irradiation of a germanium crystal in a nonchanneling orientation.

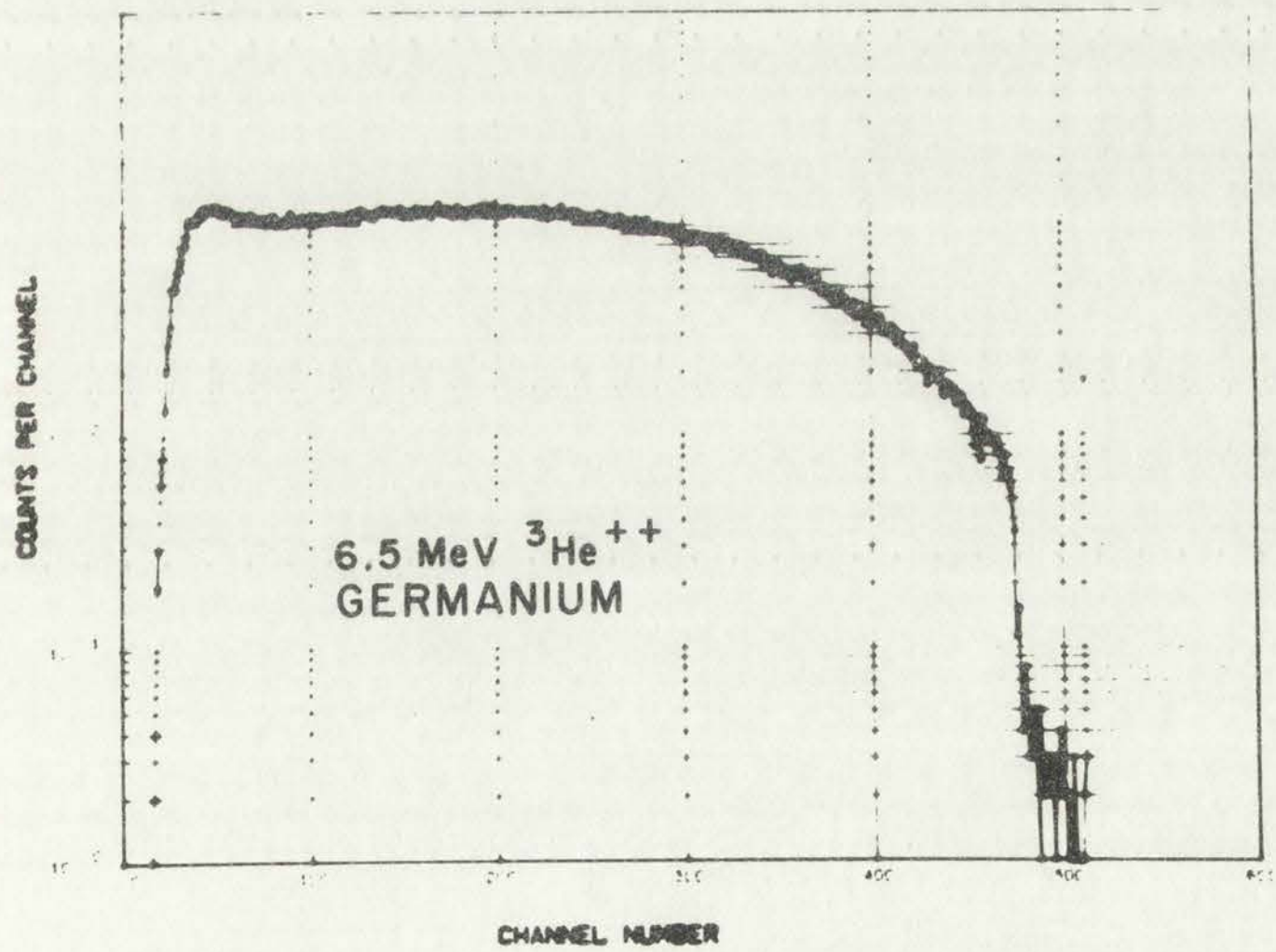

Fig. 11. Plot of the backscattered ^{3}He pulse-height distribution from the irradiation of a germanium crystal in a channeling orientation.

was oriented in the ⟨111⟩ direction. The channeling spectrum has fewer counts than the nonchanneling spectrum. This deviation is particularly evident at the high-energy end of the spectrum which corresponds to backscatters from near the surface. The effect of multiple hard scatters, as the ^{3}He particles penetrate deeper into the crystal, decreases the effect of channeling on the low-energy portion of the spectrum.

The alignment procedure for the channeling irradiations consisted of using a single-channel analyzer and scaler to record the count rate in the high-energy portion of the ^{3}He backscatter spectrum at various goniometer settings. The single-channel analyzer was set so that only pulses with amplitudes corresponding to energies from about 1 MeV below to slightly above the maximum backscatter energy produced an output pulse to the scaler. A set of data that was obtained during the alignment of a sample for a channeling irradiation along the ⟨111⟩ axis is shown in Fig. 12. The backscatter dips are shown for each of the {110}-type planes. One limitation of the goniometer used in these experiments was the lack of ability to rotate the samples about the incident ^{3}He beam. Therefore, it was impossible to rotate the sample about an axis parallel with the channeling plane and minimize the angular half width of the backscatter dips. The differences in the widths of the backscatter dips shown in Fig. 12 are due to the differences in the angles of the planes relative to the two axes about which the goniometer was rotated to cross the plane.

Experimental ^{4}He channeling data from Ref. 16 were extrapolated to compare with the above data. It was assumed that the channeling characteristics of ^{3}He ions are similar to those for ^{4}He and that the width

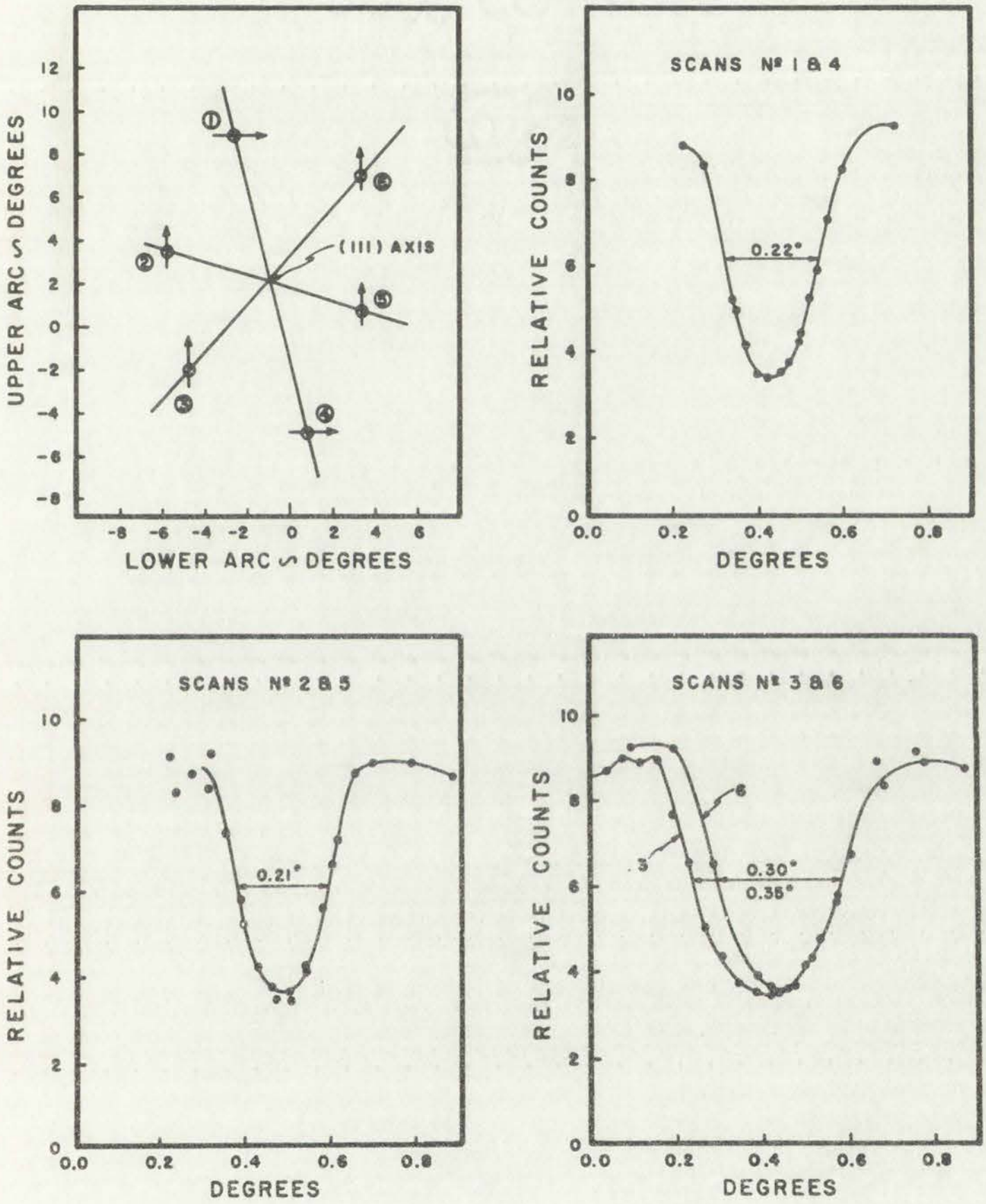

Fig. 12. Data obtained during the alignment of a germanium crystal.

of the channeling dips can be given by

$$FWHD = K/\sqrt{E}$$

where K is a constant and E is the ion energy. Extrapolation gives a value of 0.24° for the corresponding width of the backscatter dip for the {110} planes in germanium. This compares quite well with the data shown in Fig. 12.

A backscatter dip as the goniometer was rotated across the ⟨111⟩ axis of a germanium sample is shown in Fig. 13. The nonsymmetric nature of the dip is due to the location of the {110}-type planes relative to the axis about which the goniometer is being rotated. Just to the left of the dip there is an orientation which shows an increase in the number of backscatters over that for a nonchanneling orientation.

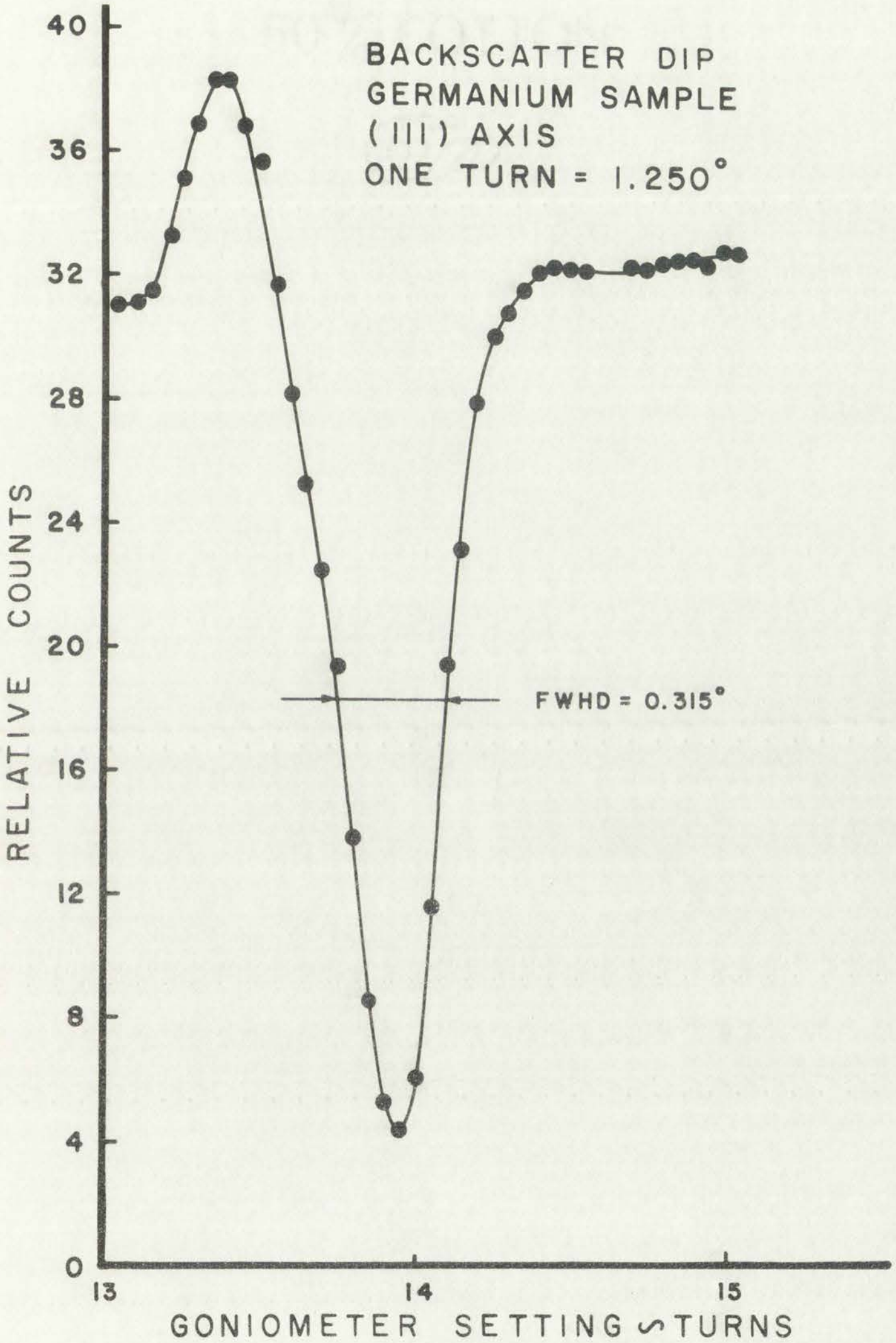

Fig. 13. Plot of the count rate from the high-energy backscattered ^{3}He as the goniometer was rotated across the $\langle 111 \rangle$ axis of a germanium crystal.

CHAPTER III

CALIBRATION USING PASSIVE ANALYSES

Introduction

Thin carbon and oxygen targets were irradiated with 8.6 MeV ^{3}He ions in the standard target chamber. The proton spectra were recorded during the irradiations. After the irradiations, the samples were counted in a 4π NaI detector system and their decay histories were recorded. The main activation products were ^{11}C from the $^{12}C(^{3}He,\alpha)^{11}C$ reaction and ^{18}F from the $^{16}O(^{3}He,p)^{18}F$ reaction. Half-life data and Q values for these and a few other reactions of interest are given in Table 1.

TABLE 1

NUCLEAR REACTIONS, THEIR HALF-LIVES AND Q VALUES

Reaction	Half-Life*	Q Values (MeV)**
$^{12}C(^{3}He,d)^{13}N$	10.1 min	-3.5498
$^{12}C(^{3}He,\alpha)^{11}C$	20.4 min	+1.8582
$^{12}C(^{3}He,p)^{14}N$	stable	+4.7786
$^{16}O(^{3}He,p)^{18}F$	110. min	+2.0334
$^{16}O(^{3}He,\alpha)^{15}O$	124. sec	+4.9101

*Ref. 2

**Ref. 17

Cross sections published by Markowitz and Mahony (Ref. 2) and Cochran and Knight (Ref. 18) were used to calculate the carbon and oxygen thicknesses and to calibrate the proton detector system. For these passive analyses, the fluctuations in the beam current during the irradiations

were large enough to influence the results. Therefore, the currents on the targets were recorded at 10-sec intervals during the irradiations so that corrections could be made for these fluctuations. The on-line computer system at the accelerator was used for this recording.

The carbon sample was irradiated for approximately 24 min at an average beam current of 83 nA. The oxygen sample was irradiated for approximately 28 min at an average current of 143 nA.

Data Acquisition

After the irradiation, each sample was counted in a 4π detector system and its spectral history was recorded. The detector system is shown in Fig. 14. It consisted of two optically isolated 13.5-in.-diam by 6-in.-thick NaI(Tl) cylinders with a 2½-in.-diam hole between them for sample insertion. The NaI(Tl) was shielded with 6 in. of low-background TADANAC lead. The coincident and the single spectra were simultaneously recorded using a 4096-channel analyzer. The spectra were recorded at 100-sec intervals on a magnetic tape. These data were later used with computer codes that analyzed the spectra and unfolded the complex decay curves.

A schematic diagram of the electronics is shown in Fig. 15. The pulses from each half of the detector were fed into a mixer and summed. In addition, the output from a 60-Hz pulser was routed into the mixer so that the dead time of the system could be calculated. The mixer summed the simultaneous input pulses. This summed pulse was routed to the input to the ADC of the pulse-height analyzer and was digitized to a maximum of 2048 channels. Each half of the detector was checked for coincident output pulses. If a coincidence occurred, a pulse was sent from the coincidence unit to the address register of the analyzer, causing

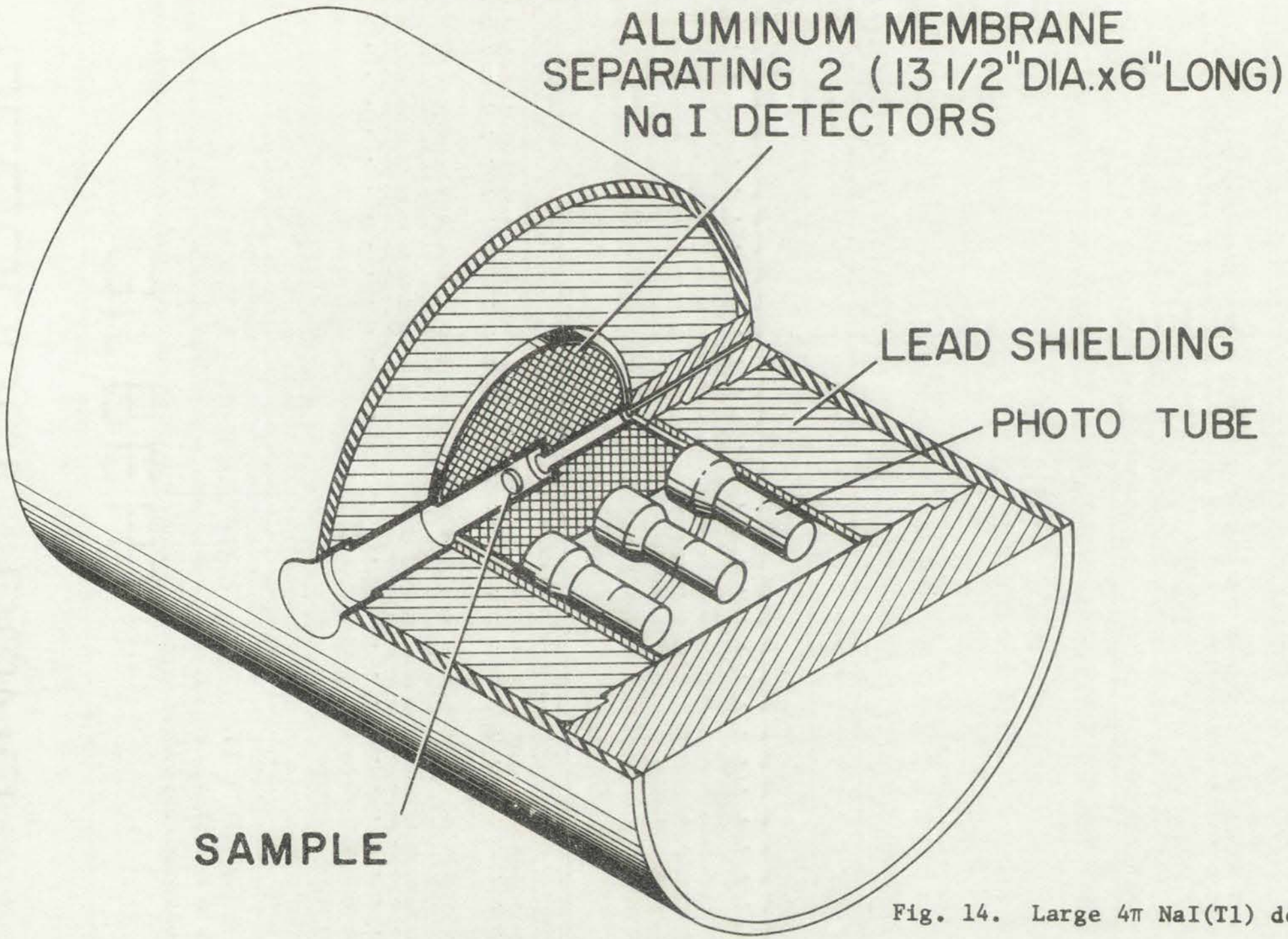

Fig. 14. Large 4π NaI(Tl) detector system.

SCHEMATIC
DATA SYSTEM FOR 4Π COUNTING

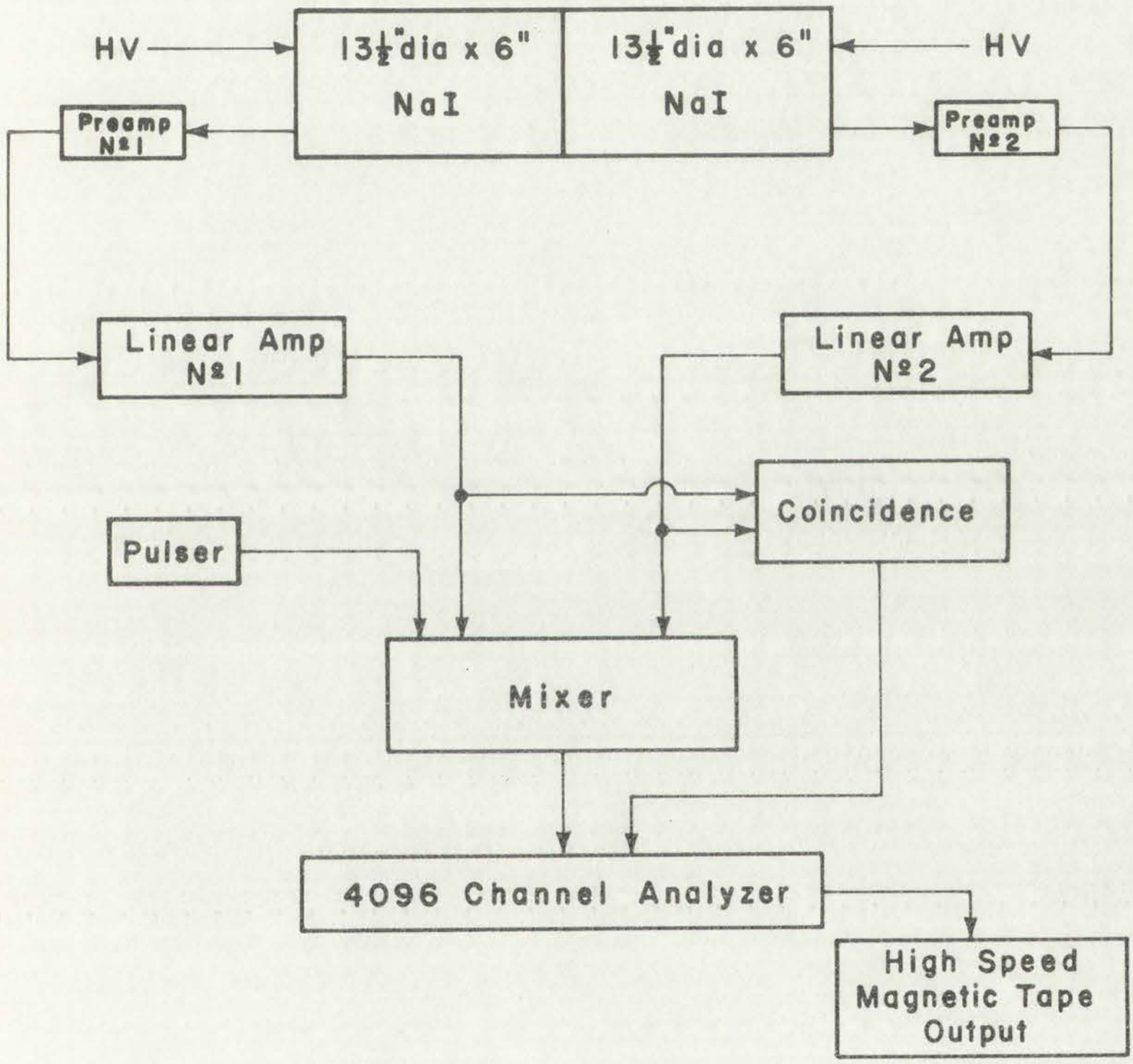

Fig. 15. Schematic diagram of the electronics used with the 4π detector system.

the digitized data to be stored in the upper 2048 channels. Otherwise, the pulse was stored in the lower 2048 channels.

Data were accumulated for intervals of 100 sec (clock time), and then the spectral data were recorded on a magnetic tape. The 4096 20-bit data words were recorded on the tape, the analyzer cleared, and accumulation of the next set of spectral data started in 2.14 sec.

A 60-Hz pulser was used to determine the live time during the count intervals. The output of the pulser was adjusted so that the pulser peak occurred near the upper end of the lower 2048 channels. This type of live-time determination was satisfactory at the count rates encountered (less than 1.5×10^4 counts/sec). At count rates higher than this, random coincidences between the pulser and the detectors would remove counts from the pulser peak. This would give a smaller live time than was actually present. At higher count rates, where the dead time becomes significant, the statistical variation of the number of counts in the pulser peak becomes significant. At these higher count rates, a higher frequency pulser would have been used to obtain the necessary accuracy.

A background spectrum from a 1000-sec count is shown in Fig. 16. The background count rate was higher than usual at the time these experiments were conducted due to the presence of a highly radioactive reactor fuel element in a nearby gamma-ray scanning cave. The singles background rate, integrated over the energy region indicated in the left-hand spectrum of Fig. 16, was 366 counts/sec. The corresponding coincident background count rate was 25.9 counts/sec.

Figure 17 shows the pulse-height distribution obtained from the carbon sample approximately 15 min after the irradiation stopped. The pulser peak and important gamma-ray peaks are labeled. The small broad

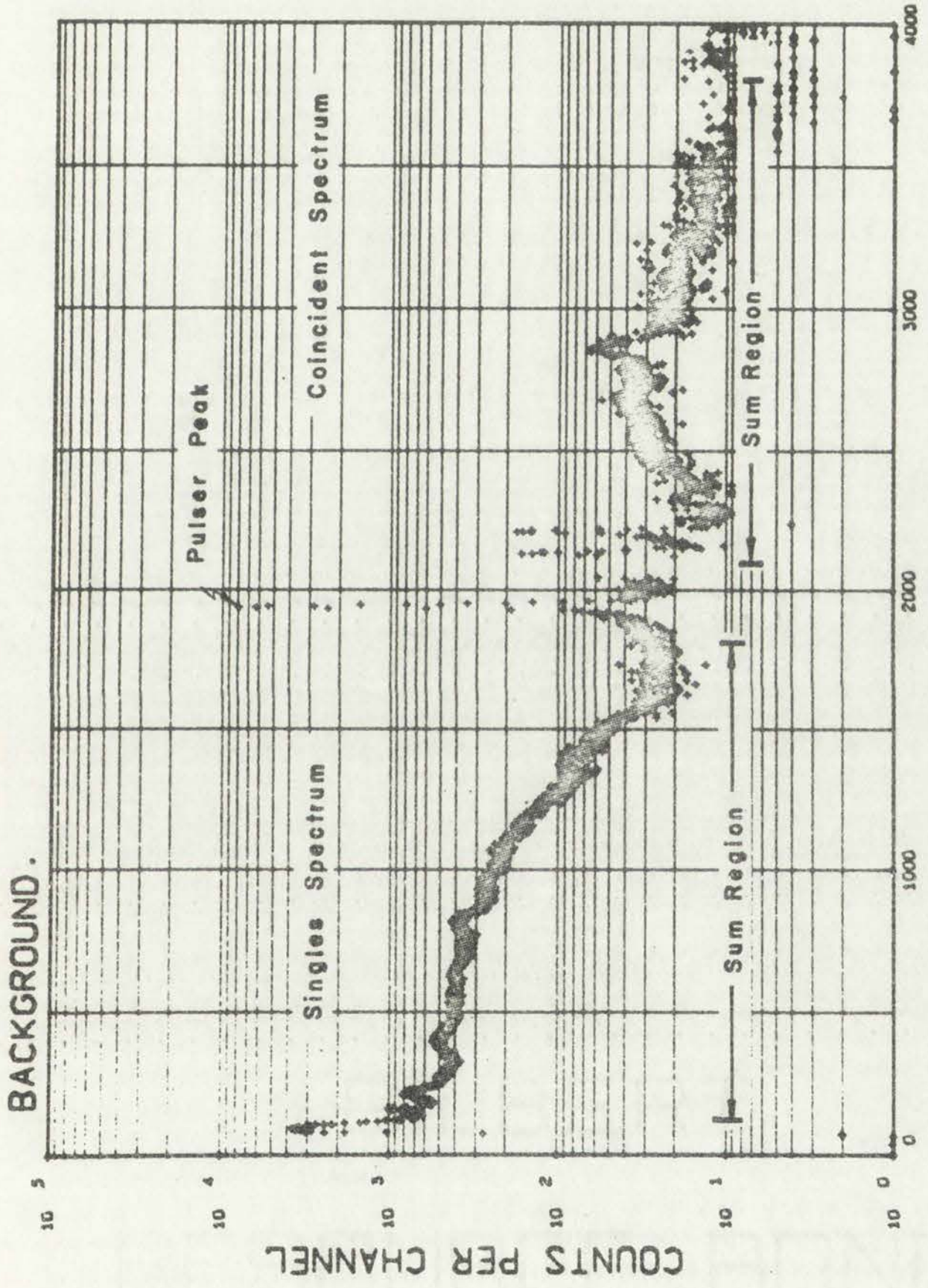

Fig. 16. Background from the 4π detector system.

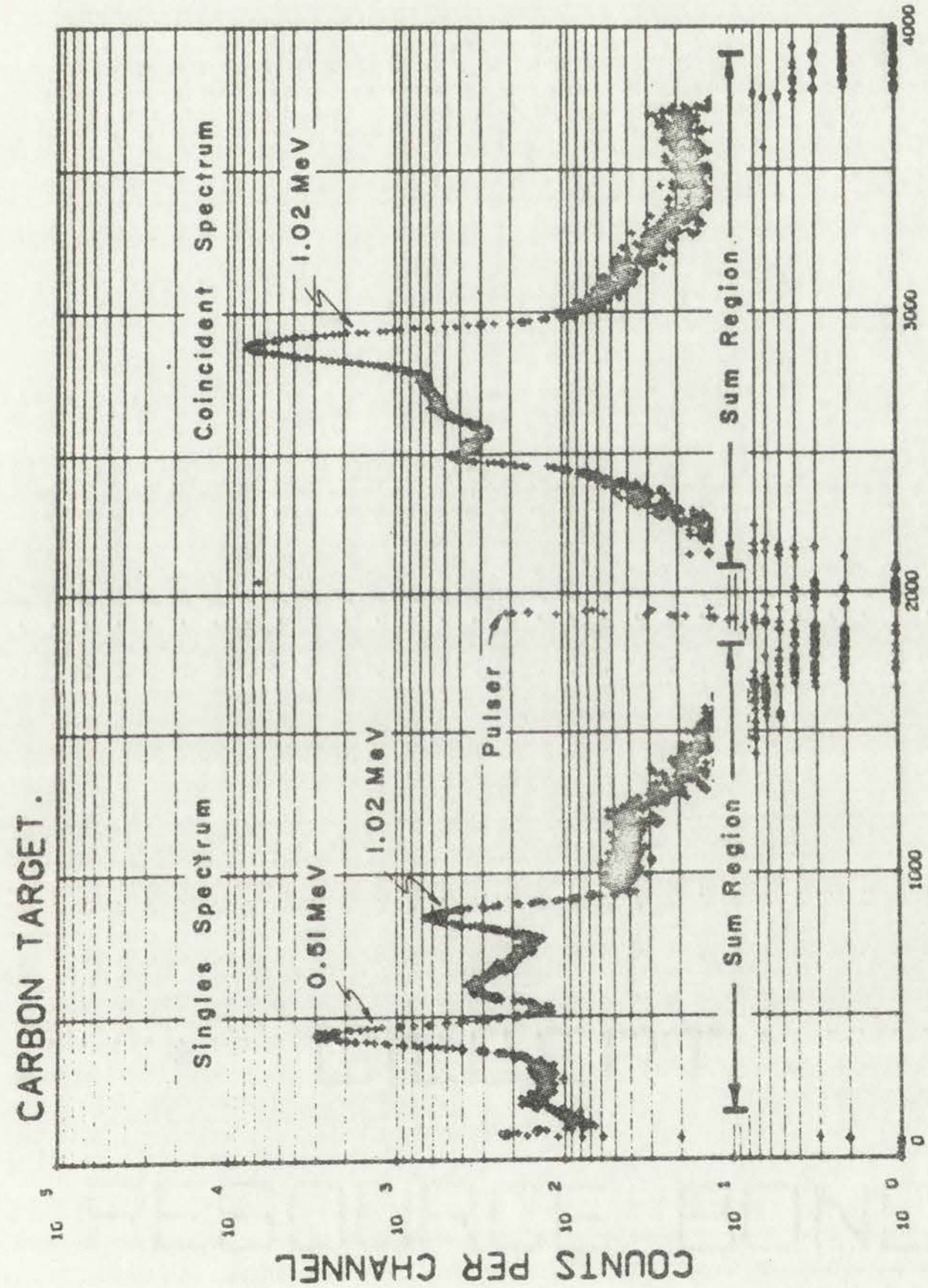

Fig. 17. Spectrum from ^{3}He irradiated carbon sample placed in the 4π detector system.

peak between the 0.51 MeV peak and the 1.02 MeV peak in the singles spectrum is from 3-quanta annihilation where one of the quanta escaped detection (e.g., Ref. 19). In fine-grained MgO power, the probability for 3-quanta annihilation can be as large as 20 to 25% (Ref. 20).

The carbon decay curve was constructed from 85 sets of spectral data. The singles spectra were integrated from 145 keV to 1230 keV. The coincident spectra were integrated from 115 keV to 1240 keV. The sum of these two numbers was then used to construct the decay curve because the total efficiency of the detector system was better known than the coincident efficiency.

The decay curve from the oxygen sample was constructed from 143 sets of spectral data. Because both ^{11}C and ^{18}F do not have a coincident gamma ray associated with their decay, the shape of the oxygen spectra was quite similar to that of the carbon data shown in Fig. 17.

Decay Curve Analysis

Since the activation products from ^{3}He irradiations are usually neutron deficient, they normally decay by positron emission. Many of the activation products are pure positron emitters as in the case of ^{18}F and ^{11}C. One way to determine the amounts of these isotopes present in a sample is by counting the 0.51 MeV annihilation radiation for various time intervals and unfolding the complex decay curve into its components. The DEcay CURve Analysis code, DECURA, was written to analyze complex decay curves obtained during ^{3}He activation analysis studies. The function

$$Y(J) = P(1)*\sum_{I=1}^{NOI} P(I*2)*EXP(P(I*2+1)*X(J))$$

is fitted to the decay curve data using least-squares techniques. The J subscript refers to the Jth data point, and the I subscript refers to the Ith exponential or component. The best least-squares value can be obtained for each of the P(I) variables in the equation. Y(J) is the decay rate in counts/sec that is obtained by integrating the pulse-height spectra. X(J) is the elapsed time since the irradiation stopped. No provision is made for correcting for decay during the counting interval.

The code uses pulser data to determine the live time during the counting interval.

The output that is used from this code is the counts/sec for each isotope extrapolated to the time the irradiation stopped. Figure 18 shows the analysis of the complex decay curve from the carbon data. The experimental data are analytically represented by four exponentials. These four exponentials, their sum, and the experimental data points are shown on the plot. The main component, with a 20.3-min calculated half-life, is from ^{11}C, the reaction product from the $^{12}C(^{3}He,\alpha)^{11}C$ reaction. The analysis indicates the presence of a component with a 7.7-min half-life. This is probably mostly due to the presence of ^{13}N from the $^{12}C(^{3}He,d)^{13}N$ reaction, but the calculated number could also be influenced by the presence of ^{15}O from the $^{16}O(^{3}He,\alpha)^{15}O$ reaction at the very early times. The presence of a small amount of ^{18}F from the $^{16}O(^{3}He,p)^{18}F$ reaction from body and surface oxygen associated with the tantalum is also indicated. The half-life of this component was fixed during the calculation at 110 min. The presence of a small amount of long half-lived products is indicated from the fit. The uncertainty associated with the results of this fit are probably an upper limit as calculated in the least-squares code. This is from the rather large variance due to statistical

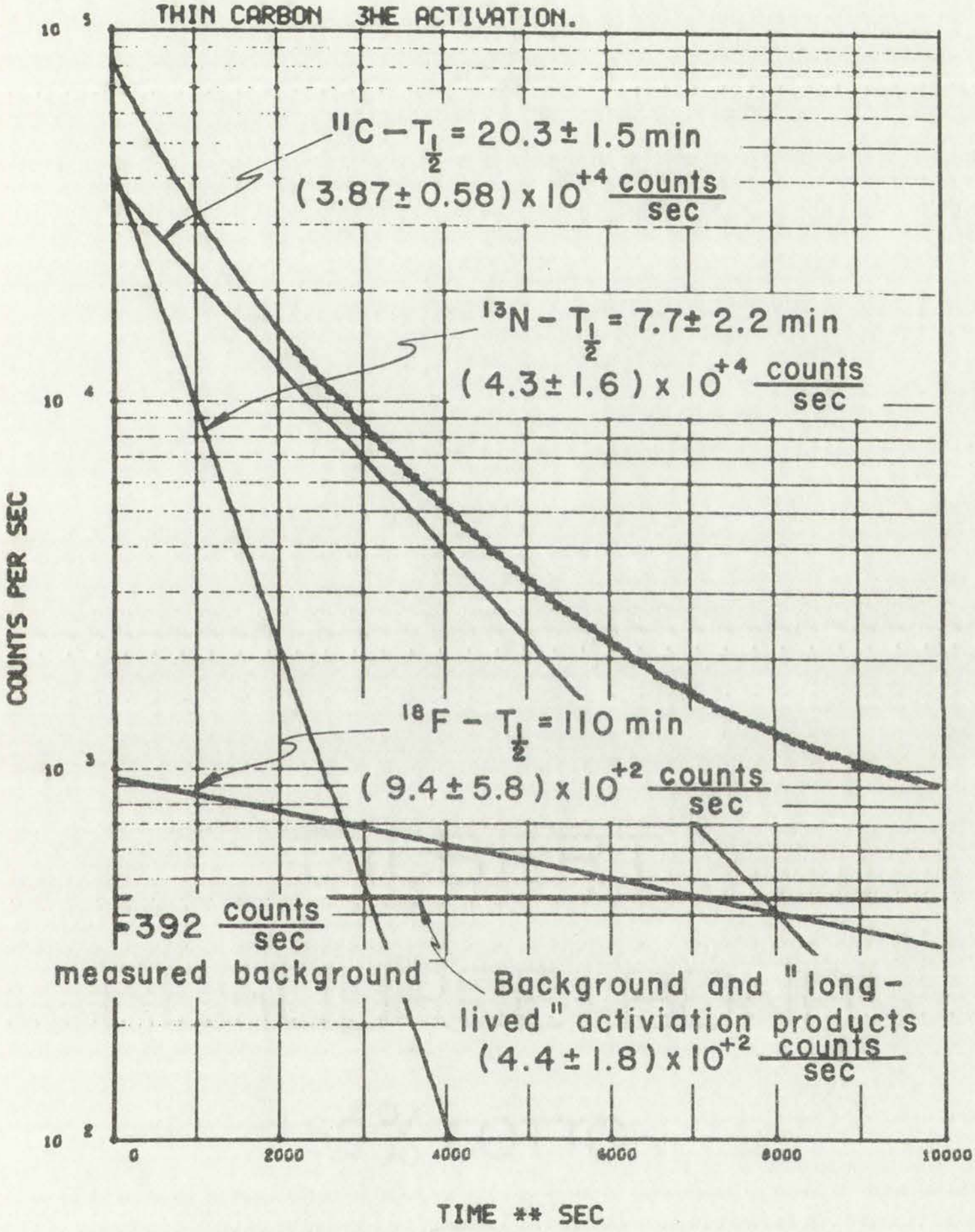

Fig. 18. Unfolded complex decay curve from activated carbon sample.

fluctuation in the live-time determination. The results of this analysis are given in Table 2.

Code DECURA is discussed in Appendix A.

TABLE 2

RESULTS FROM ANALYSIS OF CARBON ACTIVATION SAMPLE

Isotope Assigned	Half-Life Calculated (min)	Relative Decay Rate at Time Zero (counts/sec)
^{11}C	20.3 ± 1.5	$3.8 \pm 0.6 \times 10^4$
^{13}N	7.7 ± 2.2	$4.3 \pm 1.6 \times 10^4$
^{18}F	110. (fixed see above)	$9.4 \pm 5.8 \times 10^2$
---	long-lived	$0.5 \pm 0.2 \times 10^2$

Calculation of the Target Thicknesses

A computer code, SVCCPA (Surface and Volumetric Concentrations from Charged Particle Activations), was written to determine the volumetric and corresponding surface concentration of the activation product from the unfolded decay curve data. This code is discussed in Appendix B.

The beam current history tape generated during the irradiation is used to correct for fluctuations in the beam current during the irradiation. Analytical representation of the ^3He cross-section data of Markowitz and Mahony (Ref. 2) and Cochran and Knight (Ref. 18) are used in the code. The cross section as a function of ^3He energy is fitted with a combination of Gaussians and exponentials. This code, GHLET (Gaussian with High and Low Energy Tails), is discussed in Appendix C. It has been quite useful in the analysis of cross-section data and other experimental data where the distributions are basically of a Gaussian or Lorentzian shape. The analytical representation of the $^{12}C(^3He,\alpha)^{11}C$ cross section is shown in Fig. 19.

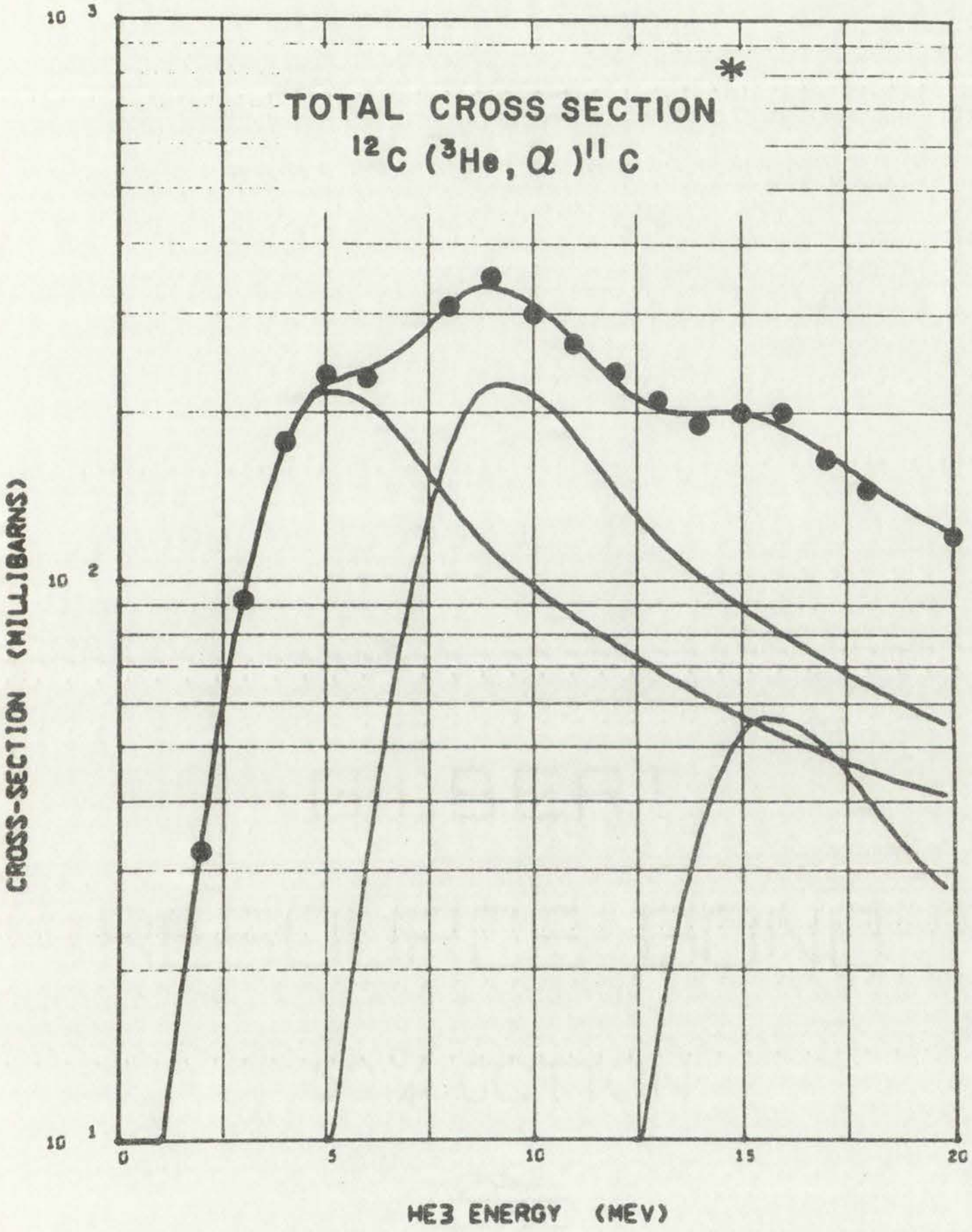

Fig. 19. Analytical representation of the $^{12}C(^{3}He,\alpha)^{11}C$ cross section.

* Data from Refs. 2 & 18.

Corrections are made in SVCCPA for detector efficiency and branching ratios. In this experiment, the detector efficiency was approximately 100% due to the size of the detector system and the fact that there are two photons per positron decay. The branching ratio used for ^{18}F was 97% (Ref. 21) and for ^{11}C was 100% positron decay.

Concentrations of the impurity atoms are calculated assuming that they are all on the surface and also assuming a homogeneous volumetric concentration. Of interest in this calibration data was the surface concentration since both samples had thin layers deposited on their front surfaces. In the volumetric calculation, the position of the ^{3}He particle is determined as it penetrates the sample from the dE/dx data for each 0.01 MeV energy increment.

$$\frac{dE}{dx} = s(E)$$

$$\Delta x = x_2 - x_1 = \int_{E_1}^{E_2} \frac{1}{s(E)}\, dE$$

The integral $\int_{E_1}^{E_2} \frac{1}{s(E)}\, dE$ is determined numerically from the integration of the cubic spline interpolation function of $\frac{1}{s(E)}$. The use of the interpolatory cubic spline functions and the stopping power data used in this experiment are discussed further in Chapter IV.

The average cross section between E_1 and E_2 for each energy step is given by

$$\bar{\sigma} = \frac{\int_{E_1}^{E_2} \sigma(E)\, dE}{E_2 - E_1} \quad .$$

The integral, $\int_{E_1}^{E_2} \sigma(E)\, dE$, is evaluated by numerical methods. The cross section as a function of energy,

$$\sigma(E) = g(E) \quad ,$$

is the analytical representation of the experimental cross section obtained from GHLET.

In these calculations, it is assumed that the number of particles in the beam remains constant as it penetrates the sample. This is to say that energy losses are due primarily to ionization and that reaction and other hard cross sections are small. In the above calculations, the cross sections become small enough at low energies that the calculation can be terminated once the ^{3}He energy reaches 1 MeV.

Prompt Proton Data

The prompt proton data from these samples were recorded during the irradiations using a silicon surface barrier detector, a 512-channel analyzer, and ancillary electronics. Reaction alphas and backscattered ^{3}He particles were absorbed in three 25 μ aluminum foils between the detector and target to prevent their energy deposition in the detector. The detector was located at 160° from the incident beam direction. The proton spectrum from the carbon irradiation are shown in Fig. 20, and the corresponding data from the oxygen irradiation is shown in Fig. 21. Detailed analyses of these data and the techniques used to analyze the proton spectra are presented in Chapter IV. The total $^{3}He^{++}$ charge collected during the carbon irradiation was 1.2×10^{-4} C and during the oxygen irradiation was 2.4×10^{-4} C.

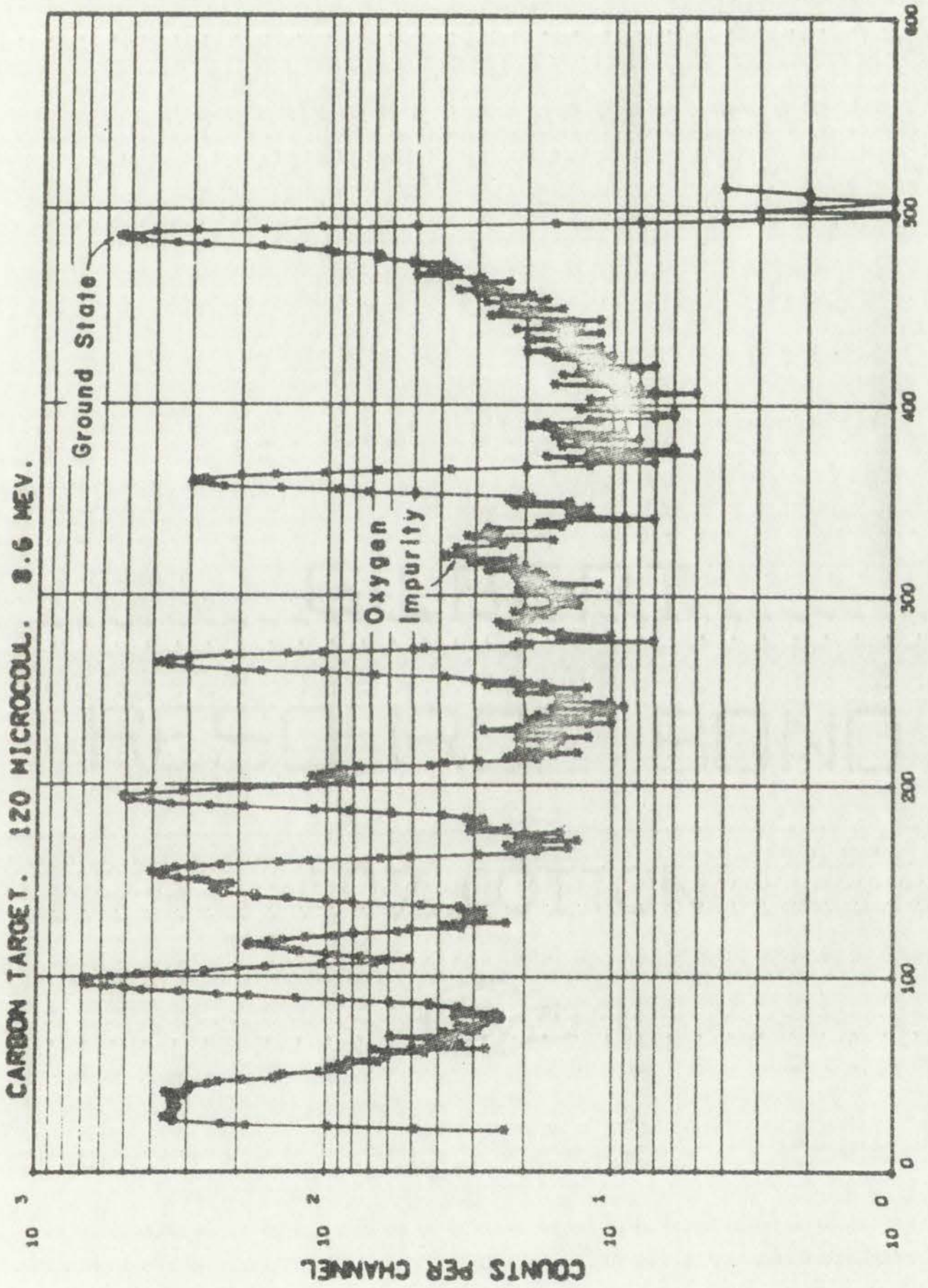

Fig. 20. Prompt proton pulse-height distribution from the carbon activation.

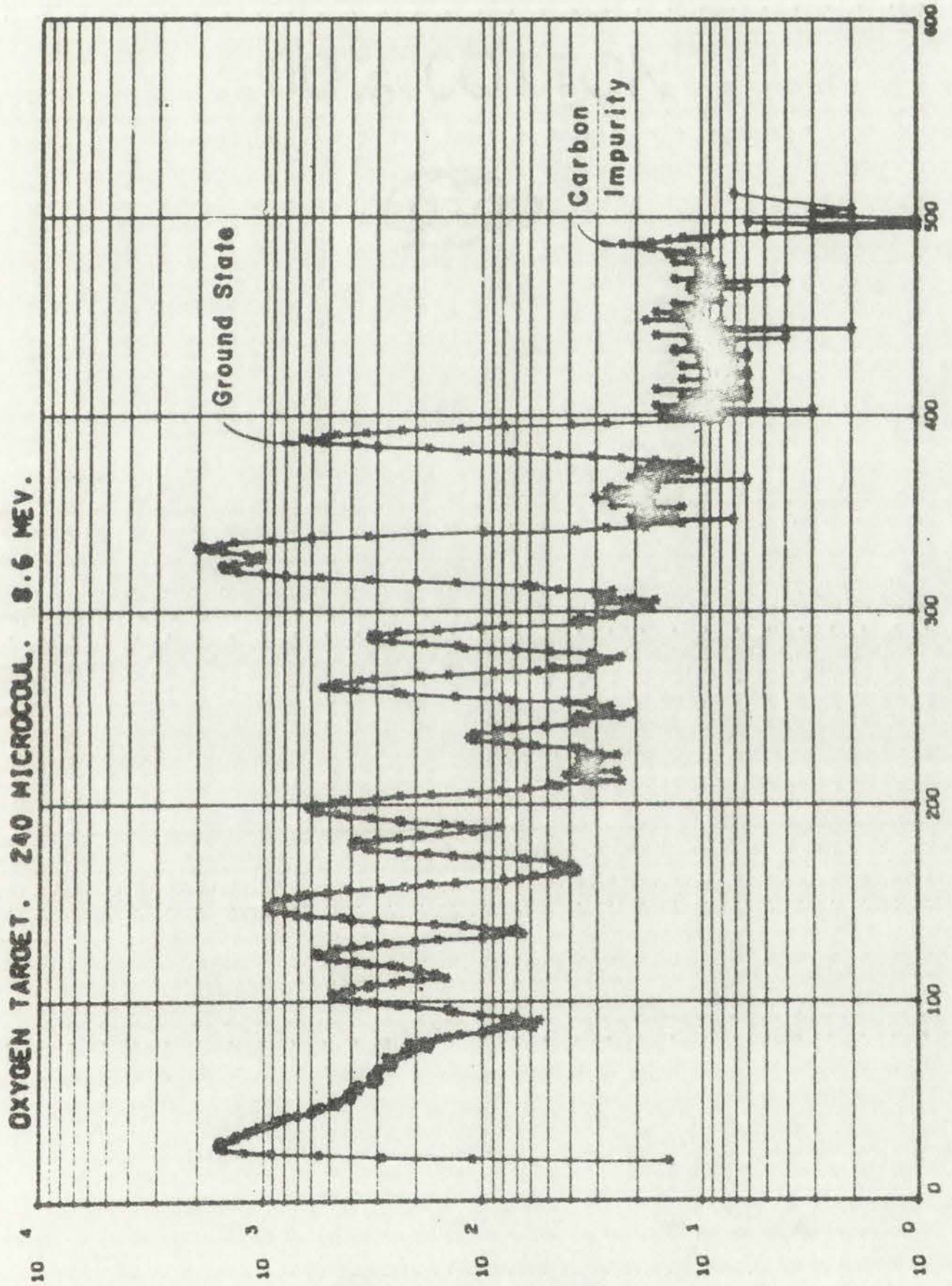

Fig. 21. Prompt proton pulse-height distribution from the oxygen activation.

Results

The thickness of the carbon layer on the carbon target was calculated to be 15.9 $\pm$ 0.9 $\mu g/cm^2$. The thickness of the Ta_2O_5 layer on the oxygen target was calculated to be 47.6 $\pm$ 2.8 μg-oxygen/cm^2. This latter value is 20% lower than that calculated from data presented by Kover and Musselin (Ref. 22). However, a direct comparison probably should not be made since the variations of layer thickness with temperatures and current densities are significant. There were insufficient data to make these corrections; however, the 20% lower thickness is an indication of the higher current density and higher temperature used in this experiment. Davies et al. (Ref. 23) report a 10% decrease in the oxide layer thickness as the current densities were increased from 0.1 mA to 10 mA. The peak current density used in this experiment was approximately 100 mA. A summary of these results is given in Table 3.

TABLE 3

RESULTS OF PASSIVE CALIBRATION†

	Carbon	Oxygen	Ta_2O_5
Thickness ($\mu g/cm^2$)	15.9 $\pm$ 0.9	47.6 $\pm$ 2.8	263.1
^{3}He energy loss (keV)* in layer at 8.6 MeV	6.9	---	54.1
Proton energy loss (keV)* in layer at 5.0 MeV	small	---	9.4

*Calculated using dE/dx data from Ref. 24

†The corresponding thicknesses that are consistent with the thick target data are 18.8 and 33.6 $\mu g/cm^2$.

CHAPTER IV

CALCULATIONS AND DATA ANALYSIS

Introduction

One of the objectives of this experiment was to determine the body concentrations of carbon and oxygen impurities in various materials including germanium, which is used in the manufacture of Ge(Li) detectors. In addition to the body concentrations, the surface concentrations of oxygen had to be determined because these materials readily oxidize when exposed to air. Some experimenters have bombarded the sample to be investigated with charged particles and then have removed the surface in small amounts. The amount of material removed and the activities present in this material are determined. These techniques can be used if the range of the bombarding particle is large compared to the recoil ranges of the reaction products; however, the short range of the ^{3}He particles used in this experiment and the large positive Q of the reactions cause ranges for the recoil atoms that are large enough to give erroneous results. This is particularly true for the bombardment of crystalline materials where channeling of the recoil atoms can greatly increase their range. These problems do not exist with the prompt activation analysis techniques that were used in this experiment.

Experiments using anodizable materials and controlled anodizing with chemical etching techniques to remove thin layers from the surface of the material have been quite successful (Ref. 9) in determining the recoil ranges of heavy ions incident on amorphous, polycrystalline, and single-crystalline materials.

The thin target excitation functions were determined with good resolution so that the various proton groups could be unfolded from the complex spectra. These complex proton spectra were unfolded using least-squares techniques similar to those presented in Ref. 25. The differences and additions to the code in order to unfold the proton spectra, instead of high-resolution gamma-ray spectra, are presented in Appendix D.

The thin carbon targets were approximately 19 $\mu g/cm^2$, and the thin oxygen targets were approximately 34 $\mu g/cm^2$. The solid angle of the silicon surface barrier detector was 3.08×10^{-3} sr.

Energy Loss Calculations

The energy of the ^3He particles versus distance traversed in the target and the energy of the reaction protons at the detector were determined using numerical techniques and stopping-power data from Refs. 26 and 24. The data from these references were based on observed experimental measurements and simple theoretical extrapolations guided by theoretical expectations.

The stopping-power data,

$$\frac{dE}{dx} = s(E) \quad ,$$

were interpolated using cubic spline functions. The cubic splines as they were used in the numerical representation of the stopping-power data are discussed in Appendix E. The objective of the numerical manipulation of the stopping-power data was to obtain the function $x = f(E)$ and the inverse function $E = F(x)$ for a 12-MeV particle incident on the material. Twelve MeV was chosen for the upper energy because it represented an upper bound for the particle energies of interest.

Figure 22 shows E = F(x) for ^{3}He particles and protons in germanium. The energy losses of the ^{3}He particles as they traversed the target material and the energy losses of the protons in the target and in the backscatter absorber foil were determined using the E = F(x) and x = f(E) interpolation functions in the following manner. All of the thick target energy loss data start with a particle energy of 12 MeV and stop when the particle energy reaches 1 MeV. These energies represented the upper and lower bounds on the particle energies of interest. If we were to determine the energy loss of an 8-MeV proton as it passes through a 100-μ germanium foil, the function x = f(8.0) would be evaluated to determine the initial x displacement, x_0, that gave an energy of 8.0 MeV. Then, the function E = F(x_0 + 0.01) would be evaluated to determine the proton energy after passing through the foil. These and similar calculations are performed for all energy loss calculations. The x displacements are in cm and the particle energies are in MeV.

Thin Target Excitation Functions

The thin target excitation functions for the various excited states from the $^{12}C(^{3}He,p)^{14}N$ and $^{16}O(^{3}He,p)^{18}F$ reactions were determined over the ^{3}He energy range of 2.5 to 9.0 MeV using thin oxygen and carbon targets. A computer code was then used to unfold the complex pulse-height distributions that were obtained from the reaction protons. This code was referred to as C24HE3P and is discussed in Appendix D. The results of the spectral unfolding of the carbon and oxygen spectra from the calibration irradiations discussed earlier are shown in Fig. 23 for carbon and in Fig. 24 for oxygen. The proton spectra were obtained at a ^{3}He particle energy of 8.6 MeV and a detector angle of 160°. The spectra are shown after the protons had passed through a 76.2-μ aluminum foil

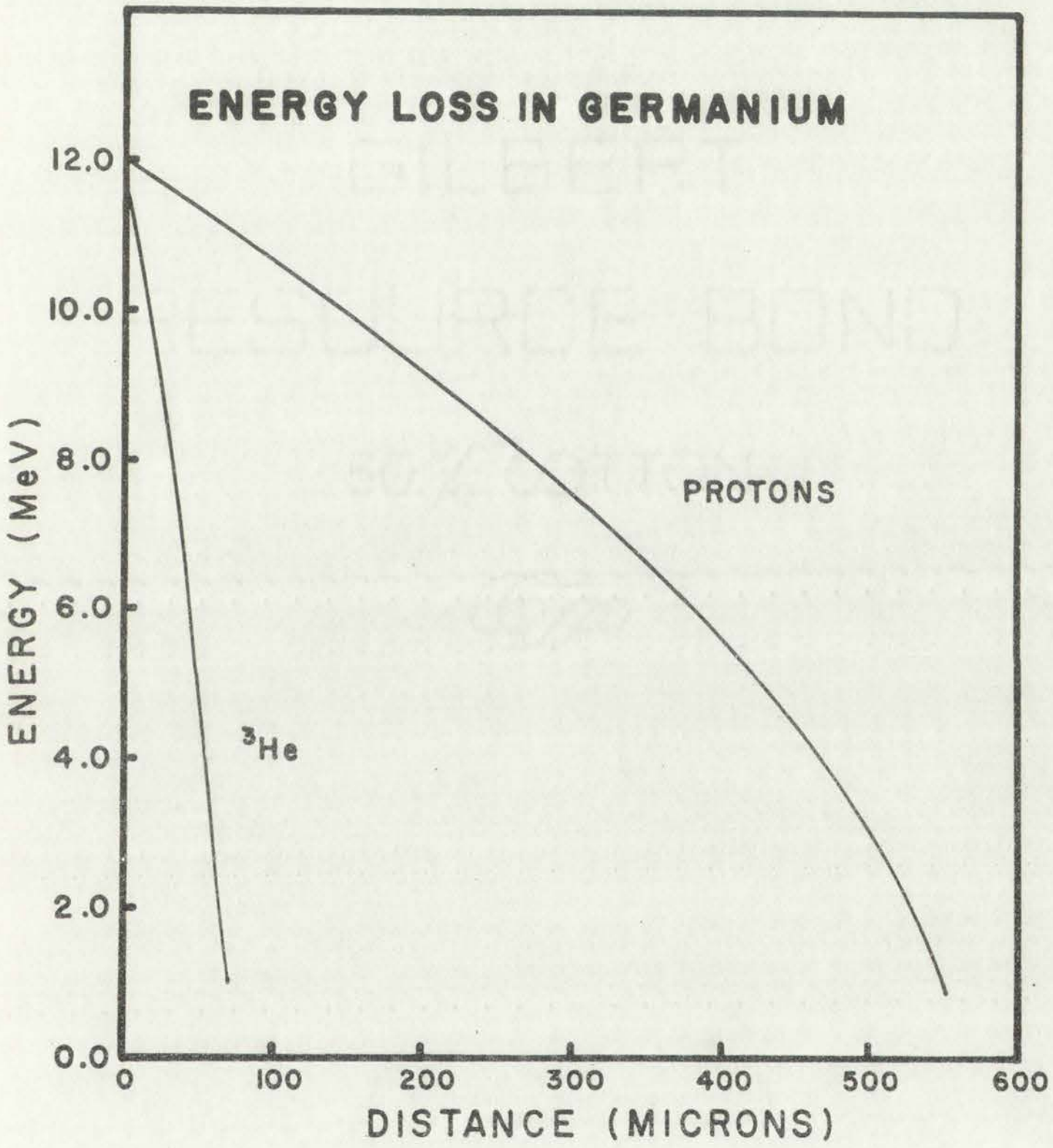

Fig. 22. Proton and ^{3}He energy loss in germanium.

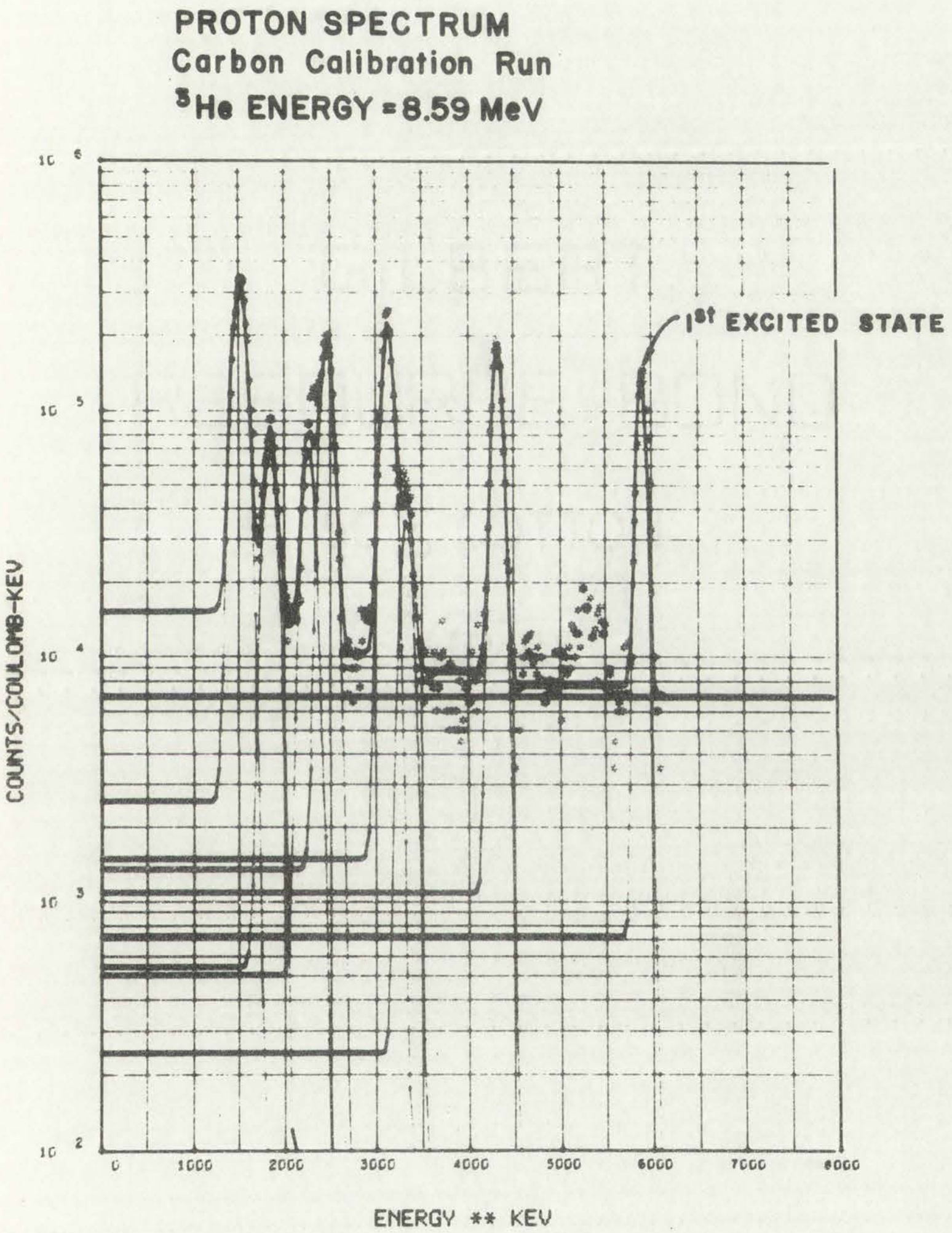

Fig. 23. Proton spectrum from the thin carbon calibration sample.

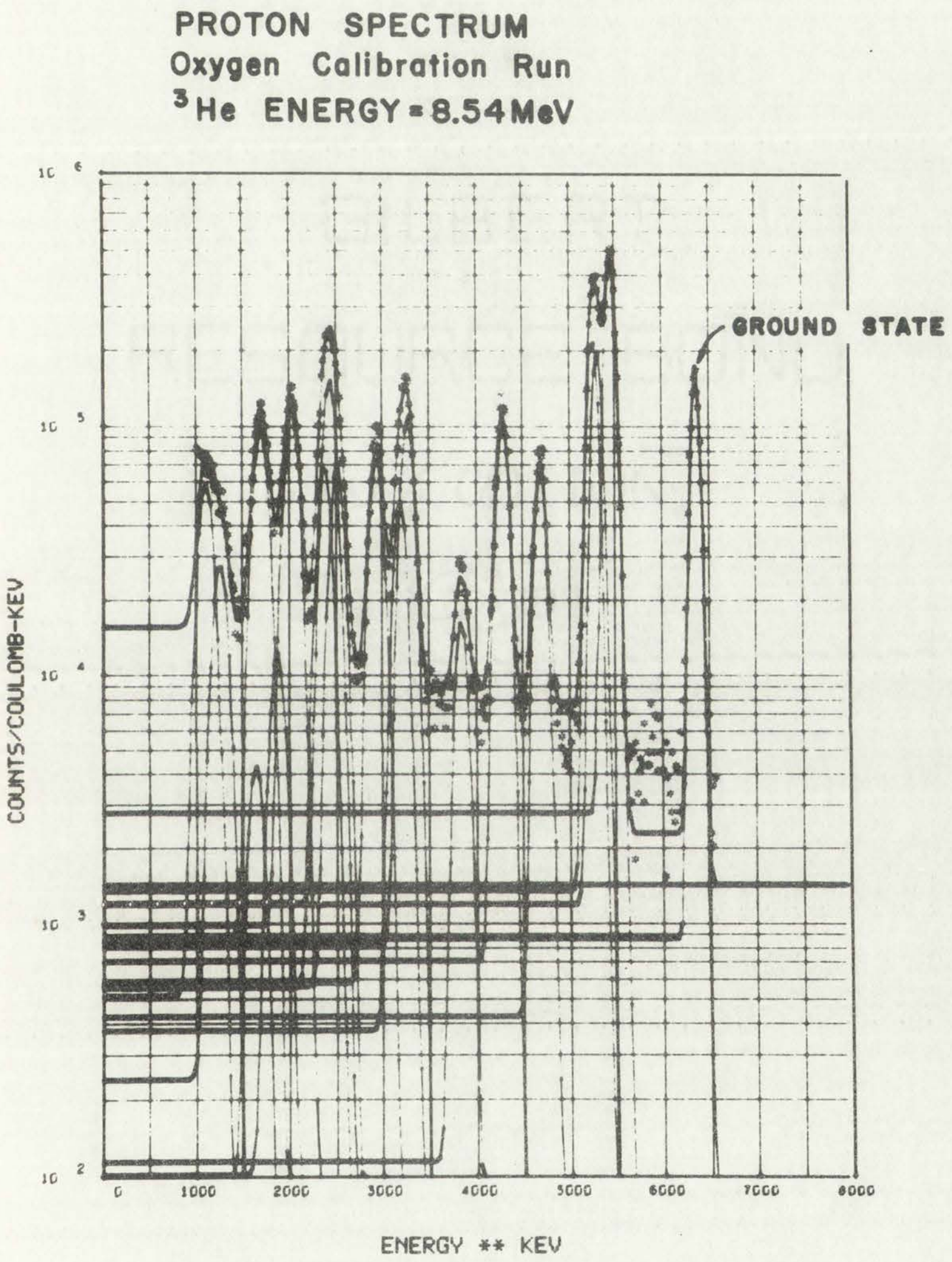

Fig. 24. Proton spectrum from the thin oxygen calibration sample.

that was used to prevent the backscattered ^{3}He particles from striking the detector. These proton spectra were unfolded from about 1 MeV to slightly above the ground-state peak. The proton spectrum for carbon shown in Fig. 23 is one of the few exceptions. In this case, the range of the ground-state proton exceeded the depletion depth of the detector and caused this peak to appear at a lower energy than expected. Therefore, it has not been considered in this analysis.

The thin target excitation functions for the first ten energy states of the $^{12}C(^{3}He,p)^{14}N$ reactions are presented in Figs. 25 through 27. The thin target excitation functions for the first twenty energy states of the $^{16}O(^{3}He,p)^{18}F$ reactions are presented in Figs. 28 through 32. The smooth lines through the data were obtained using cubic spline smoothing techniques. Resonance effects from the virtual energy levels in the compound nuclei are quite evident.

Nuclear Energy Levels

The reaction products, ^{14}N and ^{18}F, are sometimes left in an excited state and decay to the ground state by gamma-ray emission. Before kinematics can accurately calculate the proton energies, an accurate knowledge of these prompt gamma-ray energies is necessary. At the time the excitation functions were measured, published values for these gamma-ray energies were not well known. Therefore, the prompt gamma-ray spectra were recorded for many of the bombardments using a Ge(Li) detector system. The standard target chamber was designed so that such a detector could be placed close to the target (approximately 1 in. from the irradiated area) but outside the accelerator vacuum system with a minimum amount of absorbing material between the target and the detector. Typical pulse-height distributions from the prompt gamma rays are shown in Fig. 33 for a carbon irradiation

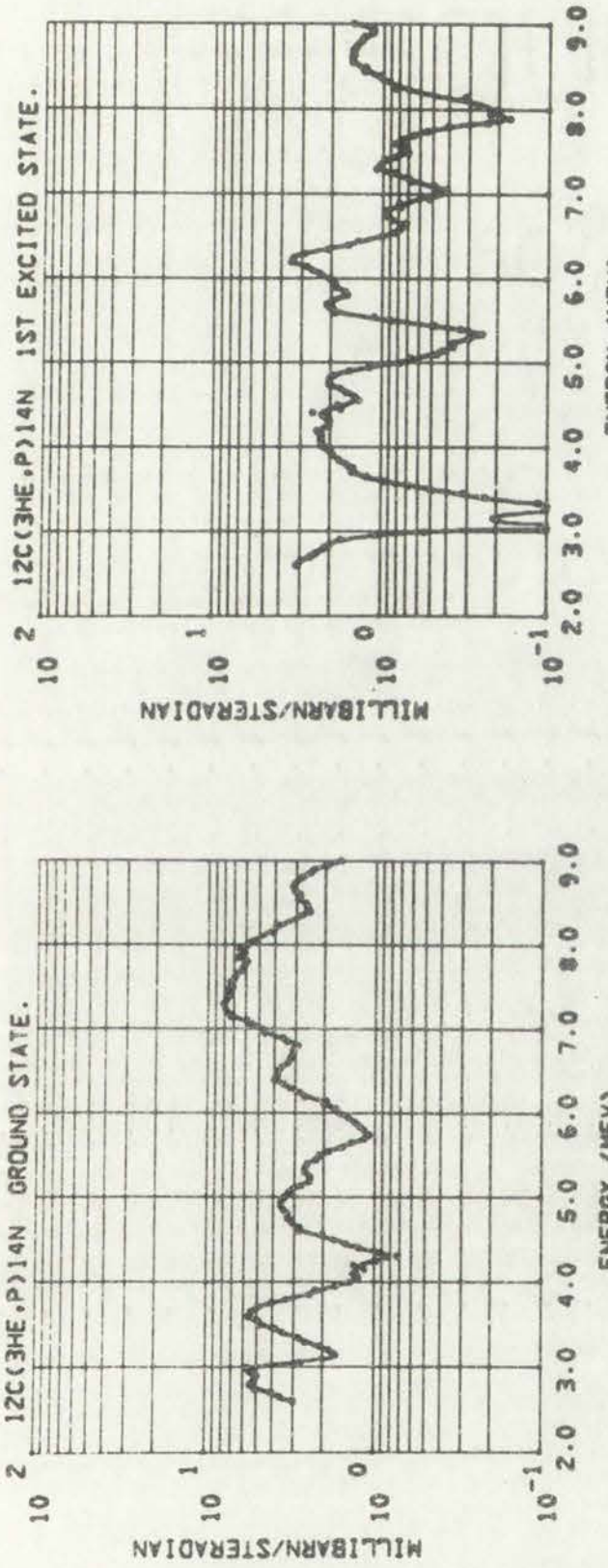

Fig. 25. Excitation functions for the ground state through the 3rd excited state for the $^{12}C(^{3}He,p)^{14}N$ reaction.

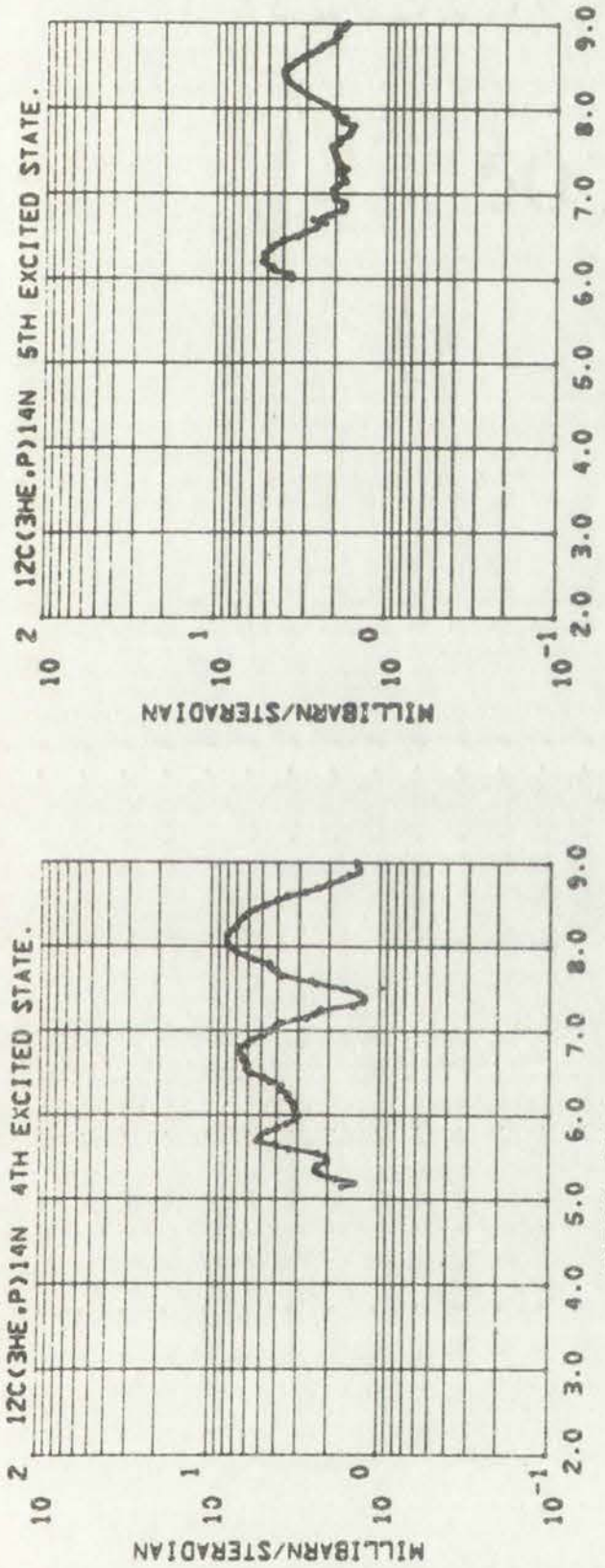

Fig. 26. Excitation functions for the 4th through 7th excited states for the $^{12}C(^{3}He,p)^{14}N$ reaction.

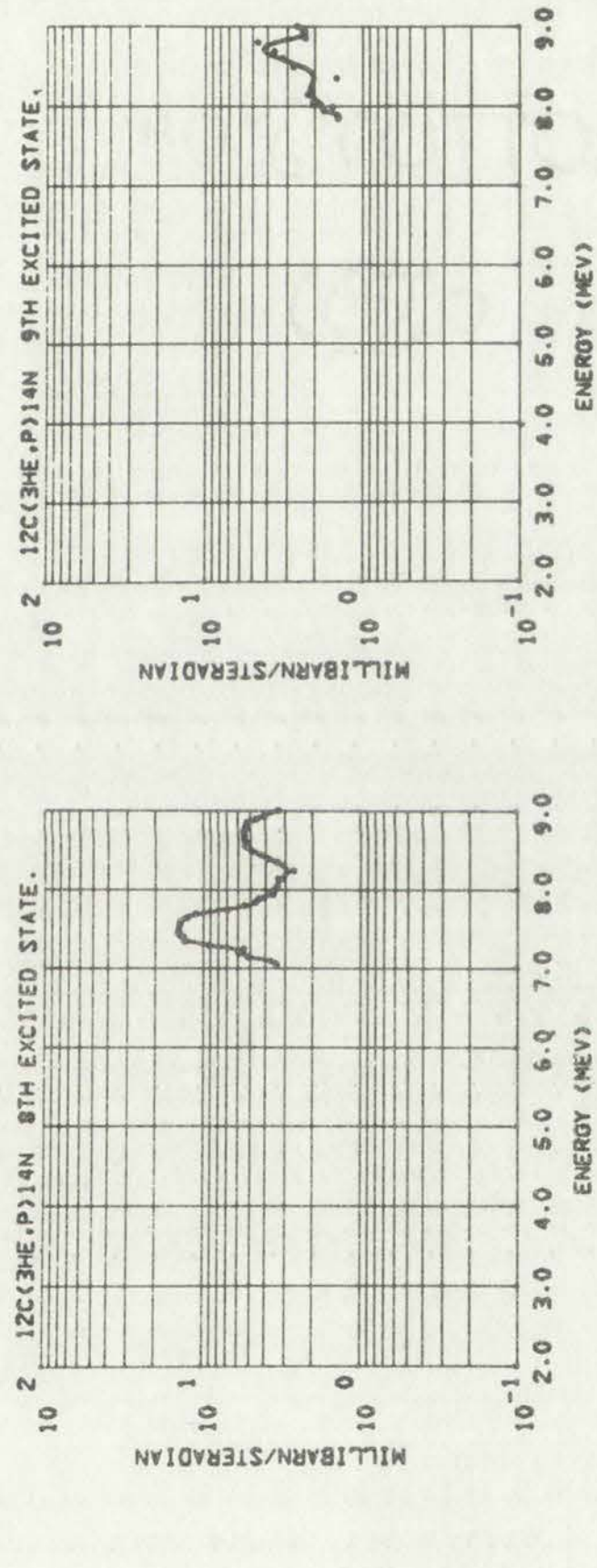

Fig. 27. Excitation functions for the 8th and 9th excited states for the $^{12}C(^{3}He,p)^{14}N$ reaction.

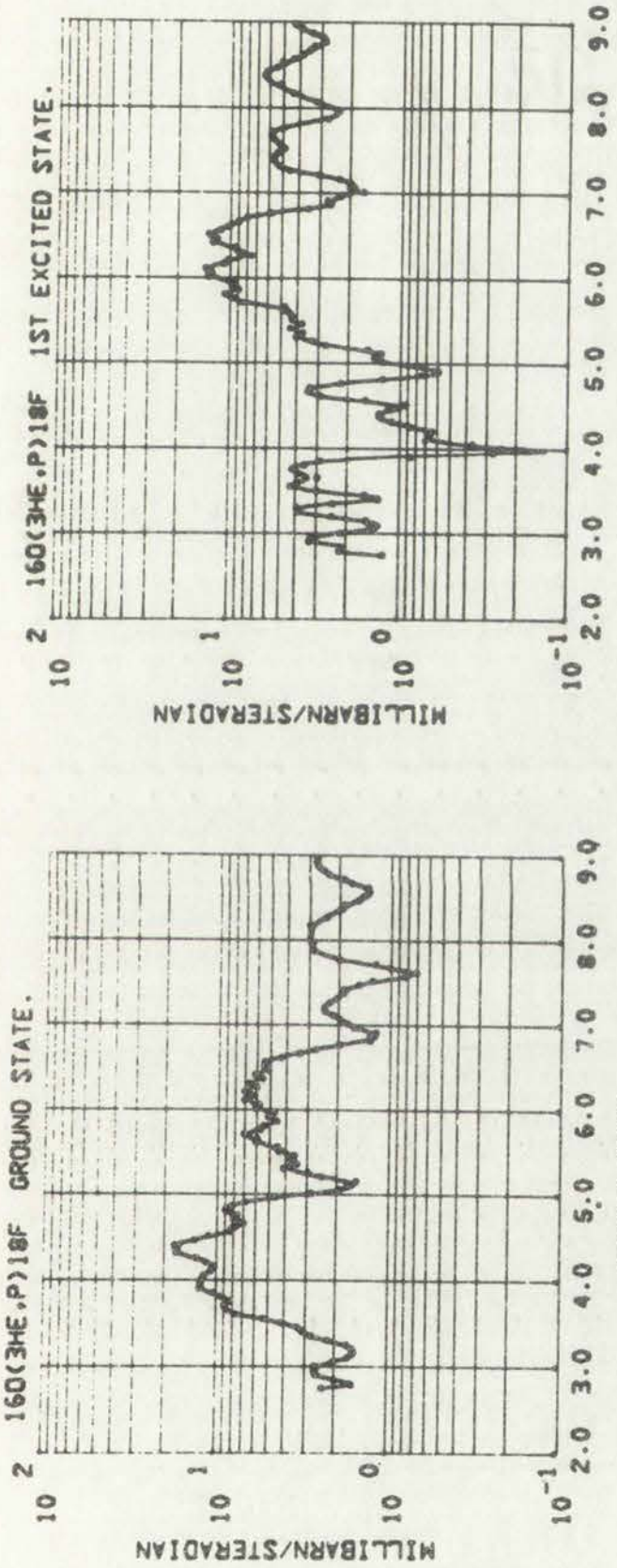

Fig. 28. Excitation functions for the ground state through the 3rd excited state for the $^{16}O(^{3}He,p)^{18}F$ reaction.

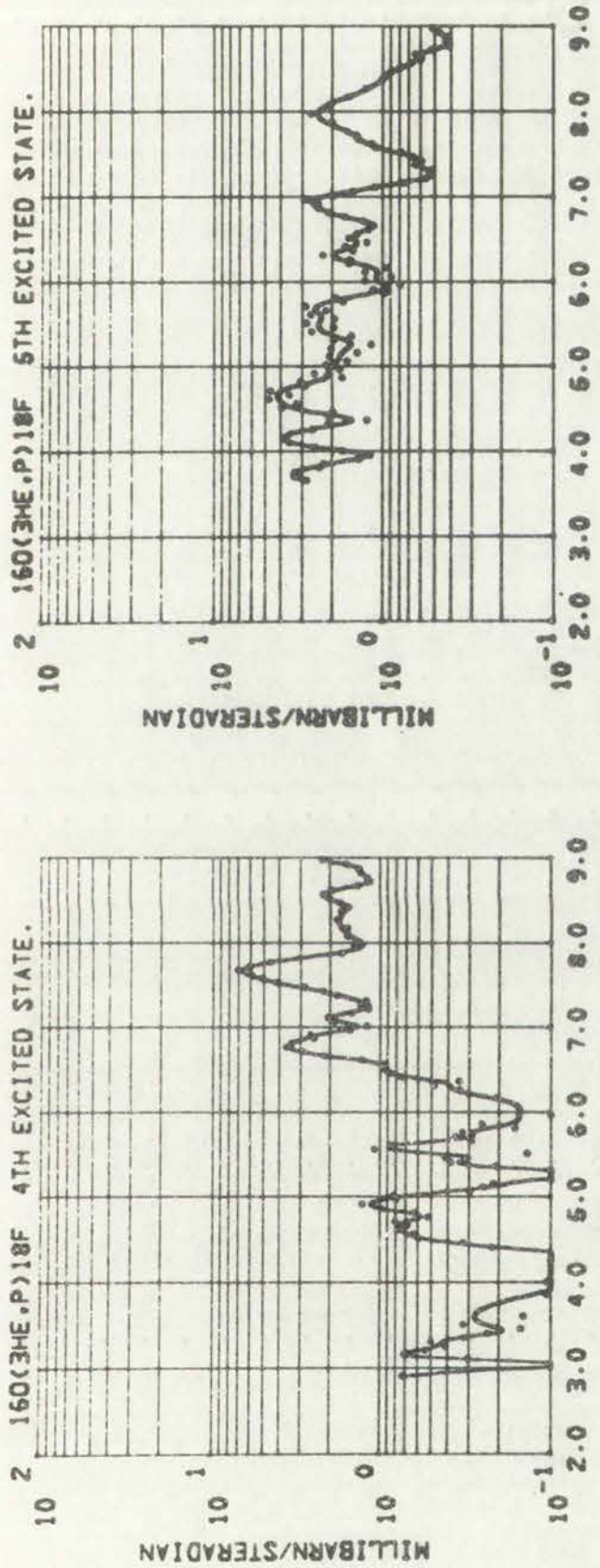

Fig. 29. Excitation functions for the 4th through 7th excited states for the $^{16}O(^{3}He,p)^{18}F$ reaction.

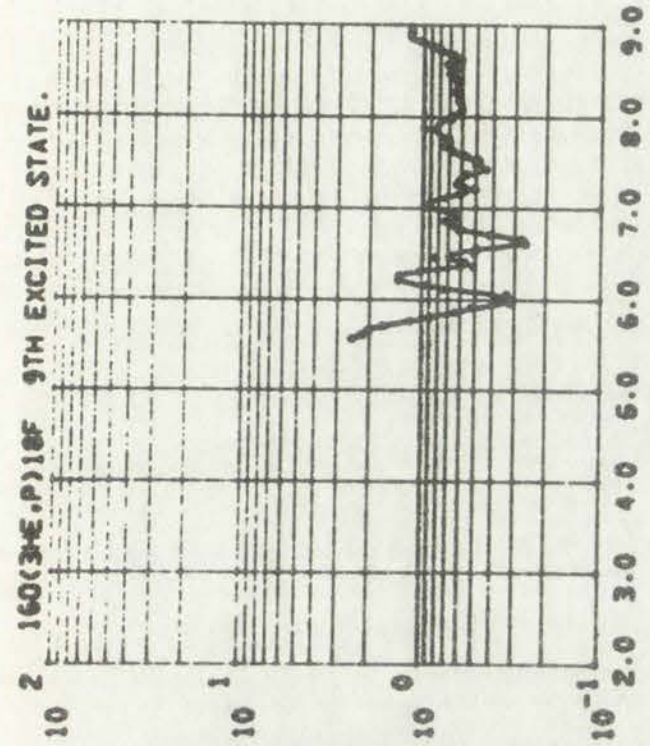

Fig. 30. Excitation functions for the 8th through 11th excited states for the $^{16}O(^{3}He,p)^{18}F$ reactions.

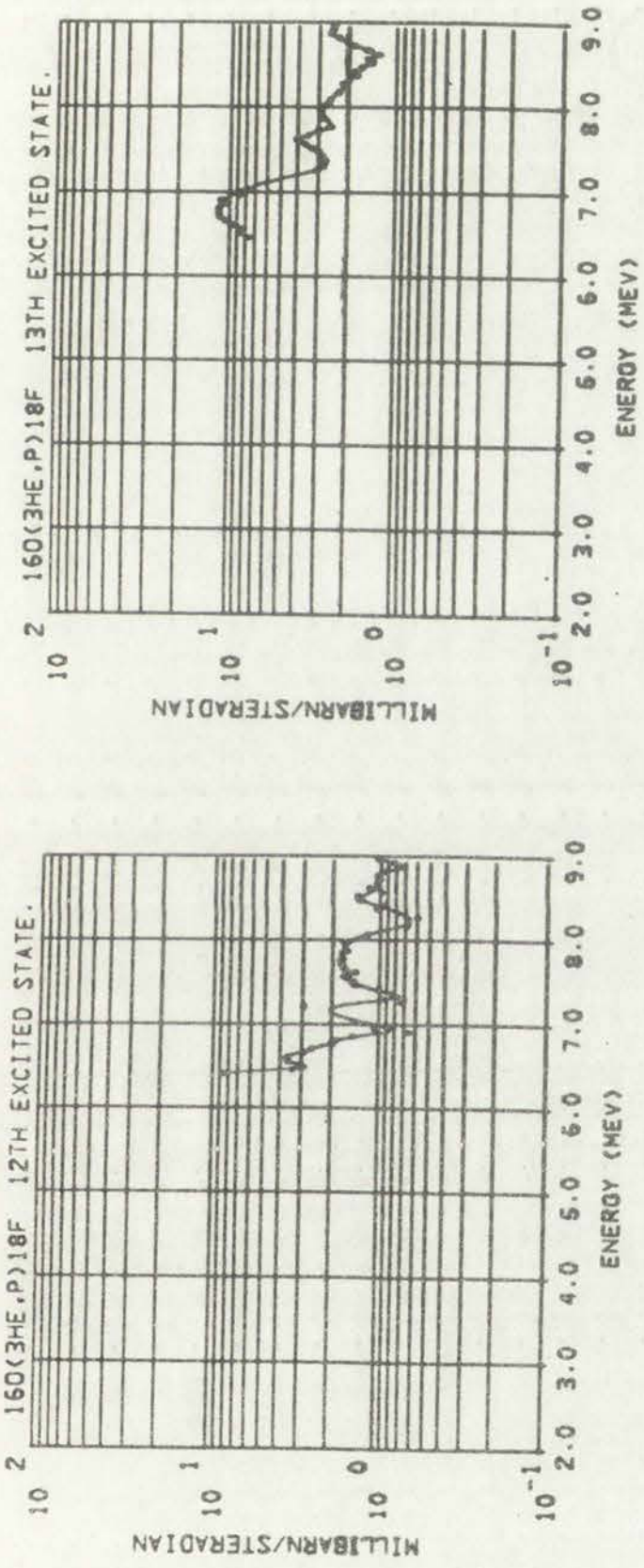

Fig. 31. Excitation functions for the 12th through 15th excited states for the $^{16}O(^{3}He,p)^{18}F$ reaction.

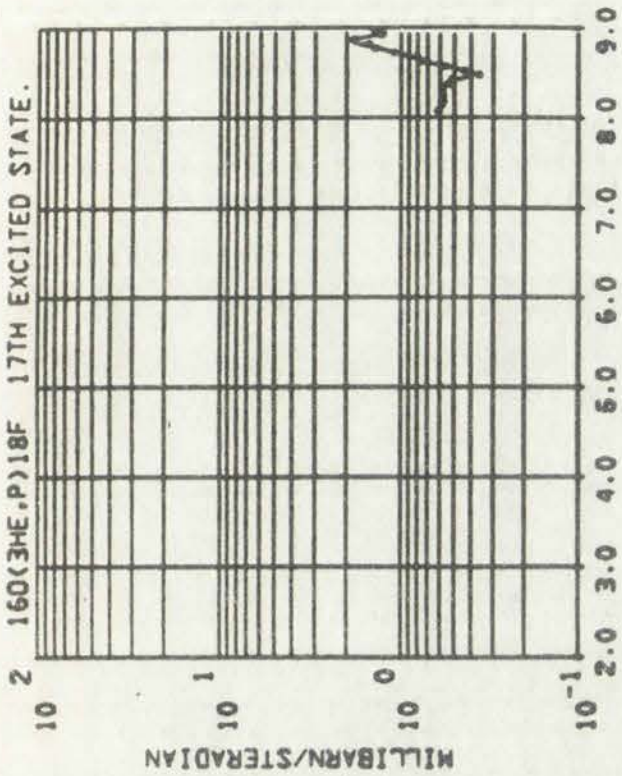

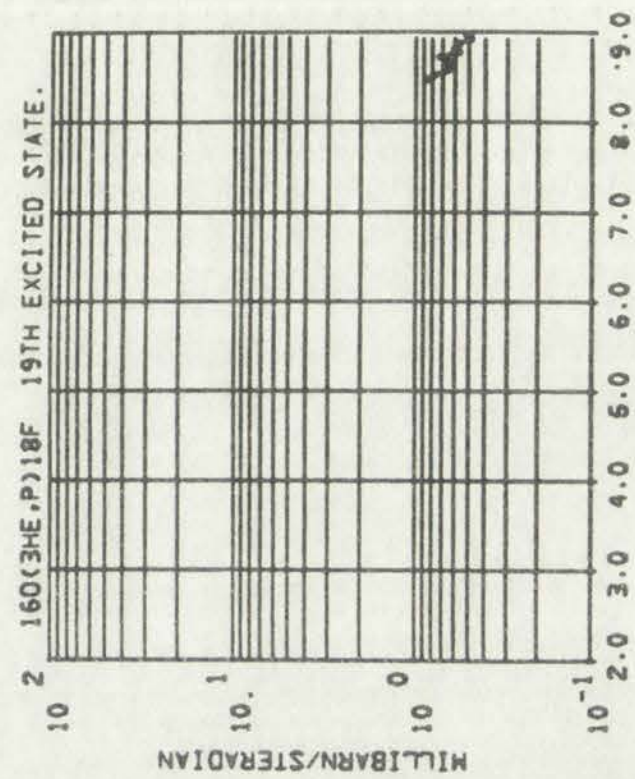

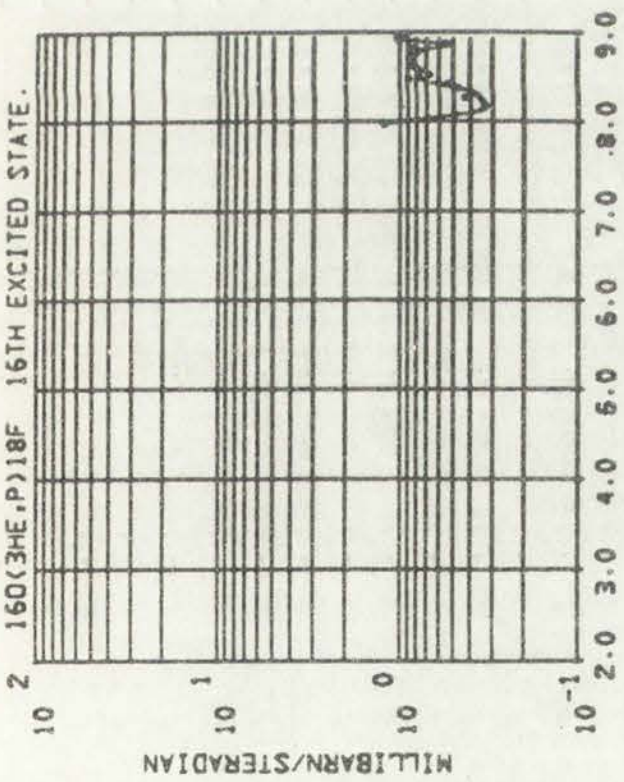

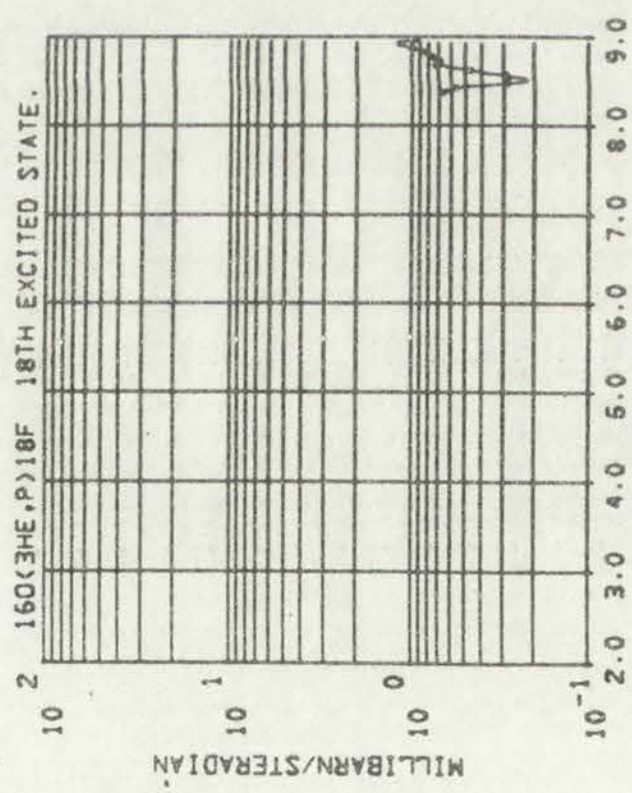

Fig. 32. Excitation functions for the 16th through 19th excited states for the $^{16}O(^{3}He,p)^{18}F$ reaction.

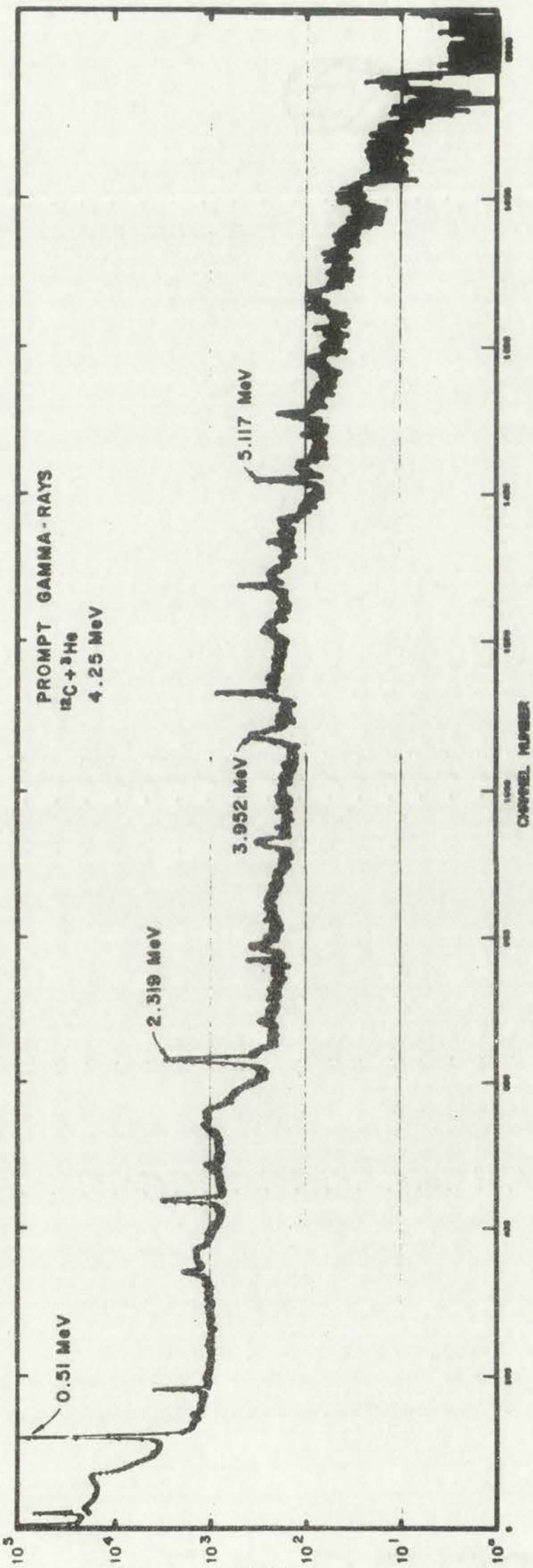

Fig. 33. Prompt gamma-ray spectrum from a carbon irradiation.

and in Fig. 34 for an oxygen irradiation. The resolution of the detector system (normally 5.0 keV FWHM for 1.33 MeV gamma rays) is degraded some by the high count rate. The full-energy peak intrinsic efficiency of the detector was 4.5% at 1.33 MeV. The total $^{3}He^{++}$ charge for these data was 4.0×10^{-5} C.

Recent publications, Refs. 27 and 28, give values for these energy levels that are consistent, within the experimental limits, with the proton spectra and also with the prompt gamma-ray data obtained in this experiment. The energy levels used in the unfolding of the proton spectra are listed in Table 4.

TABLE 4

NUCLEAR LEVELS IN ^{14}N AND ^{18}F

^{14}N Levels[a] (MeV)	^{18}F Levels[b] (MeV)
0.0	0.0
2.319	0.937
3.952	1.043
4.927	1.081
5.117	1.131
5.713	1.701
5.885	2.101
6.224	2.524
6.468	3.060
7.036	3.134
	3.358
	3.724
	3.790
	3.839
	4.115
	4.231
	4.361
	4.400
	4.651
	4.741

[a] Ref. 27
[b] Ref. 28

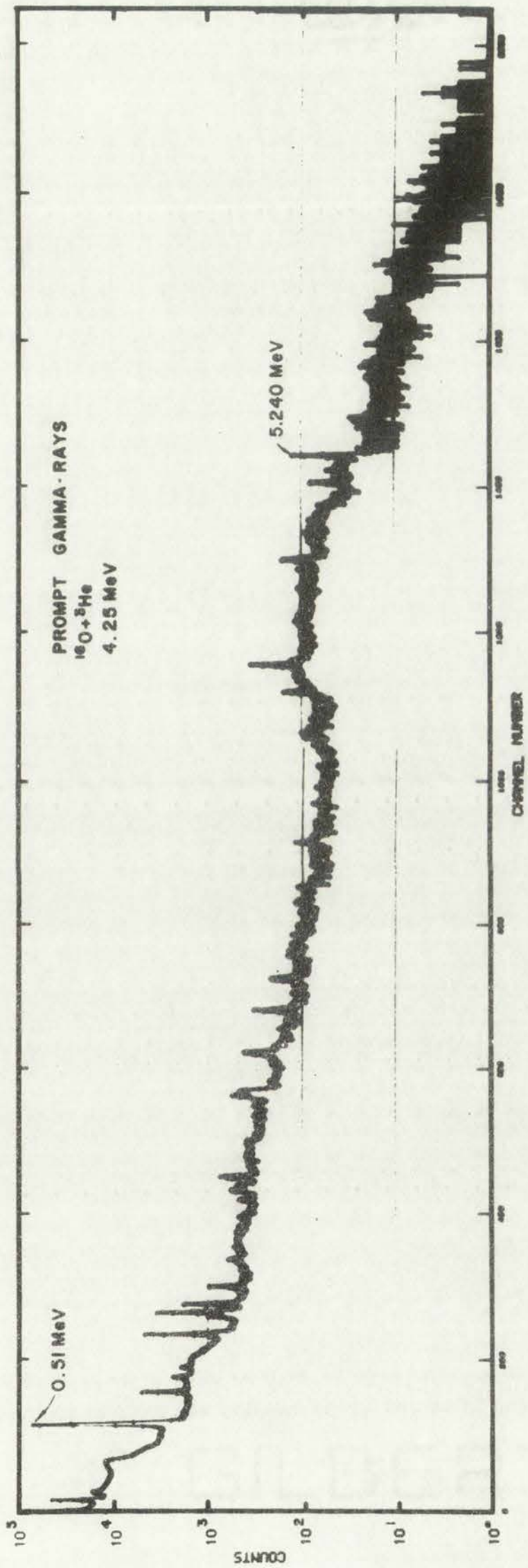

Fig. 34. Prompt gamma-ray spectrum from an oxygen irradiation.

Interpolation and Smoothing with Cubic Splines

Cubic splines have been used to interpolate and also to smooth the experimental data. A derivation of the cubic spline function, as it was used in the codes presented in this paper, is given in Appendix E. A more detailed presentation can be found in several books that are published on the subject (e.g., Ref. 29). The cubic spline functions were used to analytically represent the energy of the charged particles versus depth of material penetrated, $E = F(x)$, and the inverse of this function, $x = f(E)$. These functions were used extensively to determine the charged-particle energy losses and the depth of material penetrated for a given reaction energy.

Interpolatory cubic splines in smoothing experimental data, e.g., to calculate a smooth line through a set of data containing statistical fluctuations, have been quite useful. The data is smoothed by interpolating a value (y_i^e) using an odd number of data points. The smoothed data point becomes

$$y^e_{i,j} = 2/3\ y^e_{i,j-1} + 1/3\ y^e_{i,j} \quad ,$$

where the superscript refers to the smoothed data, the i subscript refers to the ith data point, and the j subscript refers to the number of times the data point has been smoothed. The smoothed function and the original data are shown in Fig. 35 for a small region of a 4096-channel gamma-ray spectrum. The data were smoothed ten times to give the smoothed function. This type of data smoothing is quite stable even with very poor statistics, does not produce the oscillations common in smoothing done with high-order polynomials, and does not smooth away small satellite peaks.

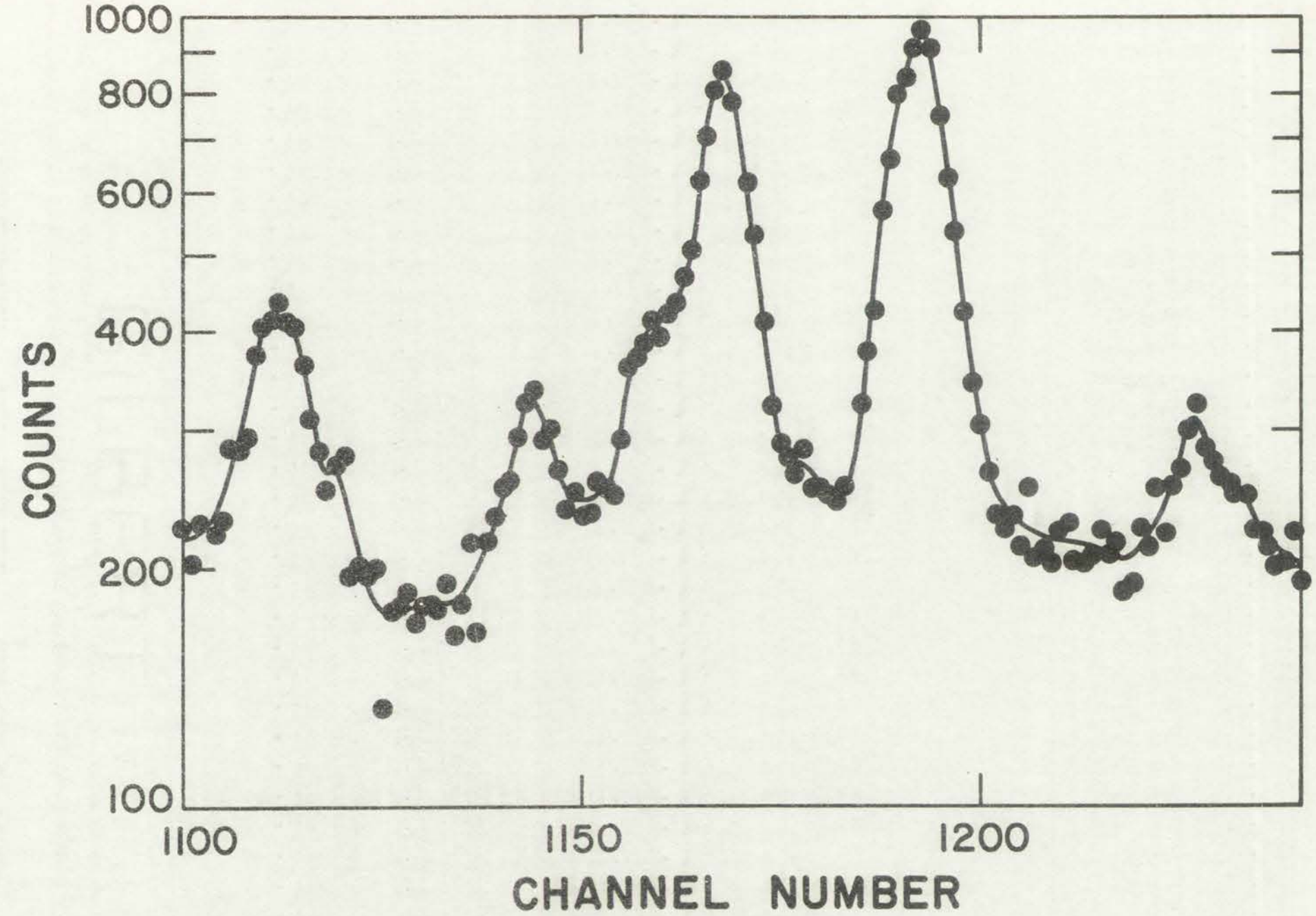

Fig. 35. Pulse-height distribution that was smoothed with cubic splines.

The excitation function data presented in Figs. 25 through 32 were smoothed using these techniques. These data were smoothed three times using seven data points. These smoothed spline functions were used to represent the excitation functions in the computer calculations of the impurity distributions in the thick targets.

Nuclear Reaction Kinematics

The reaction kinematics are shown schematically in Fig. 36. M_1 refers to the incident particle mass, which, for this experiment, was that of ^{3}He; M_2 refers to the target mass, which, for this experiment, was that of either carbon or oxygen; M_3 refers to the light reaction product, which, for this experiment, was a proton; and M_4 refers to the heavy reaction product. Psi is the laboratory angle, and θ is the center-of-mass angle of the light product.

The kinematics equations needed to calculate the energy of the reaction protons as a function of angle and ^{3}He energy are those of Jarmie and Seagrave given in Ref. 30. The expression used to calculate the proton energy was

$$E_3 = E_1 \cdot B[\cos \Psi \pm (D/B - \sin^2 \Psi)^{\frac{1}{2}}]^2 \quad ,$$

where

$$B = \frac{M_1 M_3 (E_1/E_t)}{(M_1 + M_2)(M_3 + M_4)} \quad ,$$

$$D = \frac{M_2 M_4}{(M_1 + M_2)(M_3 + M_4)} \left(1 + \frac{M_1 Q}{M_2 E_t}\right) \quad ,$$

Ψ = laboratory angle of the light product,

E_3 = proton energy,

E_1 = ^{3}He energy,

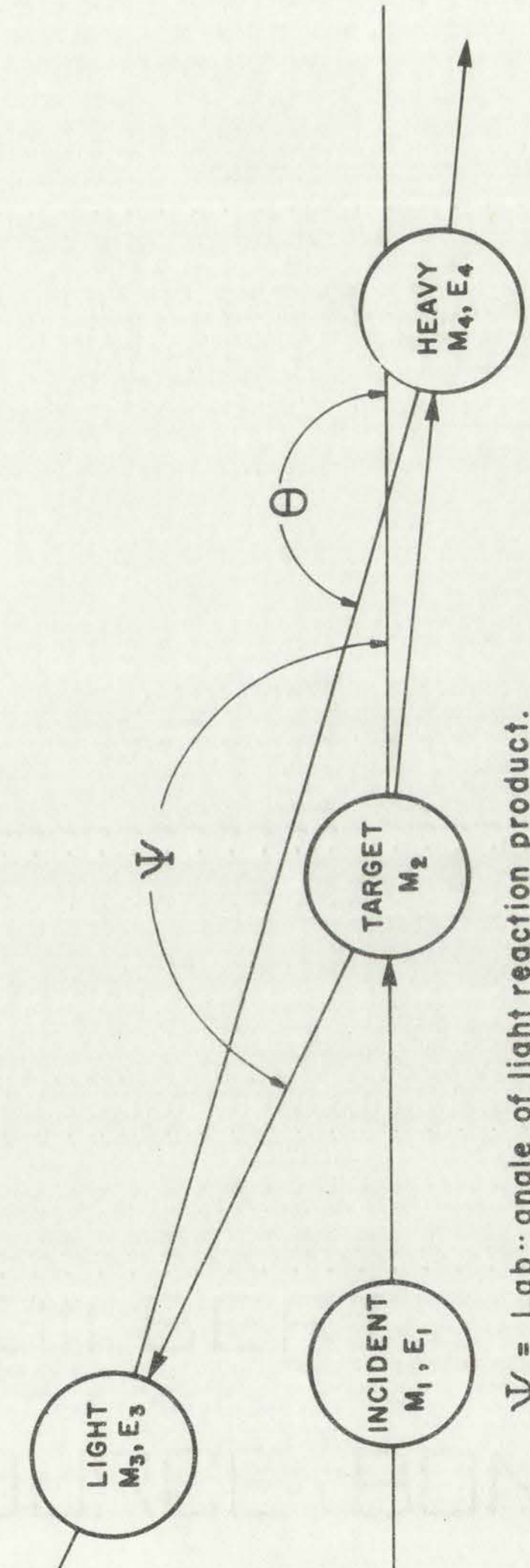

ψ = Lab angle of light reaction product.

θ = c.m. angle of light reaction product.

Fig. 36. Reaction kinematics for experimental geometry.

$$Q = Q_{gs} - E_{\gamma}$$

Q_{gs} = ground-state Q = 4.7786 MeV for carbon

= 2.0334 MeV for oxygen,

E_{γ} = prompt gamma-ray energy, and

$E_t = E_1 + Q$.

Another expression from Ref. 30,

$$Q = \frac{M_3 + M_4}{M_4} E_3 - \frac{M_4 - M_1}{M_4} E_1 - \frac{2(M_1 M_3 E_1 E_3)^{\frac{1}{2}}}{M_4} \cos \Psi ,$$

was used to calculate the prompt gamma-ray energies from the iterated proton energies in the C24HE3P code, Appendix D.

It is helpful in understanding the kinematics of these reactions to be able to visualize the proton energies for the various states as a function of the incident ^{3}He energy. These data are shown in Fig. 37 for several states of the $^{12}C(^{3}He,p)^{14}N$ reaction. Similar data are shown for the $^{16}O(^{3}He,p)^{18}F$ reaction in Fig. 38. These kinetmatics data coupled with the excitation function data and the stopping-power data were used to calculate the thick target response of the proton detector for various geometries.

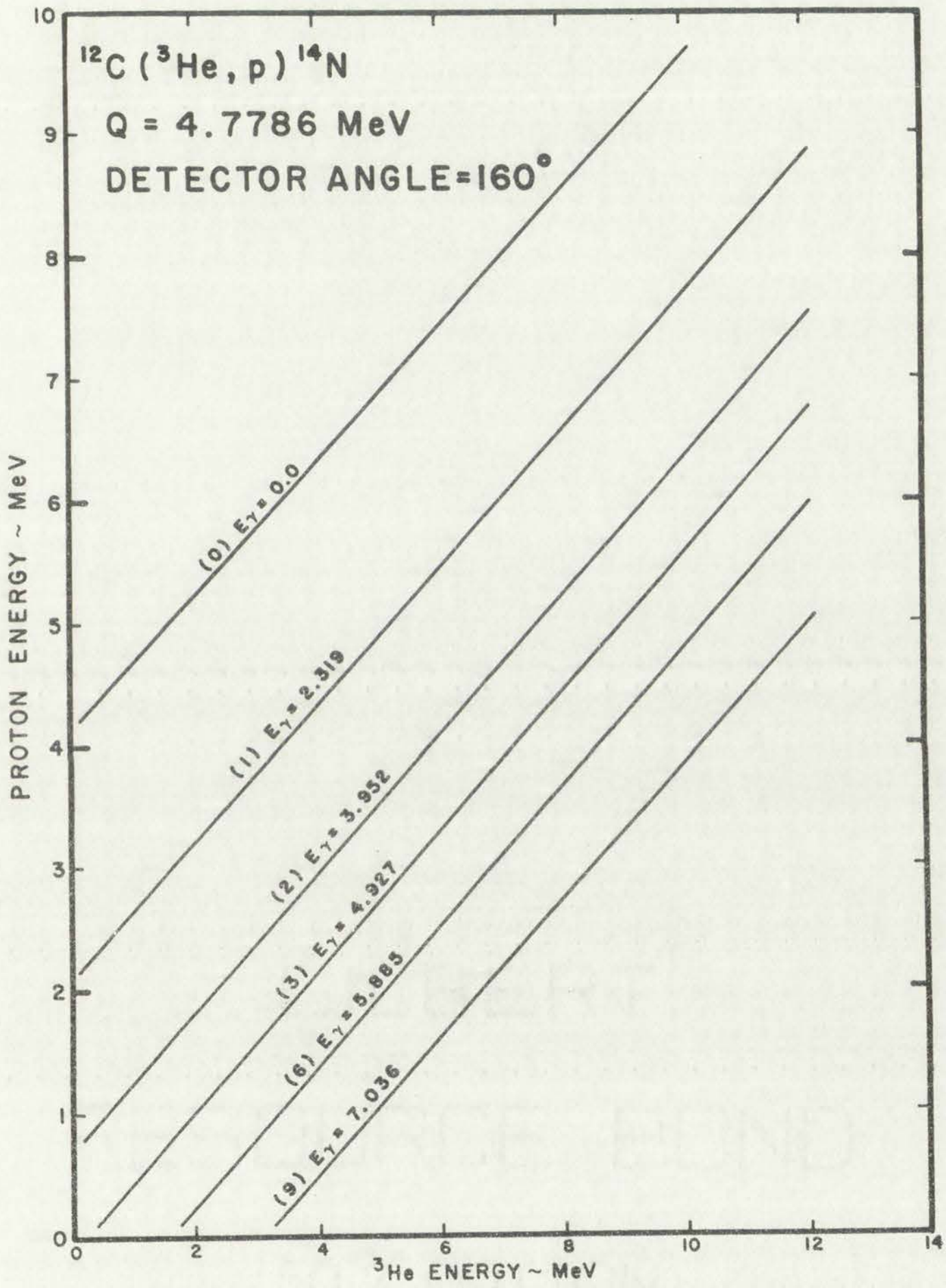

Fig. 37. Reaction proton energy versus ^{3}He energy for the $^{12}C(^{3}He,p)^{14}N$ reaction at 160°.

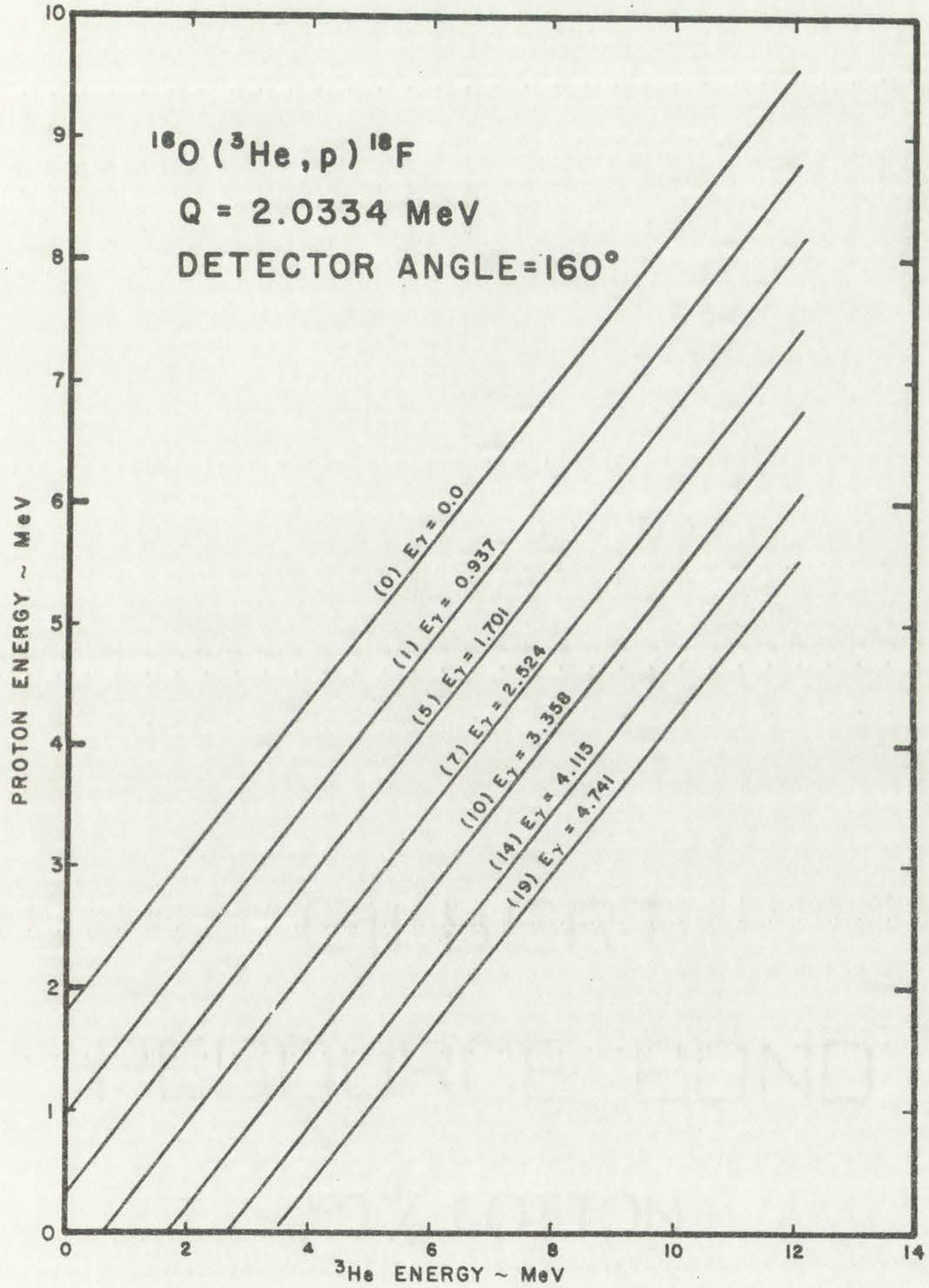

Fig. 38. Reaction proton energy versus ^{3}He energy for the $^{16}O(^{3}He,p)^{18}F$ reaction at 160°.

CHAPTER V

CHANNELING

Introduction

The concept of channeling dates back to 1912 when Johannes Stark contemplated the existence of open channels in crystalline materials and their possible effects on hydrogen ion bombardments. However, the experimental techniques of his day were not adequate to demonstrate channeling phenomena. It was not until 1963, after work on computer analyses of trajectories of energetic atoms in single crystals was published (Ref. 31), that there has been renewed interest in channeling phenomena. Since then, the theoretical and experimental studies on channeling have been extensive (Refs. 32 through 38).

Channeling can occur in either polycrystalline or single-crystal materials when the velocity of the particles is in a direction that is nearly parallel to one of the major crystal axes or planes. Repulsive coulomb forces can gently steer the particles between the rows or planes of nuclei and channeling effects become quite large. The channeled particles travel through regions of lower electron densities, and there are fewer ionizing collisions causing an increase in the particle range. This increase in the particle range can be quite significant for heavy ions.(Ref. 9) and is only about a factor of two for the lighter ions. The number of hard collisions and encounters that occur near the nuclei, such as large angle Rutherford scatter and nuclear reactions, are decreased for channeling trajectories. However, there is a transition region between the channeling trajectories and the nonchanneling

trajectories where the crystal nuclei are able to steer the incident particles so that the number of hard collisions and encounters that occur near the nuclei are increased. The particle trajectories for these three orientations are shown schematically in Fig. 39.

It is important that the experimentalist be aware of these phenomena if he is doing activation analyses of polycrystalline or single-crystal materials. For channeling orientations, the effective range of the incident particles is increased, and the activation of randomly located interstitial impurities will be increased. Similarly, if the impurities are substitutional, the number of activations will decrease if the sample is bombarded in a channeling direction. This decrease will be somewhat larger than the increase expected for interstitial impurities.

If the interstitial impurities are located in a unique location in the crystalline structure, bombardment in a direction parallel with one crystal axis might cause an increase in the number of activations, while bombardment in a direction parallel to another crystal axis might cause a decrease in the number of activations relative to a bombardment in a nonchanneling orientation. One of the objectives of this experiment was to irradiate crystalline materials in channeling and nonchanneling orientations with ^{3}He ions to determine the locations and amounts of carbon and oxygen impurities.

Channeling Experiments with Single-Crystal Thoria

Channeling data were obtained from single-crystal thoria samples. Preparation of the single-crystal thoria samples is given in Ref. 39. These thoria channeling data show both the backscatter channeling effects discussed in Chapter II and also the effect that channeling has on the reaction protons from the $^{16}O(^{3}He,p)^{18}F$ reaction. The high-energy

ION PATHS IN AN ORDERED LATTICE

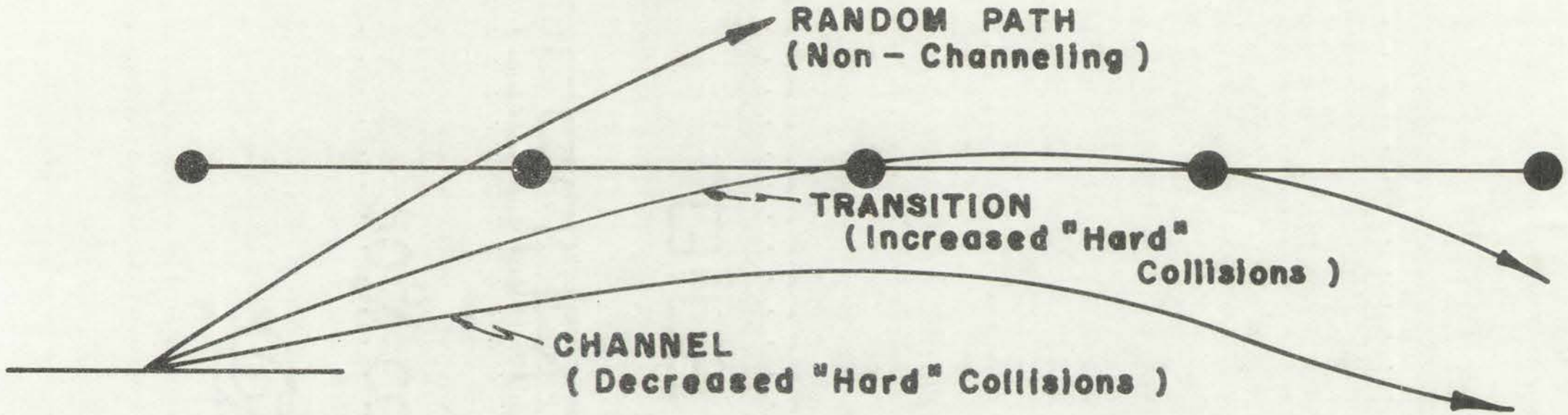

Fig. 39. Ion paths in an ordered lattice.

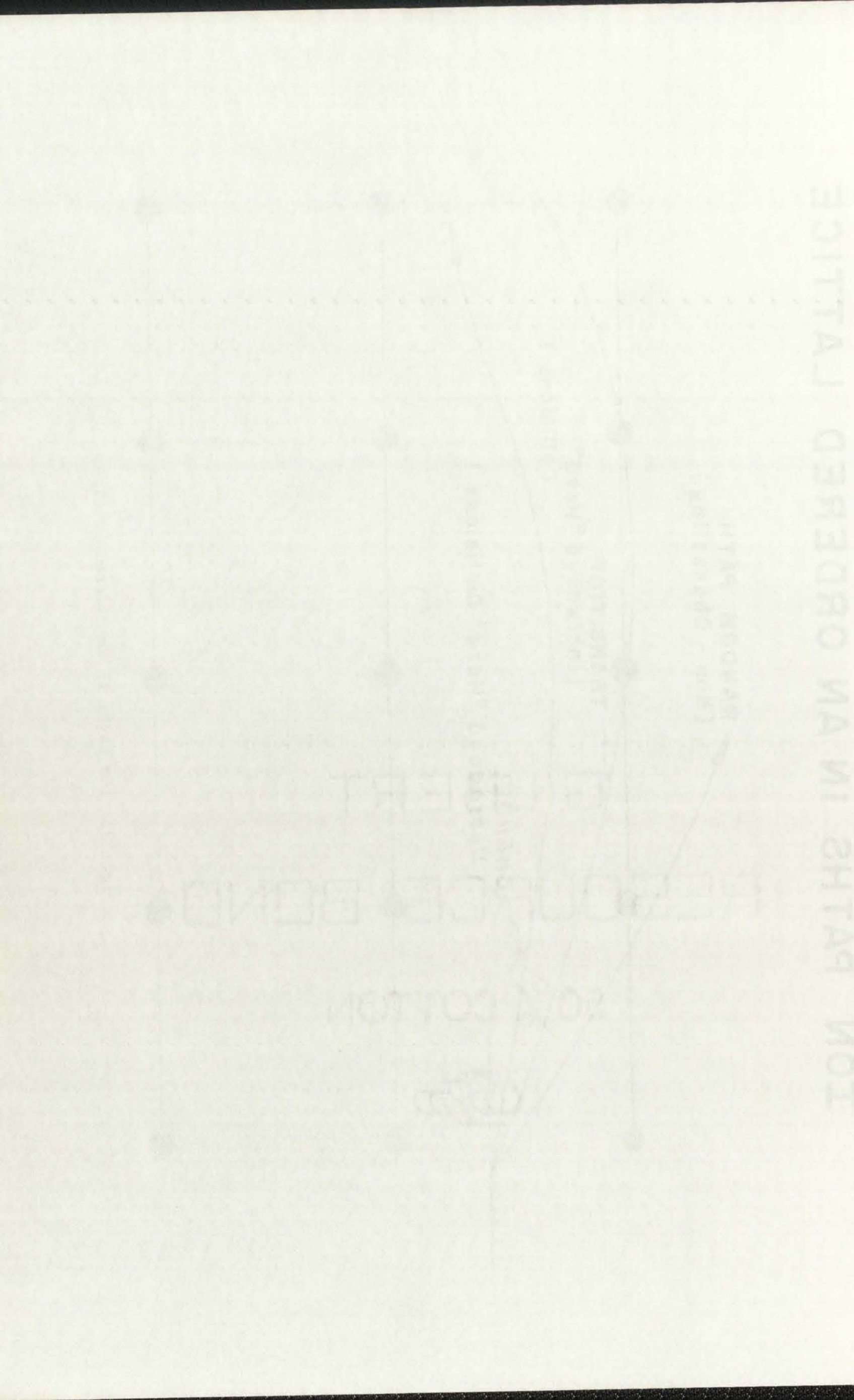
ORDERED LATTICE
NOT DISTRIBUTIVE

backscatter data is from the thorium atoms, and the reaction protons are from interactions with the oxygen atoms in the crystalline material. These reaction proton data show quite clearly the results that are expected from the oriented bombardments of a crystalline matrix containing substitutional oxygen impurity atoms.

The backscatter techniques can be used to study the locations of the thorium atoms, and the prompt proton techniques can be used to study the locations of the oxygen atoms. These techniques could be used to investigate the defects in the crystal or to investigate the displaced atoms in the crystal after radiation damage to the crystal structure.

The thoria crystals, because of their small size, had to be mounted and then masked with a material that would not cause interfering reactions. This mask was to prevent the incident ^{3}He particles from striking the epoxy that was used for mounting the crystal on the goniometer. The mask area was approximately 1.2 mm^2 and triangular in shape. Copper was chosen for the mask material. Its atomic weight was low enough that the backscatter from the copper did not interfere with the high-energy portion of the backscatter spectrum from the thorium. Also, the atomic number of copper is high enough that its coulomb barrier prevented interference from (^{3}He,px) reactions with the copper. Interference from low-Z impurities in the copper was negligible. The goniometer target chamber was used for these irradiations. All of the spectral data presented on the thoria irradiations were for the same number of incident particles.

Normal backscatter techniques were used to align the thoria crystal so that the $\langle 111 \rangle$ axis was parallel with the beam. Backscatter spectra are shown for nonchanneling and channeling orientations in Fig. 40. The lighter copper atoms contribute only to the low-energy region of these

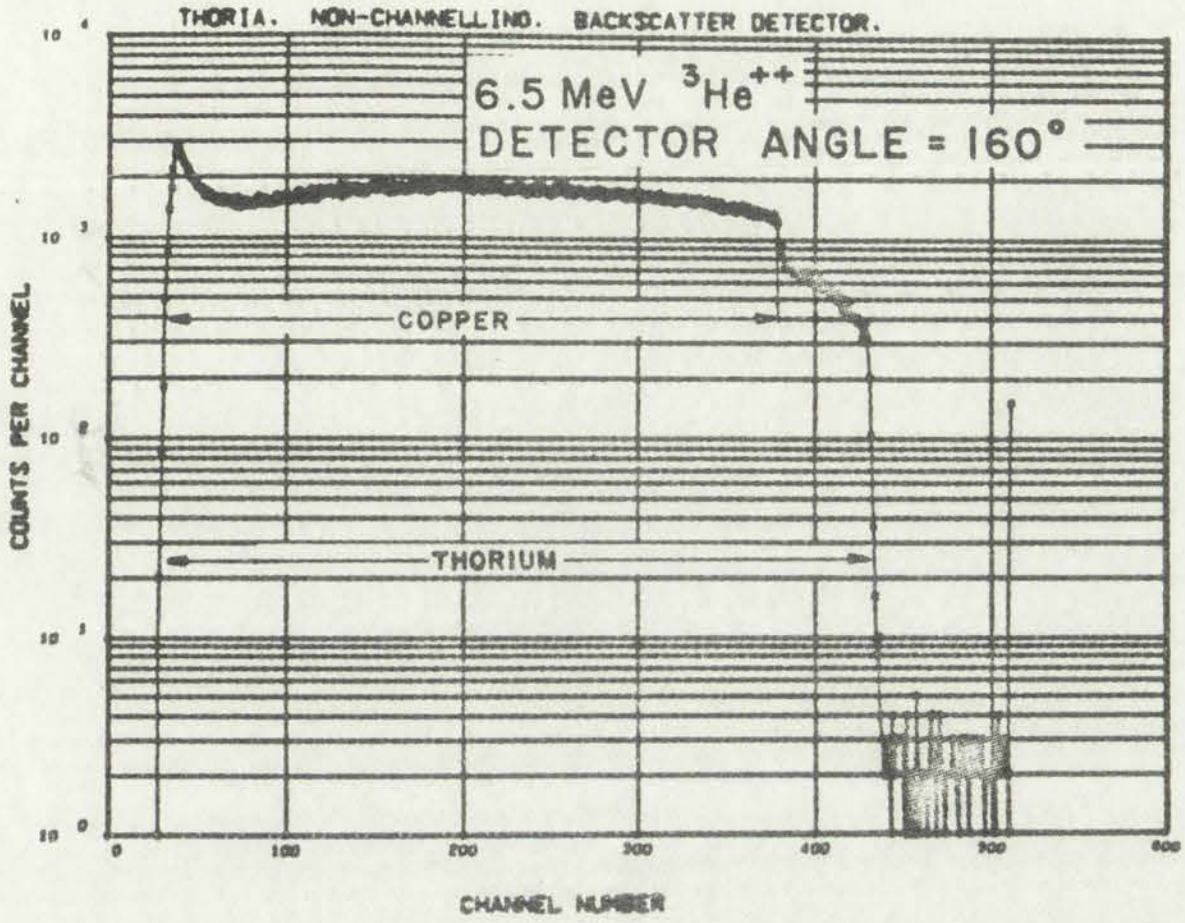

Fig. 40. Pulse-height distributions from ^{3}He particles backscattered by copper and oriented single-crystal thoria.

spectra, while the backscatter from the heavier thorium atoms extends to higher energies. The threshold of the counter that was used to record the backscatter data, from which the channeling orientation was determined, was adjusted so that only backscatters from the thorium atoms were counted. For the data presented in Fig. 40, the maximum backscatter energy from the copper atoms corresponds to channel 380, while the backscatter from the heavier thorium atoms extends up to about channel 430.

The backscatter data that were obtained as the upper arc of the goniometer was rotated across the ⟨111⟩ axis are shown in Fig. 41. The critical angle for channeling along the ⟨111⟩ axis of thoria is about 0.3° for 6.5 MeV ^{3}He particles. The location of the axis of rotation relative to the {110} planes of the crystal was not determined.

The critical angle is defined as the half-width at a level halfway between the normal and minimum yields. Usually only those encounters that take place near the surface are considered, so that complicating multiple scattering effects can be ignored. The critical angle for channeling is related to the crystal and particle parameters (Refs. 32 and 16).

$$\psi_{crit} \propto \left(\frac{Z_1 Z_2}{d \cdot E}\right)^{\frac{1}{2}} ,$$

where

Z_1 is the atomic number of the incident particle,

Z_2 is the average atomic number of the lattice atoms,

E is the particle energy, and

d is the lattice spacing.

The critical angle is also a function of the sample temperature.

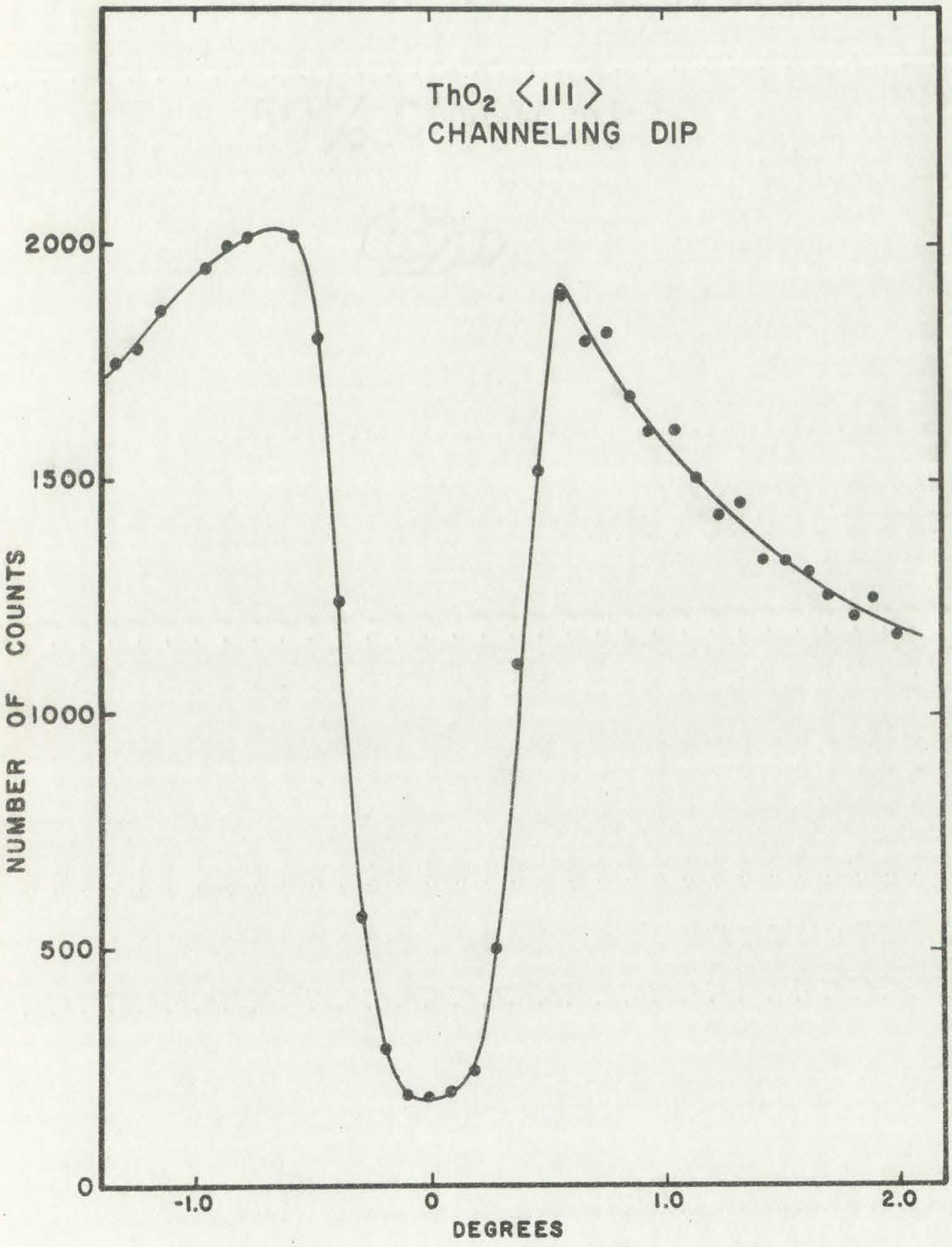

Fig. 41. Channeling dip for the ⟨111⟩ axis of thoria from backscatter techniques.

The dependence of the critical angle on the lattice spacing is not well understood. Picraux et al. (Ref. 16) have obtained experimental agreement with the theoretical dependence of Ψ_{crit} on the planar spacing only after correcting for the effects of surface transmission and surface oxide layers. They found that their theoretical predictions were consistently 20 to 25% larger than their experimental measurements.

The background that were present in these experiments are shown in Fig. 42. The upper plot shows the pulse-height distribution from the ^{3}He backscattered from the copper mask. The small background that is present in the region used to measure the thorium backscatter is from protons from carbon deposited on the mask by the beam. The background spectrum for the proton detector system is shown in the bottom plot. The absorber foil thickness was 60.96 μ aluminum.

The pulse-height distributions from the proton detector system are shown in Fig. 43 for three different crystal orientations. The top plot shows the distribution with the crystal oriented approximately 2° from the ⟨111⟩ channeling orientation. The spectrum is similar to that which might be obtained from a thick sample of amorphous oxygen.

The middle plot (Fig. 43) shows the proton spectrum that was obtained with the sample oriented in the ⟨111⟩ direction. The lower count rate is from channeling of the ^{3}He particles between the rows of nuclei. These data show the effect that is expected for activation analyses for substitutional-type impurities in a crystalline matrix. For certain interstitial sites and crystal orientations, the count rate will also decrease. However, since these interstitial impurities are between two lattice planes, orientations which enhance their activation can be found.

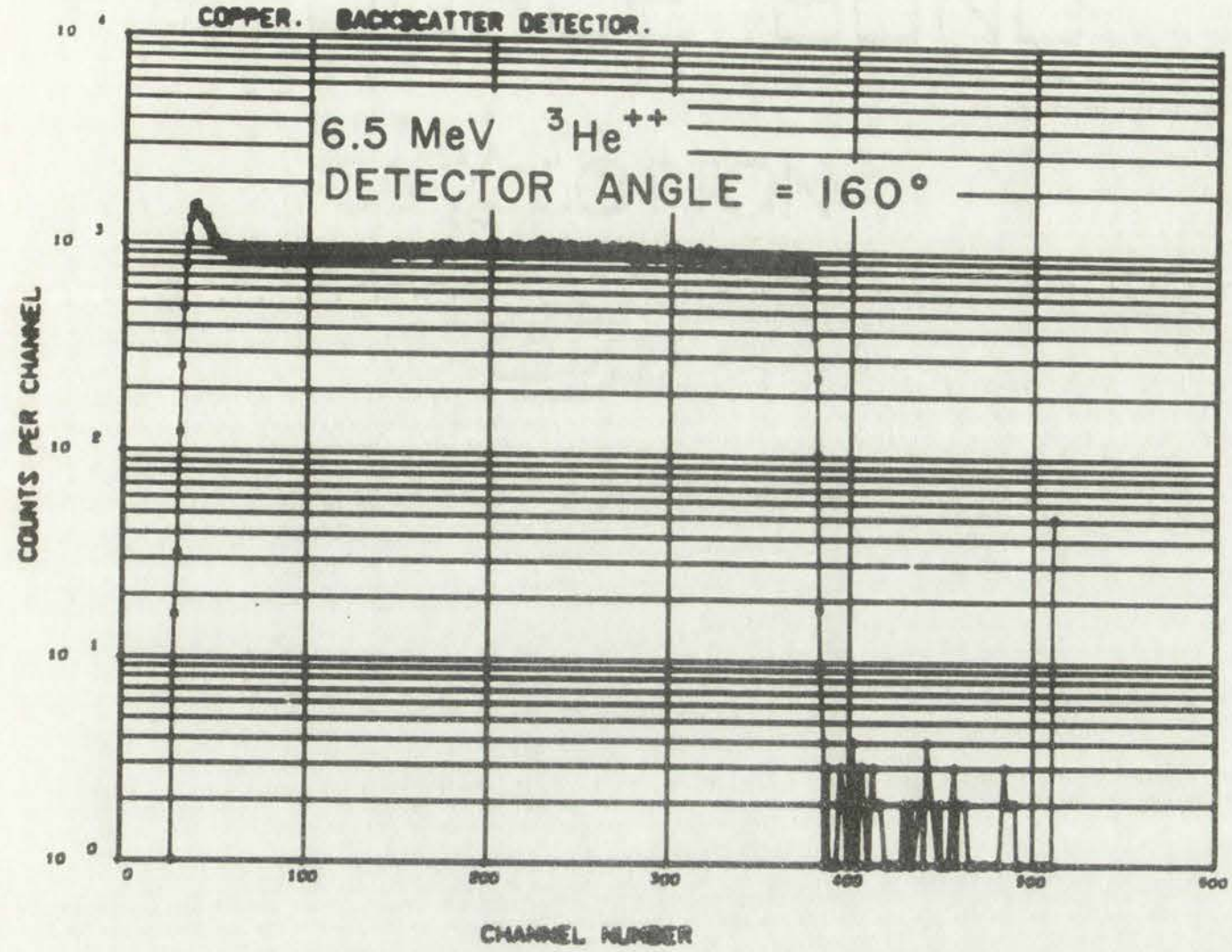

Fig. 42. Background pulse-height distributions from the copper mask.

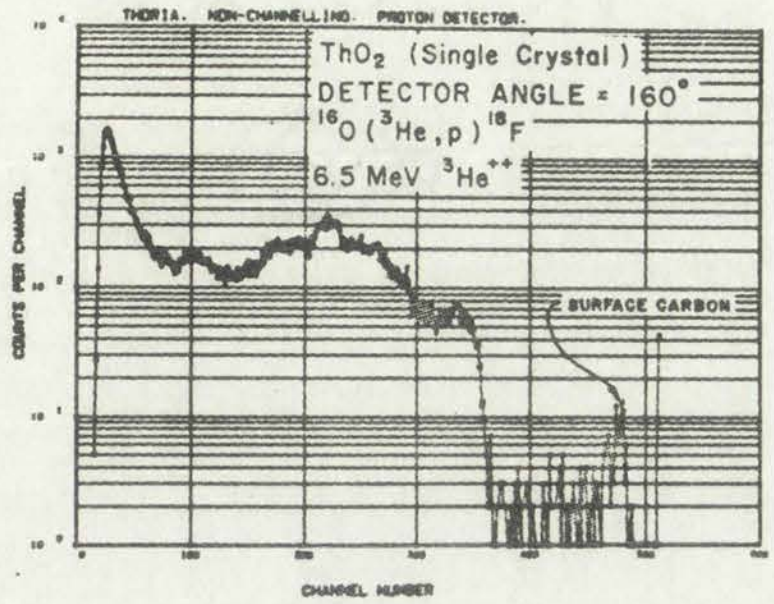

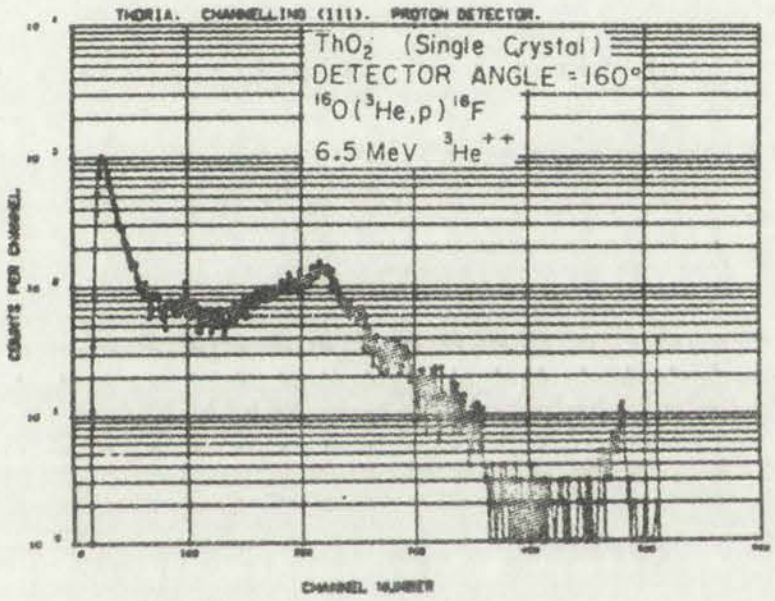

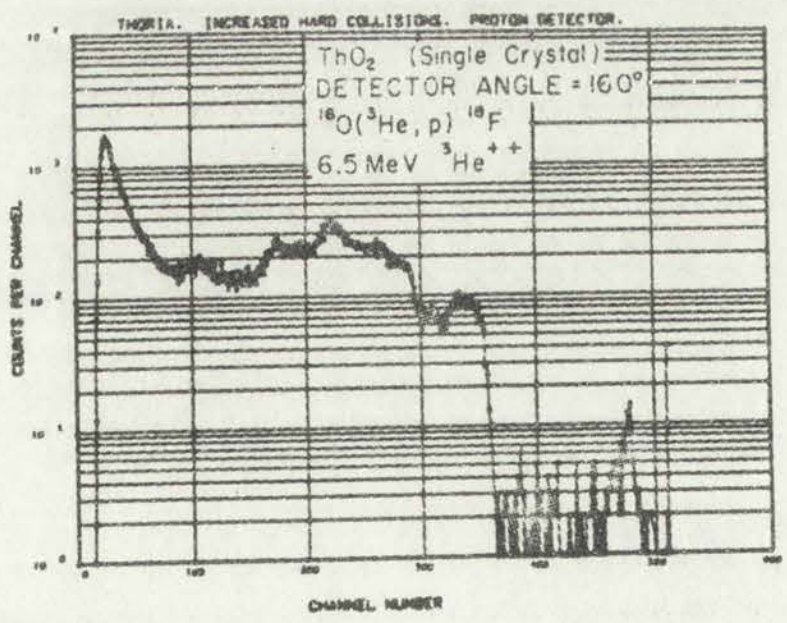

Fig. 43. Pulse-height distributions from oriented single-crystal thoria.

The pulse-height distribution that is obtained between the channeling and nonchanneling orientations is shown in the bottom plot (Fig. 43). The crystal was oriented 0.75° from the ⟨111⟩ axis for this irradiation. ^{3}He ions incident at this angle are steered close to the rows of nuclei, causing an increased number of hard collisions.

CHAPTER VI

RESULTS

Introduction

Analytical techniques were developed that utilized the thin target cross sections discussed in Chapter IV to unfold the complex proton spectra from the (^{3}He,p) reactions. Channeling and nonchanneling irradiations were performed on thick carbon and oxygen samples for calibration purposes and proof of the technique. Upper limits for the concentrations of carbon and oxygen were determined for tantalum and germanium samples.

Thick Target Calculations

One of the objectives of this experiment was to develop analytical techniques so that the complex proton spectra from the active ^{3}He activation analyses could be unfolded. The advantages of having a technique that would unfold the proton spectra for any bombarding energy or matrix material made it important that these be included as part of the analytical techniques.

The thick targets were considered to contain only two important impurity atoms for producing (^{3}He,p) reactions. These were carbon and oxygen. The samples analyzed were considered to contain impurity distributions of three different types:

1) A thin surface layer of carbon or oxygen that gives a response similar to that received from a thin target. There was a thin carbon layer on the samples analyzed from the carbon deposited by the beam. Thin oxide layers were present on the germanium and tantalum sample from surface oxidation.

2) An exponentially decreasing concentration from directly below the surface layer into the matrix material.

3) A constant volumetric concentration of the carbon and oxygen impurities.

These assumptions on the distributions of the impurities in the sample give us the capability of analyzing proton spectra from both thick and thin samples, in addition to samples with surface layers and surface gradients. Based on physical intuition, these are the types of distributions that are to be expected.

The following equation was used to unfold the pulse-height distributions that were obtained from the proton detector.

$$C = \Phi\Omega \sum_{j=1}^{m} N_j \sum_{i=1}^{n} \sigma_{i,j} \left(\frac{dx}{dE}\right)_{i,j}$$

where

Φ is the total number of incident ^{3}He particles,

Ω is the solid angle of the proton detector system,

m is the number of reactions that contribute to the experimental spectrum,

N_j is the concentration of the jth impurity atom (atoms/b-cm) in the sample interval dx,

n is the number of nuclear states associated with the jth reaction,

$\sigma_{i,j}$ is the differential cross section (b) for protons from the ith state and the jth reaction,

x is the distance (cm) that the ^{3}He particles have penetrated the sample,[1]

E is the proton energy (keV) at the detector for protons from the ith state and the jth reaction,[1] and

C is the number of counts in each channel (counts/keV).

The energy resolution of the proton spectrum is degraded primarily from the energy straggling of the protons as they lose energy in the target and absorber foil and also from the energy straggling of the ^{3}He particles as they are slowed in the target. Other lesser effects are from the angular resolution, from the resolution of the proton detector system, and from the energy spread in the incident ^{3}He beam. An empirical function with a Gaussian shape was used as the calculated resolution function. The width of the resolution function was dependent on the proton spectrum, the initial energy of the proton, and the proton energy at the detector.

$$D(E) = \frac{e^{-\frac{1}{2}(E-E_c)^2/\Delta E^2}}{2\pi \cdot \sqrt{\Delta E}} ,$$

where

D(E) is the distribution of the spread data,

ΔE (standard deviation of the Gaussian) where

$$\Delta E = \left\{P(1) \cdot E_c^2/E_R + P(2)\right\}^{\frac{1}{2}}$$

---

[1]From the incident ^{3}He energy, reaction kinematics and the energy loss data for the target and for the absorber foil, the functions $x = f(E_{i,j})$ were calculated. These functions were interpolated using cubic splines and the first derivatives $(dx/dE)_{i,j}$ were determined from these interpolated functions.

P(1) and P(2) are parameters for which the best least-squares values can be obtained,

E_R is the proton energy at the reaction, and

E_c is the calculated proton energy at the detector.

The 17 parameters that may be least-squares fitted to the experimental proton spectral data are listed in Table 5. In general, several of these parameters were usually fixed for a given analysis.

The computer code that was used for this least-squares analysis has not been optimized for the most efficient and fastest convergence. The running time varies greatly depending on the number of free parameters, the ^{3}He energy, and whether both carbon and oxygen concentrations are being calculated. For the most complex case, the running time would be approximately 10 min on a CDC 7600 computer. The program uses approximately $(200,000)_8$ core locations.

This code has been designated IMP for IMPurity calculation code.

Thin Oxygen Calibration Data

Figure 44 shows the proton spectrum from the oxygen calibration run that was unfolded using the IMP code. The results from this analysis compared quite favorably with those that were obtained using the C24HE3P unfolding code discussed in Appendix D. The thickness calculated by the IMP code was 54 $\mu g/cm^2$ compared to 48 $\mu g/cm^2$ previously calculated using comparable cross sections. This small difference could be due to several things, a slightly different resolution function, a more accurate calculation of the ^{3}He energy in the thin layer, or a slight error in the dE/dx data that were used.

TABLE 5

PARAMETERS FOR LEAST-SQUARES ANALYSIS

P(1) is the slope of the resolution function.

P(2) is the zero intercept of the resolution function.

P(3) is the slope of the system gain (keV/channel).

P(4) is the energy corresponding to channel zero.

P(5) is the detector angle (°).

P(6) is the thickness of the absorber foil (cm).

P(7) is the energy of the incident ^{3}He particles (keV).

P(8) is the atom density of the carbon surface layer (atoms/b-cm). The (dE/dx) values used for the surface layers are those of the matrix material. The atom densities in the surface layers are adjusted to correspond to the density of the matrix material.

P(9) is the thickness of the carbon surface layer (cm).

P(10) is the amplitude of the carbon concentration beneath the carbon surface layer from the exponential gradient (atoms/b-cm).

P(11) is the slope of the above exponential gradient (atoms/cm).

P(12) is the body concentration of carbon atoms (atoms/b-cm).

P(13) through P(17) are the oxygen parameters and correspond to P(8) through P(12) defined for carbon above.

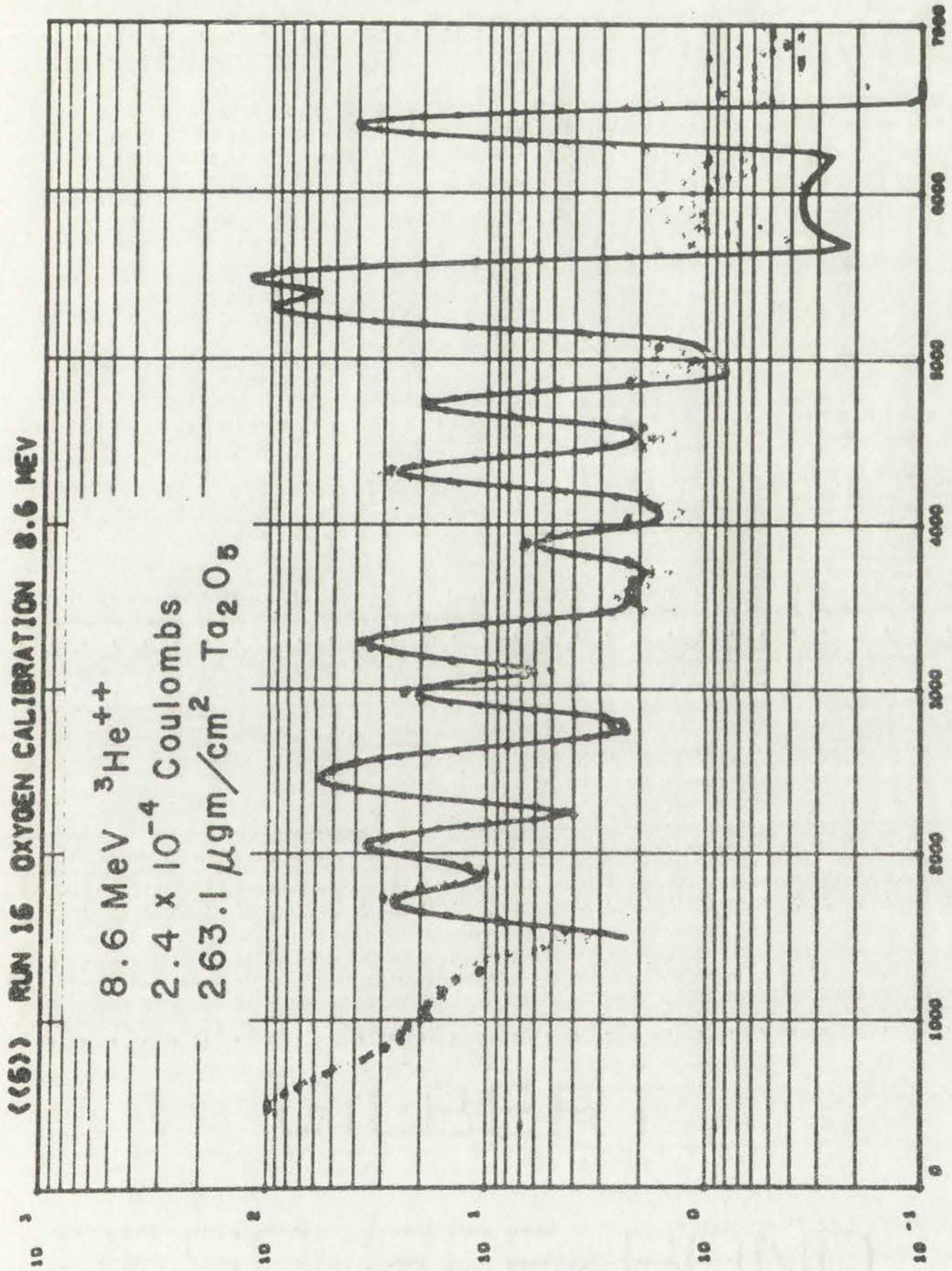

Fig. 44. Analysis of prompt proton spectrum from a thin oxygen sample using the IMP code.

Thick Carbon and Oxygen Samples

Thick carbon and oxygen samples were irradiated with ^{3}He particles, and the proton spectra were recorded ataa detector angle of 160°. Aluminum absorber foils with a total thickness from 60 to 100 μ were used. Data were obtained at ^{3}He energies of 4.4, 5.175, 6.0, 6.5, 6.8, and 8.6 MeV. The results of these irradiations indicated that the oxygen and carbon cross sections that were calculated from the thin target irradiations at 8.6 MeV and the $^{12}C(^{3}He,\alpha)^{11}C$ and the $^{16}O(^{3}He,p)^{18}F$ cross sections from Refs. 2 and 18 were slightly inconsistent. The thick carbon data indicated that the $^{12}C(^{3}He,p)^{14}N$ cross sections were about 15% high and that the $^{16}O(^{3}He,p)^{18}F$ cross sections were about 40% too small. The cross-section data presented in Chapter IV have been corrected to correspond to these thick target irradiations. These differences are quite possibly due to the smoothing effect of the stacked foil technique on the resonance peaks that are present in the cross sections.

Figure 45 shows the analyzed proton spectrum from the irradiation of a thick carbon sample at 5.175 MeV ^{3}He energy. The analyzed data from a thick oxygen irradiation at 6.8 MeV ^{3}He energy are shown in Fig. 46. The small portion of data between 3.3 and 4.1 MeV that is not analyzed (these limits depend on the thickness of the absorber foil) is due to the lack of cross-section data for the $^{12}C(^{3}He,p)^{14}N$ ground-state reaction below a ^{3}He energy of 2.8 MeV. All spectra analyzed for carbon will contain this discontinuity.

To determine if differences in the current integration from the thick carbon and from the thick oxygen samples or absorbed water in the Ta_2O_5 sample could have caused the deviations that were measured in these cross

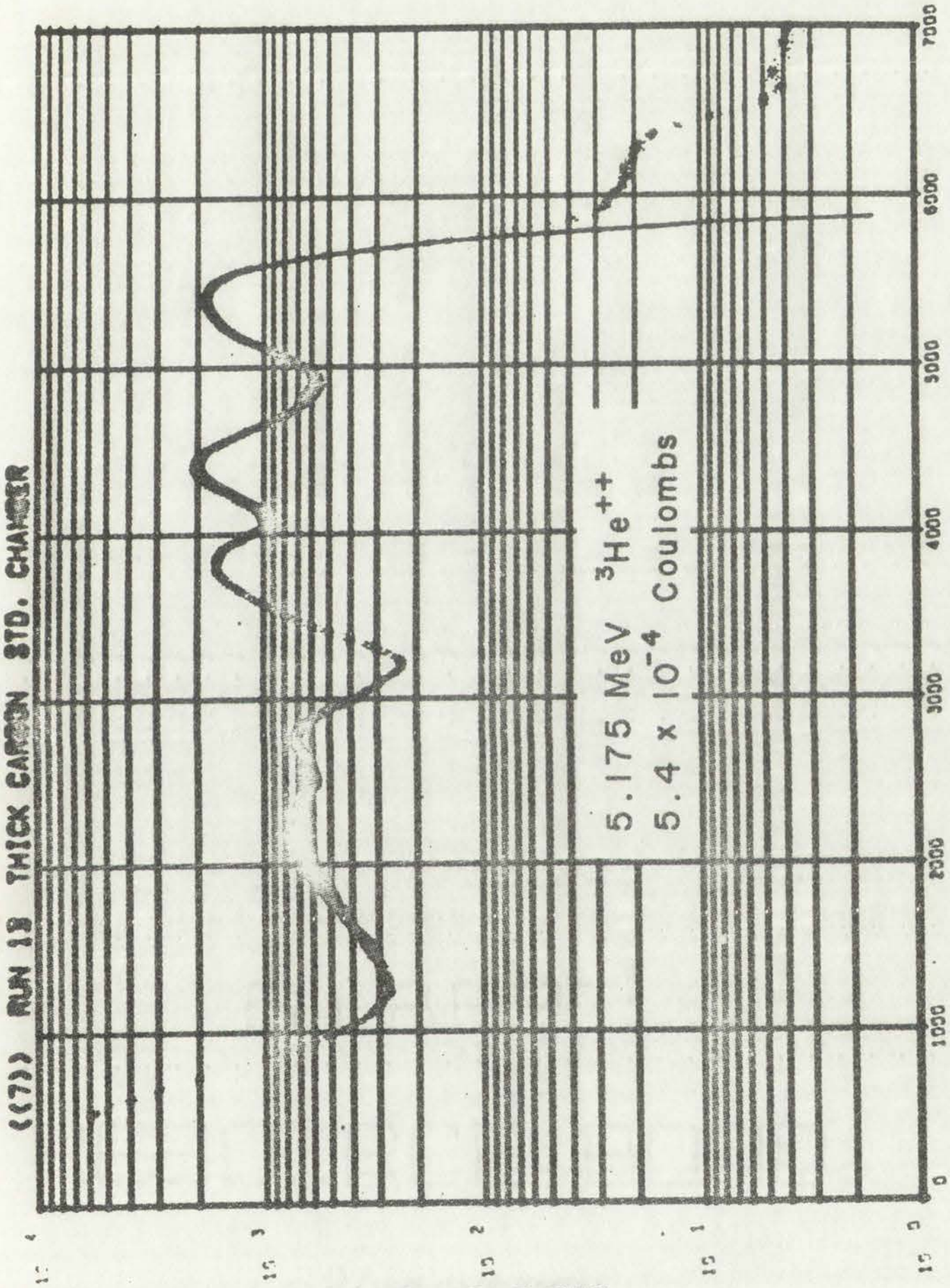

Fig. 45. Analysis of prompt proton spectrum from a thick carbon sample using the IMP code.

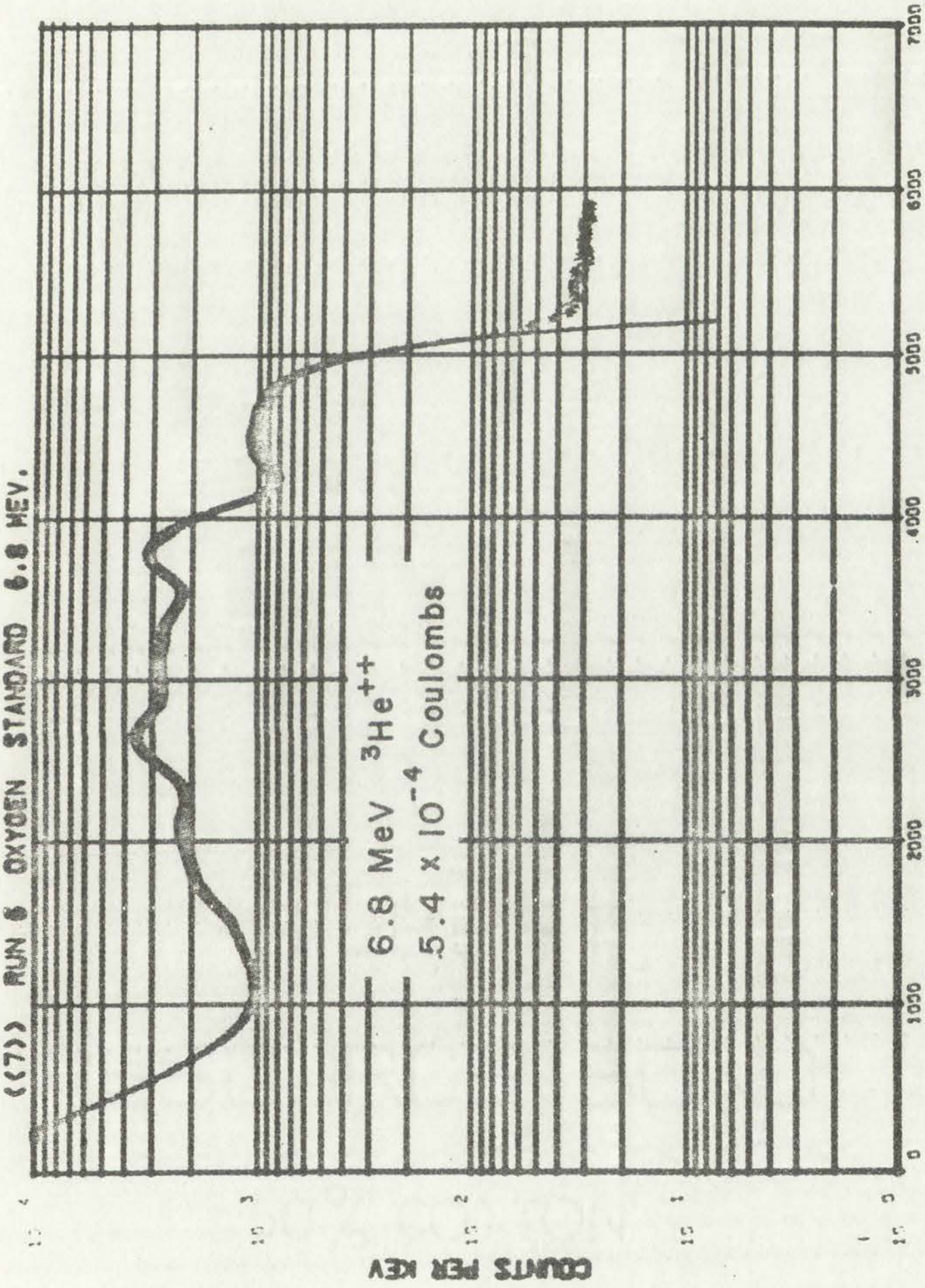

Fig. 46. Analysis of prompt proton spectrum from a thick oxygen sample using the IMP code.

sections, a calcite ($CaCO_3$) sample[1] was irradiated and the C:O ratio was calculated. The calculated C:O ratio using the revised cross-section data was approximately 3.0. This compares favorably with the theoretical ratio. The analyzed calcite spectrum is shown in Fig. 47.

Activation Analysis of Tantalum

Etched tantalum samples were irradiated at 5.175 and 8.6 MeV ^3He energies. These samples were analyzed for surface carbon, body carbon, surface oxygen, and body oxygen concentrations. The results of these analyses are given in Table 6. A typical analysis of a proton spectrum

TABLE 6

CARBON AND OXYGEN CONCENTRATIONS IN TANTALUM

Sample	^3He Energy (MeV)	Surface Carbon ($\mu g/cm^2$)	Body Carbon (ppm)	Surface Oxygen ($\mu g/cm^2$)	Body Oxygen (ppm)
3	5.175	0.65	103	0.27	79
513	5.175	0.36	79	0.34	80
512	8.6	0.35	41	0.49	77
510	8.6	0.34	58	0.65	96

from a tantalum irradiation is shown in Fig. 48. The amount of surface carbon measured is from carbon deposited on the sample during the irradiation. Therefore, the values obtained for the surface carbon concentrations are greatly dependent on the quality of the vacuum in the target chamber and are not related to the sample. The amount of surface oxygen depends on the sample preparation and the length of time that the sample

---

[1]A freshly cleaved sample from a crystal collected by Dr. Elva H. Clinard in the vicinity of the Harding Mine in New Mexico.

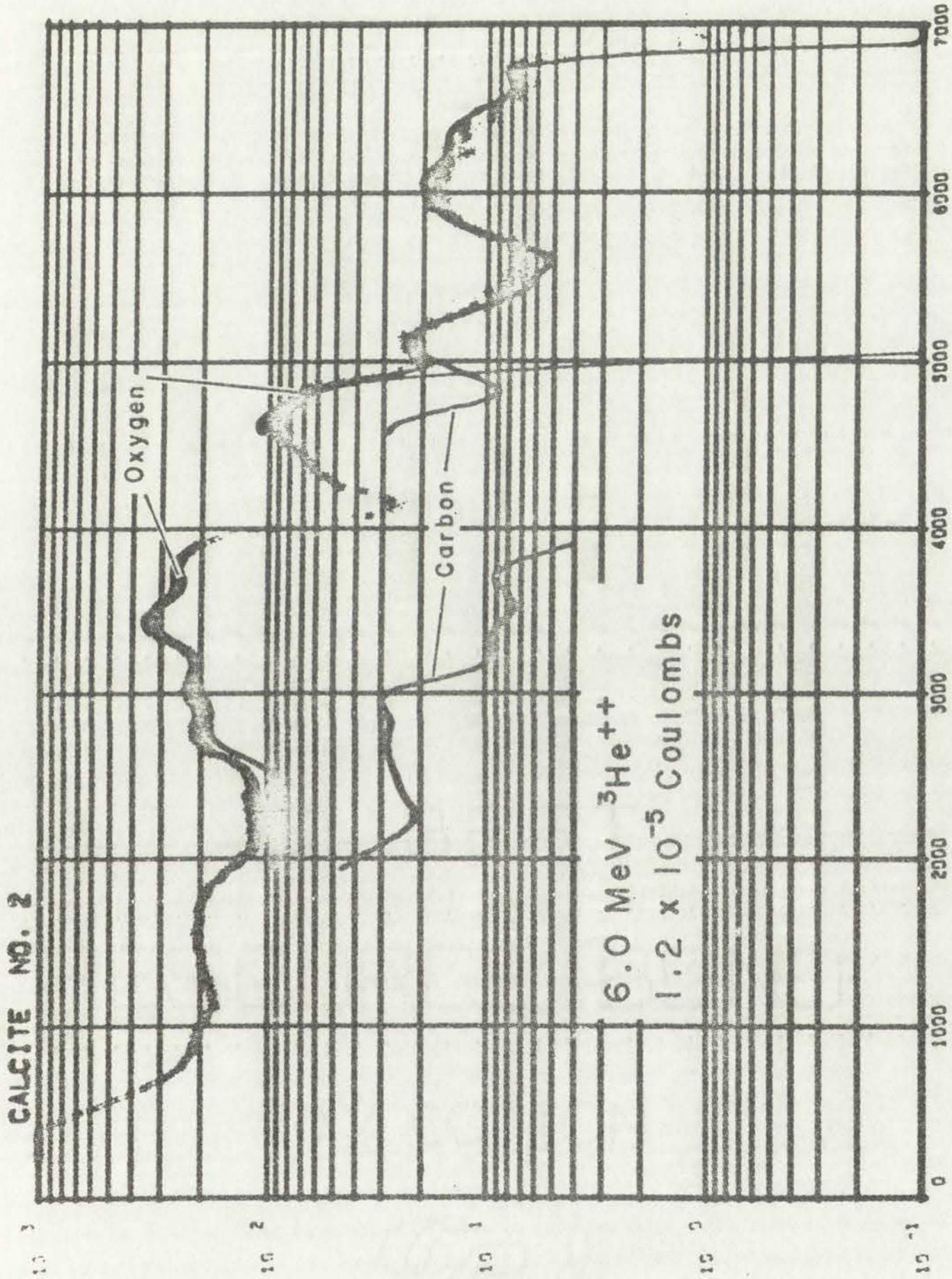

Fig. 47. Unfolded prompt proton spectrum from a ^{3}He irradiated calcite sample.

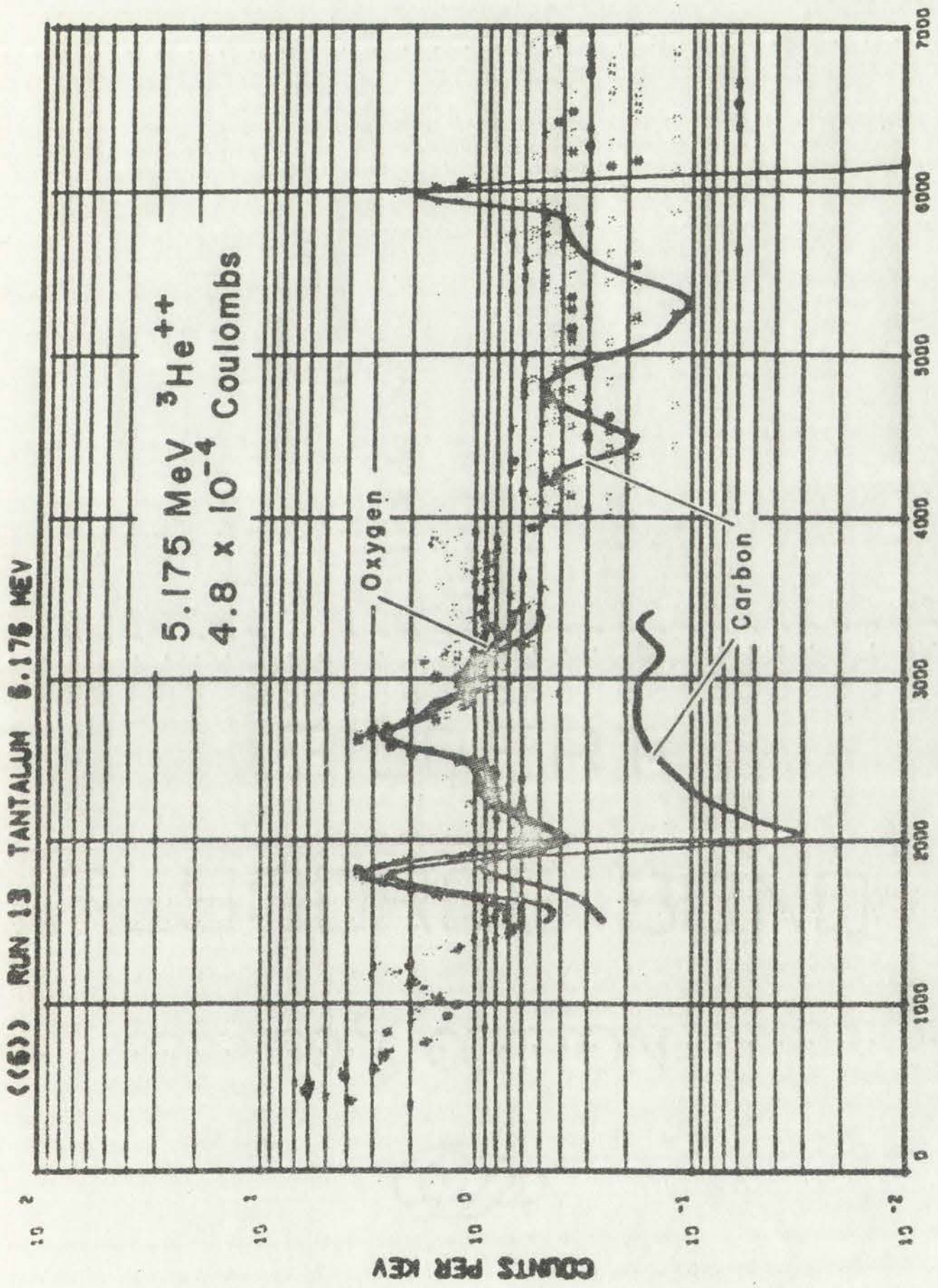

Fig. 48. Unfolded prompt proton spectrum from a tantalum activation sample.

surface was allowed to oxidize between sample preparation and irradiation. Therefore, a large variation in these surface concentrations could be expected since neither of the above variables was controlled.

The variations in the calculated values for the body oxygen concentrations are well within those expected from statistical fluctuations in the unfolding and fluctuations in the sampling process. The variations in the calculated values for the body carbon are fairly large. This might be attributed to the sampling process or the existence of an interference reaction.

Since interferences were not considered in the unfolding of the spectral data, the results listed in Table 6 and all later results should be interpreted as upper limits of the impurity concentrations.

Channeling Irradiations

Qualitative information on the locations of the impurities in crystalline matrixes can be easily obtained by channeling the ^{3}He particles along various crystal axes. Channeling irradiations were performed on single-crystal thoria and single-crystal germanium samples.

The channeling in single-crystal thoria is unique because both the oxygen and thorium atoms produce independent events which may be recorded. Backscatter from the high-atomic-weight thorium atoms and $^{16}O(^{3}He,p)^{18}F$ reactions can be used to measure independently the channeling characteristics of the thoria.

Typical backscatter and proton spectra were shown in Chapter V for channeling and nonchanneling crystal orientations along the $\langle 111 \rangle$ axis. Further channeling studies were performed along this axis and also along the $\langle 110 \rangle$ axis. The ratio of the channeling to nonchanneling spectral data are shown in Figs. 49 through 52. Thoria is a face-centered cubic

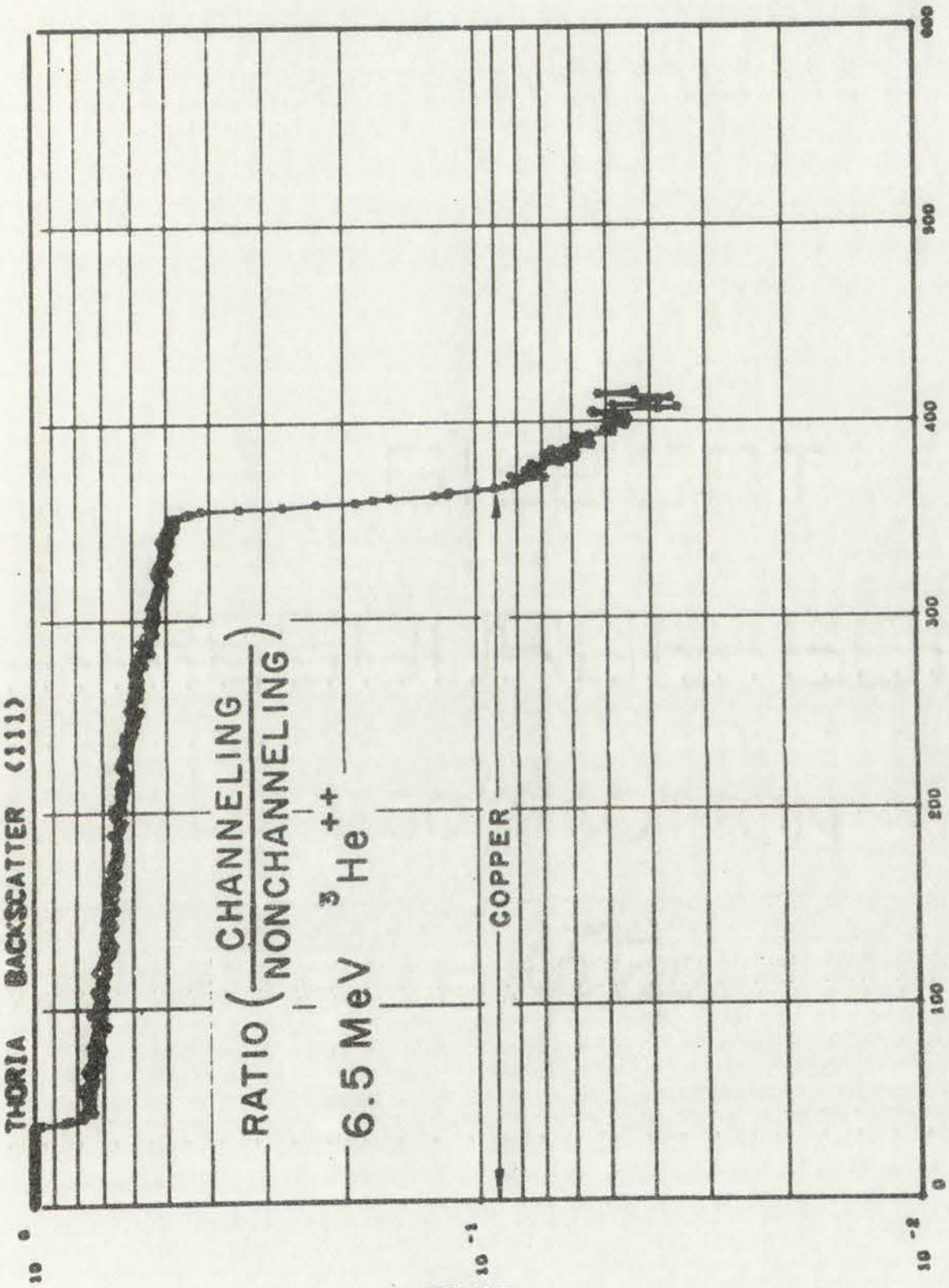

Fig. 49. Ratio of channeling to nonchanneling ^{3}He backscatter pulse-height distributions from irradiations along the $\langle 111 \rangle$ axis of single-crystal thoria.

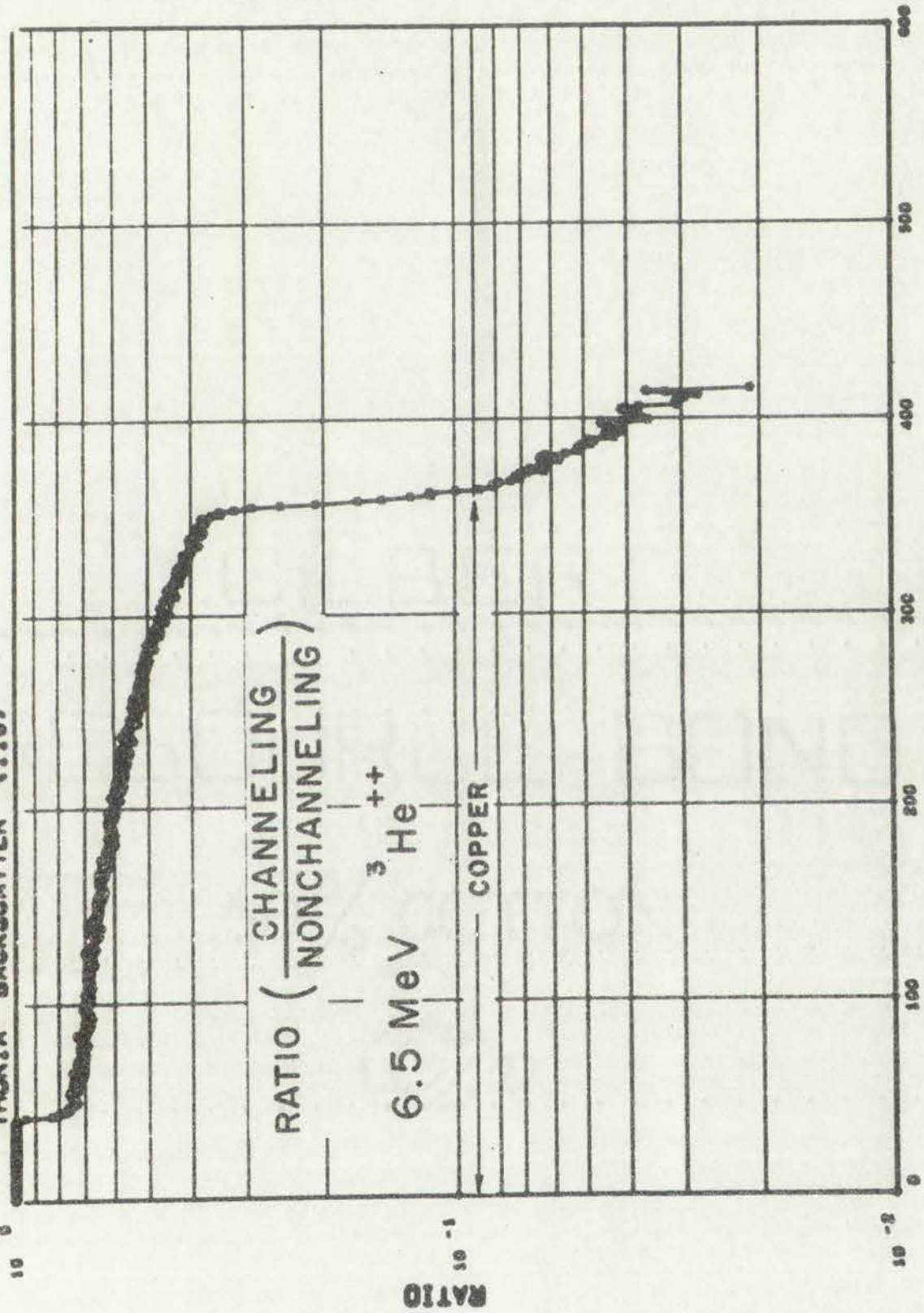

Fig. 50. Ratio of channeling to nonchanneling ^{3}He backscatter pulse-height distributions from irradiations along the ⟨110⟩ axis of single-crystal thoria.

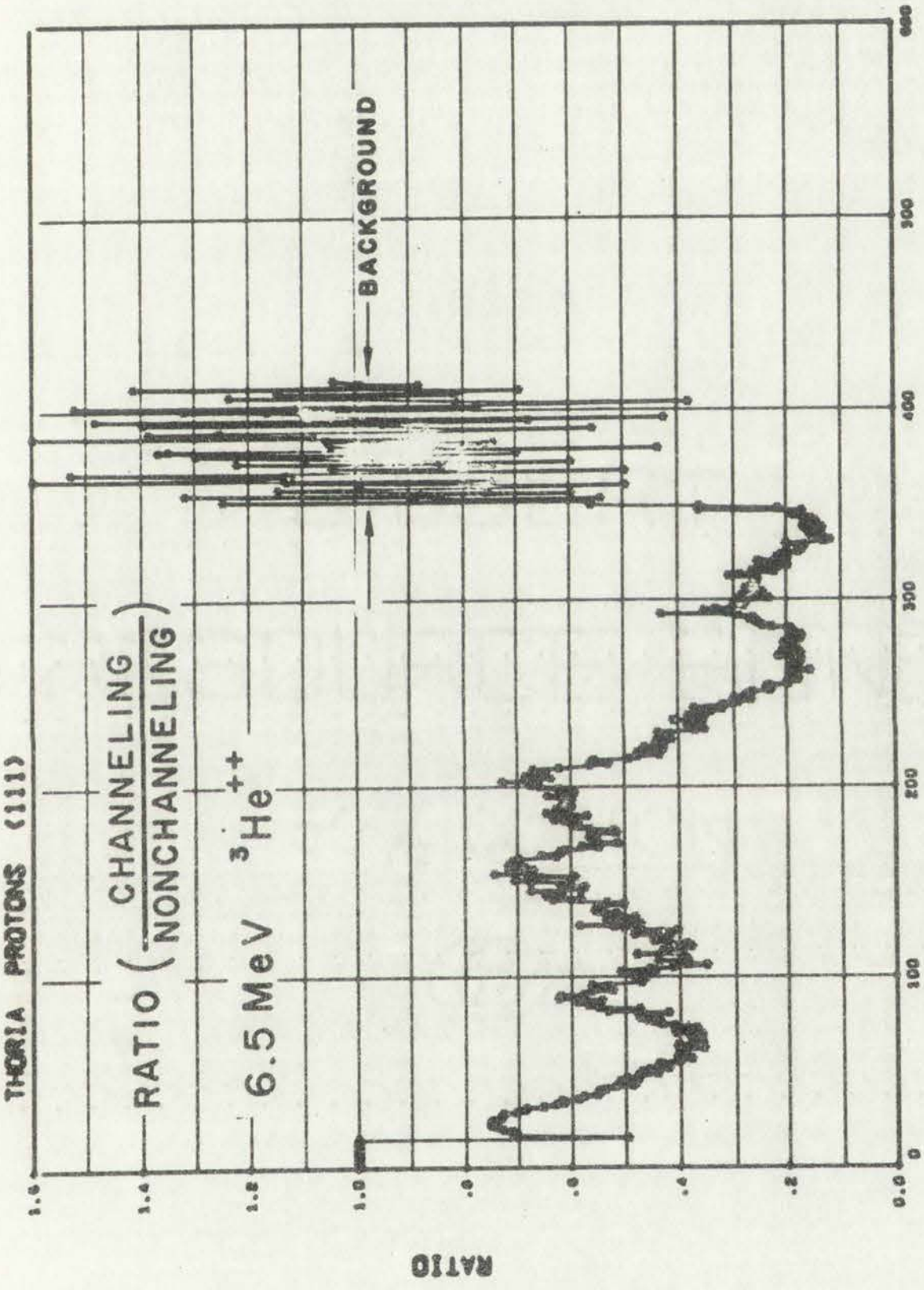

Fig. 51. Ratio of channeling to nonchanneling prompt proton pulse-height distributions from irradiations along the ⟨111⟩ axis of single-crystal thoria.

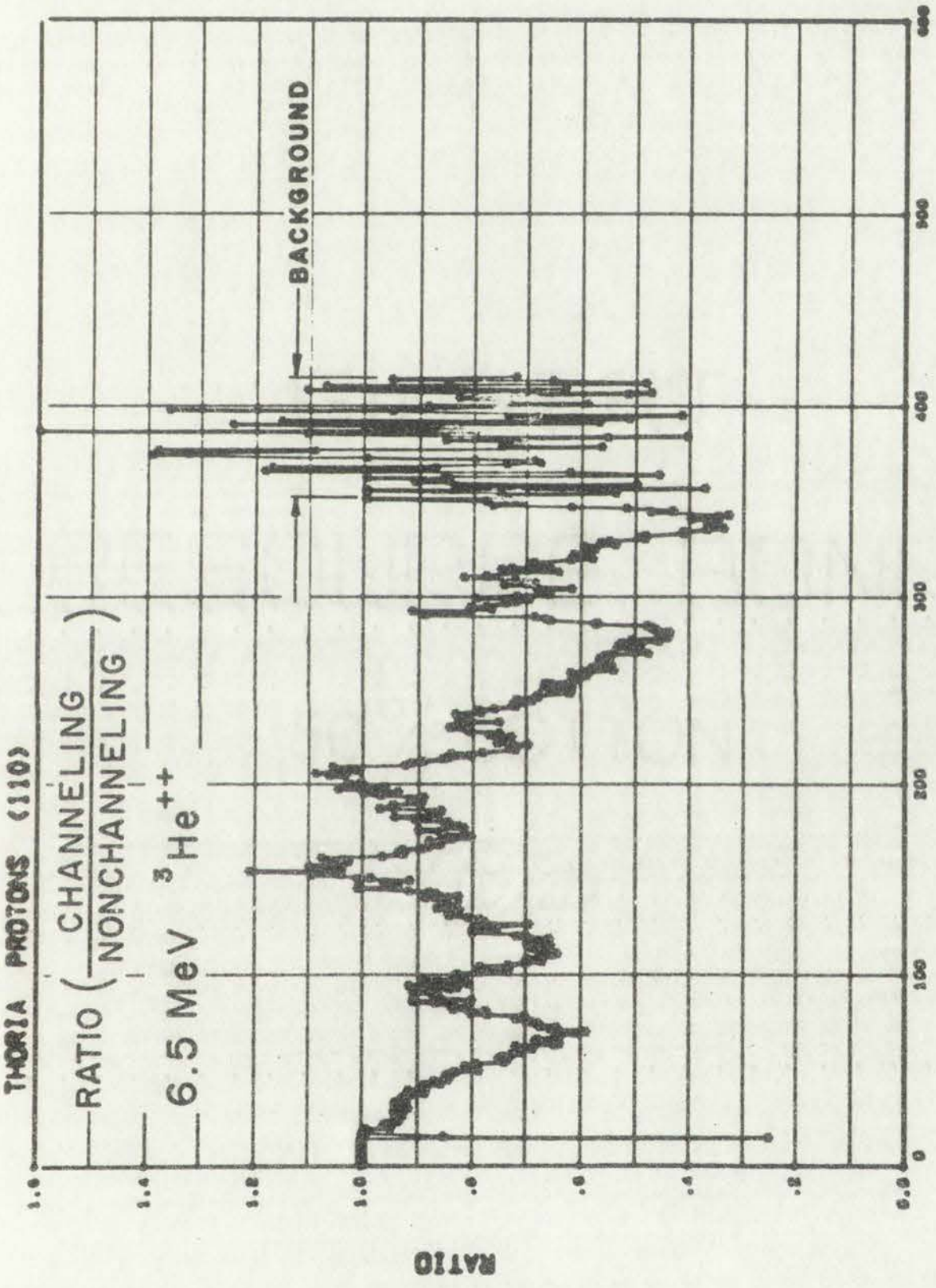

Fig. 52. Ratio of channeling to nonchanneling prompt proton pulse-height distributions from irradiations along the ⟨110⟩ axis of single-crystal thoria.

structured crystal. The irradiations along the ⟨111⟩ axis should not preferentially scatter from and activate interstitial impurities in the large (½,½,½) interstitial sites. However, channeling irradiations along the ⟨110⟩ axis should cause preferential activation of displaced oxygen atoms or impurity atoms located in these sites. Likewise, if the thorium atoms are displaced into these sites, increased backscatter should be measured relative to the increase in the number of counts in the proton spectrum from the oxygen atoms.

The ratio of the counts in the channeling backscatter spectrum to the counts in the nonchanneling backscatter spectrum that were obtained for the ⟨111⟩ channeling orientation is shown in Fig. 49. The corresponding ratio of data obtained for the ⟨110⟩ axis is shown in Fig. 50. These data are quite similar but with slightly better channeling along the ⟨111⟩ axis.

The corresponding ratio of the proton spectral data is shown in Figs. 51 and 52. Figure 51 is from data that were obtained near the ⟨111⟩ axis, and Fig. 52 is from data that were obtained near the ⟨110⟩ axis. There is a significant difference in these data. These proton data indicate much better channeling along the ⟨111⟩ than along the ⟨110⟩ axis. This is interpreted to indicate that the number of oxygen activations is increased because of displaced oxygen atoms in the (½,½,½) sites which are unshielded and parallel with the ⟨110⟩ axis.

Channeling and nonchanneling irradiations were performed on single-crystal germanium to attempt to measure and locate the oxygen and carbon impurity atoms. Figures 53 and 54 show the analyzed proton spectrum from the channeling and nonchanneling irradiations, respectively. The

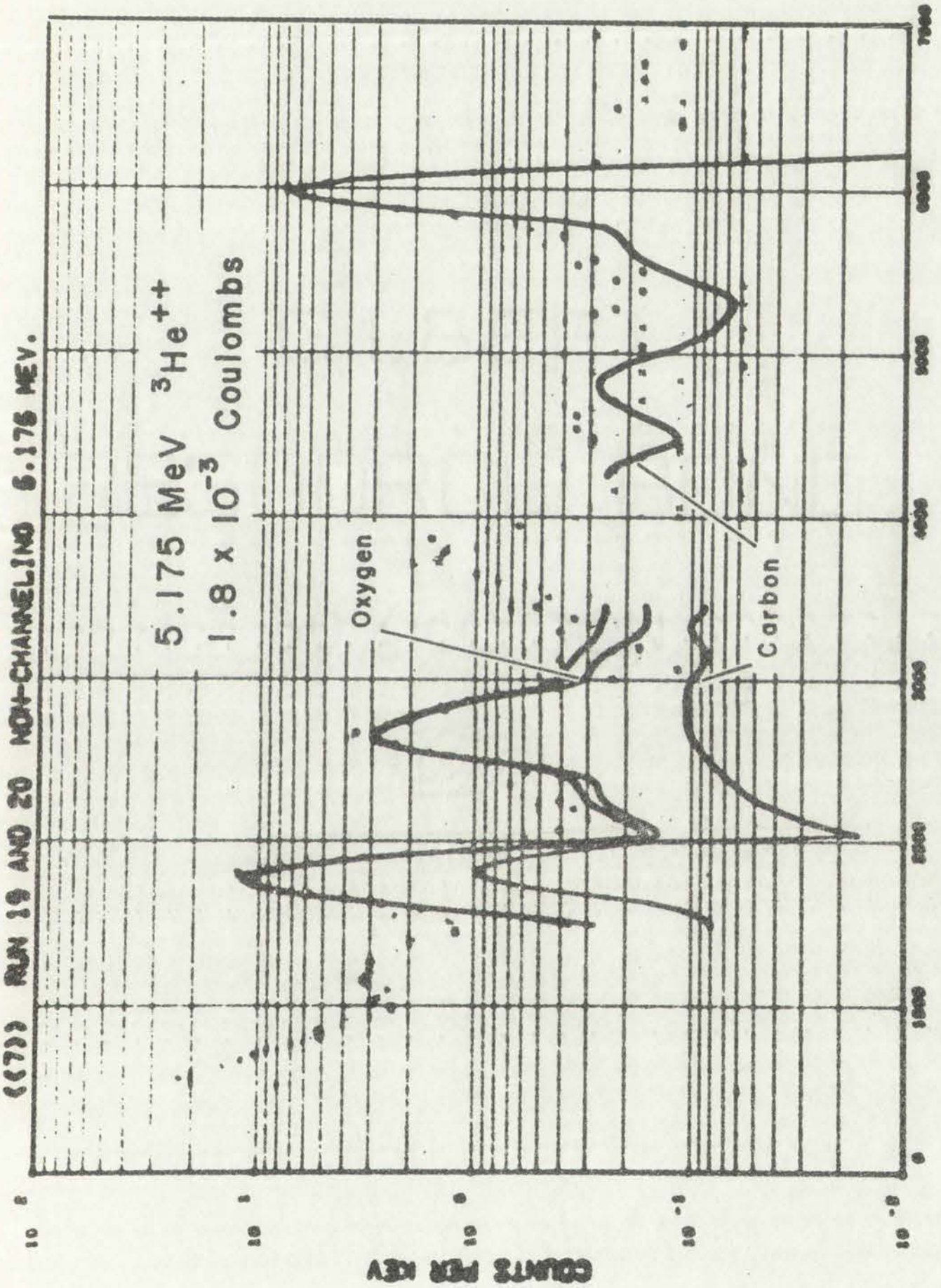

Fig. 53. Unfolded prompt proton spectrum from the nonchanneling irradiations of single-crystal germanium.

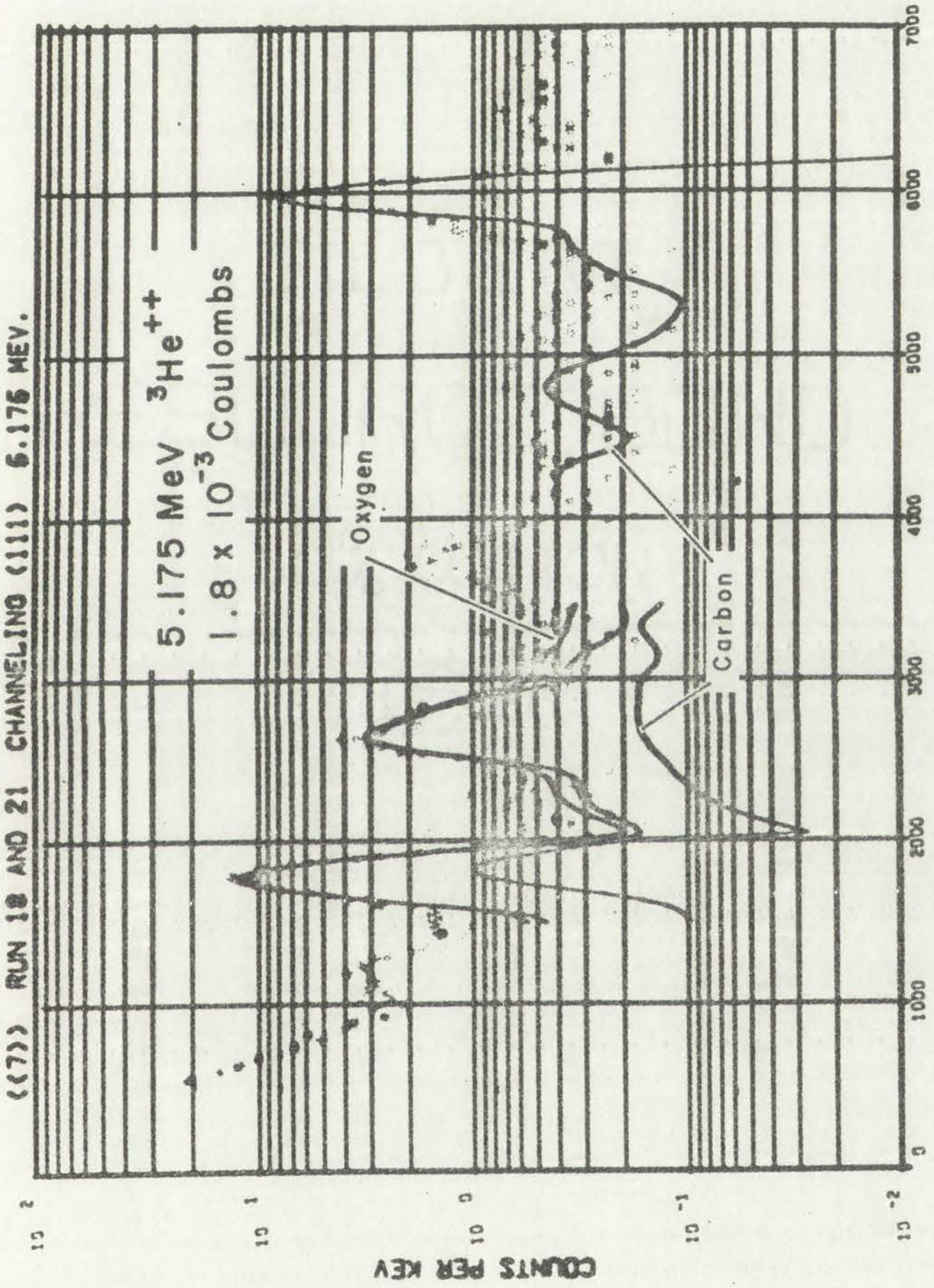

Fig. 54. Unfolded prompt proton spectrum from the channeling irradiation of single-crystal germanium along the ⟨111⟩ axis.

results from these analyses are listed in Table 7. These irradiations were performed at 5.175 MeV ^{3}He energy.

TABLE 7

GERMANIUM ACTIVATIONS

Sample Irradiation Number	Surface Carbon ($\mu g/cm^2$)	Body Carbon (ppm)	Surface Oxygen ($\mu g/cm^2$)	Body Oxygen (ppm)	Total Charge (C)
7-1920 nonchanneling	0.37	14	0.11	7.7	1.8×10^{-3}
7-1821 channeling $\langle 111 \rangle$	0.35	22	0.11	9.2	1.8×10^{-3}
3-223 nonchanneling	0.33	20	0.08	13.4	3.0×10^{-4}

The surface carbon is from carbon that is deposited on the sample during the irradiation. The surface oxygen is from a thin oxide layer on the germanium. The slightly higher carbon and oxygen impurity concentrations measured in the channeling orientation (Sample 7-1821 and Sample 7-1920) indicate that both the carbon and the oxygen are mostly interstitial impurities. Sample irradiations 7-1821 and 7-1920 correspond to similar irradiations on the same sample, except for the channeling and nonchanneling parameters. Sample irradiation 3-223 was performed on a different sample during a different accelerator shift.

Errors

The uncertainties associated with the data that are presented can only be estimated. The uncertainty in the cross-section data is estimated to be $\pm$15%. The primary sources of this uncertainty are the solid angle of the detector system, the stopping power of the matrix material and the resolution function used in the unfolding code.

It is estimated that the uncertainties in the surface and body concentrations due to the statistical fluctuation in the unfolding process is much less than that due to the sampling process itself. Insufficient data were obtained to calculate these uncertainties.

CHAPTER VII

CONCLUSIONS

High-energy reaction protons, due to the high Q value of the (^{3}He,p) reactions with oxygen and carbon, present a unique method of studying the surface and body concentrations of these isotopes in high-Z samples. This active method allows the determination of surface layer thicknesses in the 0.01 $\mu g/cm^2$ region and body concentrations in the 1.0 ppm region. There are low backgrounds associated with this type of measurement.

The thin sample cross sections that were determined and used in the unfolding code allow proton spectral data to be analyzed for various ^{3}He energies, matrix materials, and impurity distributions. The optimum ^{3}He energies for activation analysis for carbon and for oxygen in the presence of each other can be calculated using the techniques that are presented.

Channeling phenomena can be used to obtain qualitative information on the location of the oxygen and carbon impurities in crystalline matrixes. If the impurities are substitutional, the effective cross sections will be lowered for all channeling irradiations. If the impurities are interstitial, preferential activation of the impurities will be obtained for irradiations in some of the major channeling directions. Irradiations of single-crystal germanium indicated that the carbon and oxygen impurities were primarily interstitial.

Because of their large Q values, it appears that boron and/or nitrogen could produce a significant interference if they were present in the sample. Isotopes of both of these elements have (^{3}He,p) reactions with

quite large positive Q values. The (^{3}He,p) reactions involved are of no importance to normal passive analyses, since all of the reaction products are stable. The percent natural abundance and Q values for these reactions are listed in Table 8.

TABLE 8

POSSIBLE INTERFERENCE REACTIONS

Reaction	Abundance (%)	Q Value (MeV)
^{10}B(^{3}He,p)^{12}C	18.83	19.6945
^{11}B(^{3}He,p)^{13}C	81.17	13.1854
^{14}N(^{3}He,p)^{16}O	99.64	15.2426
^{15}N(^{3}He,p)^{17}O	0.36	8.5504

It should be possible to measure nitrogen impurities in addition to carbon and oxygen by using these techniques.

The phenomenon of carbon buildup on the targets during the irradiations was a problem. The buildup rate seemed to vary directly with the pressure in the vacuum system. Installation of additional liquid nitrogen cold traps and vacuum pumps near the target chambers lowered the carbon buildup rate to a tolerable background.

The carbon buildup on the sample surface was greatly reduced during the channeled germanium irradiations. It is suspected that the energy and kinetmatics of the carbon atoms that normally adhere on the surface are such that they channel deeper into the crystal before stopping and do not add to the carbon surface layer.

Sample temperature and radiation damage should be considered when doing channeling experiments. At higher sample temperatures, the increased thermal motion of the lattice will decrease the amount of channeling. Radiation damage to the lattice structure during the bombardment will also decrease the amount of channeling. To minimize the increase in sample temperature and also the radiation damage to the sample, low particle energies and currents were used in the irradiations.

The techniques and data that have been presented offer new and interesting ways to study carbon and oxygen impurity concentrations in materials.

APPENDIX A

DECAY CURVE ANALYSIS CODE

This code is written in FORTRAN IV for the CDC 6600 computer to unfold the complex decay curves that were obtained using the large 4π detector system.

Activation analyses with ^{3}He quite often result in reaction products that are neutron poor and decay by positron emission. Two reasonably long-lived reaction products from the bombardment of carbon and oxygen are ^{11}C and ^{18}F. Both of these decay by positron emission, and the complex decay curve obtained from counting the annihilation gamma rays must be unfolded into its components to determine how much carbon and how much oxygen were present in the sample. Special analyses and detector equipment can be used where there is a gamma ray coincident with the positron decay of an activation product (Ref. 40); however, this is not the case with ^{11}C and ^{18}F.

Shortly after the completion of an activation irradiation, the sample was placed in the 4π detector. Both coincident and singles spectra were recorded at 100-sec intervals using a 4096-channel ADC. The entire 4096 channels of data could be transferred to magnetic tape in 2.14 sec. At the tape densities used, slightly more than 1000 spectra could be recorded on a single tape. Data from these tapes were used as input to the DECURA code.

The function

$$Y(J) = P(1)*\sum_{I=1}^{NOI} P(I*2)*EXP(P(I*2+1)*X(J))$$

is least squares fitted to the data. The J subscript refers to the Jth data point, and the I subscript refers to the Ith exponential. Best least-squares values can be obtained for each of the parameters, P(I), in the equation. The parameters may be fixed (held constant at the input value) or free (allowed to vary until their best-least-squares value is obtained). Y(J) is the rate of decay (counts/sec), and X(J) is the elapsed time since the irradiation stopped (sec). No provision is made in the code to correct for decay during the counting interval. Therefore, the count interval should be much less than the mean life of the shortest half-lived isotope that is being counted. The code will fit a maximum of ten exponentials and 4096 data points.

The code is written to use data from a 4096-channel spectrum for each input data point. Various sections of each spectrum are summed and stored as the dependent variable after the data are corrected for dead time.

Least-squares techniques of Moore and Zeigler (Ref. 41) are used in the code.

Main Program DECURA

The main program calls the subroutines and sets up the fixed parameters for the first five iterations. If some of the exponential slopes are designated as being free, they will be fixed for the first five iterations, and only those amplitudes that are designated as being free are allowed to vary. Usually P(1) is fixed; however, if P(1) is free, the calculation starts at iteration five.

The more important variables used in the main program are listed in Table 9.

TABLE 9

MAIN PROGRAM DECURA VARIABLES

IM	number of fixed parameters
IPLTFL	input flag
IT	number of iterations
IX	indexes of fixed parameters
NODP	number of data points being fit
P(I)	best-least-squares value of the Ith parameters
PART(I)	partial derivative of the function with respect to the Ith parameter
PG(I)	input values of the Ith parameter

Subroutine BSS

This is the Linear System Solver (LSS) subroutine,[1] except for minor changes.

Subroutine DINSET

Most of the input data are processed by this subroutine (see also subroutine PLOTGN). The input data is entered into the computer by cards and by magnetic tape. Tape 10 refers to the card input file, and Tape 7 refers to the magnetic tape input.

The magnetic tape input contains the 4096-channel spectra that are to be analyzed. Up to 50 sections of each spectrum can be summed and stored as the dependent variable.

---

[1]The LSS subroutine, LA-FD04, may be obtained by writing to C Division of the Los Alamos Scientific Laboratory.

This version of DINSET was written to analyze spectra that were accumulated in clock time, and a 60-Hz pulser with a constant output voltage was used to indicate the dead time for each spectrum.

The more important variables used in this subroutine are listed in Table 10.

Live Time Calculation

Constant voltage pulses from a 60-Hz pulser were recorded and used to determine the live time during the count intervals. The total counts in the pulser peak were determined by summing 29 channels above to 30 channels below the peak channel. (The peak channel number is input for the first spectrum.) After the first spectrum, the value determined from the previous spectrum is used for the peak channel number. From this sum, the counts in 30 channels below and 30 channels above this region are subtracted for background. The channel containing the most counts in this calculation is used as the peak pulser channel for the following spectrum to be analyzed. This allows the code to accommodate slight changes in the system gain or pulser input voltage.

Input Formats and Data

The format on the magnetic tape input is:

Record Number	Information
1	89999 first record of data set
2	00001 data set number
3	80 BCD characters, title information
4	90001 control character and spectrum number
5 to 192	spectral data

The above sequence from Record 4 is repeated for each spectrum on the tape.

TABLE 10

SUBROUTINE DINSET VARIABLES

DTSEC	clock time for each data accumulation
IK	total number of parameters
IM	number of fixed parameters
IPR	print control flag
ITAG1	spectrum number
IX(I)	indexes of fixed parameters
KGMAX(I)	maximum channel of the Ith region of each spectrum that is to be summed
KGMIN(I)	minimum channel of the Ith region of each spectrum that is to be summed
KGROUP	number of regions in each spectrum that are to be summed
LLEH	plot control flag
MAXSP	number of the last spectrum that is to be analyzed
MINSP	number of the first spectrum that is to be analyzed
NODP	number of data points that have been generated and are to be fitted
NOI	number of exponentials to be used in the fit
NOIT	maximum number of iterations that are allowed before forced convergence
NPUL	channel containing the most counts in the pulser peak
OTIME	elapsed time (sec) from when the irradiation stopped until the start time of the first spectrum to be analyzed
PG(I)	initial input values of the parameters
TITT(I)	title information (80 BCD characters)
TLIVE	live-time (sec) calculated from the pulser peak
W(I)	statistical weight of the Ith data point
X(I)	elapsed time (sec) from when the irradiation stopped until the accumulation of data started for the Ith data point
Y(I)	counts/sec calculated for the Ith data point
YY(I)	storage for the 4096-channel spectrum

The card inputs (Tape 10) are:

Card Sequence	Information
1	READ (10,90) (TITT(I),I=1,8) FORMAT (8A10) This is the title card.
2	READ (10,95) NOI,IM,(IX(I),I=1,IM) FORMAT (18I3) NOI is the number of exponentials. IM is the number of fixed parameters. IX(I) are the indexes of the fixed parameters.
3	READ (10,100) PG(1) FORMAT (E12.7) PG(1) is the normalizing parameter. It is used when a set of exponentials is fitted to data. Usually the value of this parameter is 1.0.
4 to 3 + NOI	READ (10,100) (PG(I),I=2,IK) FORMAT (2E12.7) PG(I), I even, are the amplitudes of the Ith exponential at zero time in counts/sec. PG(I), I odd, are the slopes of the Ith exponential. These are decay constants in sec^{-1}. One card containing the amplitude and slope is required for each exponential.
4 + NOI	READ (10,105) KGROUP,NOIT,IPR,LLEH,NPUL FORMAT (12I6) KGROUP is the number of regions that are to be summed in each spectrum for the dependent variable. Fifty regions may be defined. NOIT is the maximum number of iterations that is allowed before convergence is forced. A normal problem should have converged in 25 iterations.

Card Sequence	Information
	IPR is the print control flag. = 0, do not print the parameter values after each iteration. ≠ 0, print the parameter values after each iteration.
	LLEH is the plot control flag. = 1, read in card containing the plot parameters. ≠ 1, plot code generates its own plot parameters.
	NPUL is the channel containing the maximum number of counts in the pulser peak for the first spectrum.
5 + NOI to 4 + NOI - KGROUP	READ (10,105) KGMIN(I),KGMAX(I) FORMAT (12I6) These are the minimum and maximum channels for the Ith region to be summed in each spectrum.
5 + NOI + KGROUP	READ (10,120) OTIME,DTSEC,MINSP,MAXSP FORMAT (2F12.0,2I6) OTIME is the elapsed time (sec) from when the irradiation stopped until the first spectrum to be analyzed. DTSEC is the clock time for the accumulation of each spectrum. 2.14 sec is added to this time to obtain the elapsed time between spectra. MINSP is the number of the first spectrum that is to be analyzed. MAXSP is the number of the last spectrum that is to be analyzed.

The above card may be repeated if you desire to analyze more than one section of data from Tape 7.

BLANK CARD	A blank card is used to indicate the end of the above input.
PLOT CARD	If the plot control flag (LLEH) equals 1, an additional card is necessary. READ (10,145) XL,XR,YT,YB,KDY

Card Sequence	Information
PLOT CARD (continued)	FORMAT (4E12.7,I6)
	XL is the left boundary of the plot.
	XR is the right boundary of the plot.
	YT is the $\log_{10}$ (top boundary).
	YB is the $\log_{10}$ (bottom boundary).
	KDY is the number of vertical lines dividing the X axis. One-half of these lines will be scaled.

Subroutine MAZGN

This subroutine does the least-squares fit to the data using techniques of Moore and Zeigler (Ref. 41). Bounds and other restrictions are placed on the parameters so that convergence is obtained even for poor data or, in some cases, for poor initial guesses for the initial values of the parameters.

If an exponential amplitude, P(2*I), tries to change sign during an iteration, the calculated value for this parameter is set to P(2*I)/2.0. If this results in a value that is less than Y(N)/5000.0, the parameter is then fixed at a value equal to Y(N)/5000.0, where the N subscript refers to the last data point.

The exponential slopes, P(2*I+1), are not allowed to change sign. If an exponential slope tries to change sign during an iteration, this parameter is fixed at its initial input value. The calculated values for the exponential slopes must remain within a factor of 2 of their initial input values. If these bounds are exceeded, the parameter is fixed at its initial input value. The iteration number is not incremented for an iteration where a parameter was fixed.

The more important variables used in this subroutine are listed in Table 11.

TABLE 11

SUBROUTINE MAZGN VARIABLES

AM(I,J)	matrix elements
BM(I,J)	matrix elements
DP(I)	correction to Ith parameter for one iteration
FAZZ	lower bound of the exponential amplitudes
IK	number of parameters
IM	number of fixed parameters
IPLTFL	flag that determines type of calculation to be made by the PHICAL subroutine
IPR	output flag
IT	iteration number
IX(I)	indexes of the fixed parameters
K	number of free parameters
LIES	convergence flag
N	number of data points
NOIT	number of iterations before forced convergence
P(I)	best value of the Ith parameter
PART(I)	partial derivatives
PC(I)	just-calculated value of the Ith parameter
PG(I)	initial estimate of the Ith parameter
SP(I)	deviation of the Ith parameter
TEST	convergence factor
W(I)	statistical weight of the Ith data point
WVAR	weighted variance
X(I)	independent variable
Y(I)	dependent variable
YC(I)	calculated value of the function at the Ith data point

Subroutine OUTGN

Essentially all of the output by this code is through this subroutine. The output from a sample problem is given at the end of this appendix. The initial value, calculated value, and standard deviation are printed for each parameter. The data point number, weight, independent variable, dependent variable, calculated function, deviation, and standard deviation of the predicted mean are printed for each data point.

Since the code will fix parameters if restrictions on sign changes and bounds are not met, the output should be carefully checked to determine which parameters were fixed when the calculation converged. If a parameter is fixed, both the initial guess and calculated value are identical, and the standard deviation of the calculated value is zero.

The more important variables used in this subroutine are listed in Table 12.

Subroutine PHICAL

This subroutine evaluates the function for use in the plot routine, calculates the sum of the squares of the deviations or calculates the weighted sum of the squares of the deviation that is used to calculate the weighted variance. IPLTFL indicates which of the above options is to be calculated. If IPLTFL = 1, the function is evaluated for each X(I) and stored as Y(I), destroying the original Y(I). If IPLTFL = 2, the sum of the squares of the deviations is calculated and stored as PHI. If IPLTFL = 3, the weighted sum of the squares of the deviations is calculated and stored as WVAR. This variable is later used to calculate the weighted variance. For both IPLTFL = 2 and = 3, it is assumed that the original Y(I)'s are stored.

TABLE 12

SUBROUTINE OUTGN VARIABLES

B(I)	best values of the parameters
DY(I)	deviation of the function at the Ith data point
IB(I)	indexes of the fixed parameters
IK	number of parameters
IP	number of fixed parameters
IT	number of iterations
NODP	number of data points
NOI	number of exponentials
PDD	standard deviation of the predicted mean
PG(I)	initial value of the Ith parameter
SA(I)	standard deviation of Ith parameter
TITT(I)	title information
W(I)	statistical weight of Ith data point
WVAR	weighted variance of the fit
X(I)	independent variable
Y(I)	dependent variable
YC(I)	calculated value of the function at the Ith data point

The more important variables used in this subroutine are listed in Table 13.

TABLE 13

SUBROUTINE PHICAL VARIABLES

IPLTFL	control flag for type of calculation
NODP	number of data points
NOI	number of exponentials
P(I)	best value of the Ith parameter
PHI	sum of the squares of the deviations
W(I)	statistical weight of the Ith data point
WVAR	weighted sum of the squares of the deviations
X(I)	independent variable
Y(I)	dependent variable

Subroutine PLOTGN

Subroutine plotgn is used to plot the data using the SC4020 plotter. Variable LLEH determines if the plot boundaries are to be determined by the subroutine or read as part of the card input. This plot option was discussed in the section on the DINSET subroutine.

The plots generated are semi-log. The dependent variable is counts/sec, and the independent variable is decay time after the irradiation in sec. The data points, the calculated function, and the individual exponentials are plotted.

The standard boundaries that are determined by the subroutine, LLEH $\neq$ 1, are set so that only complete cycles are plotted, and all but the bottom cycle will contain data points. The left boundary will be 100 sec less than the first data point truncated to the nearest 100 sec.

Similarly, the right boundary will be 100 sec greater than the last data point truncated to the nearest 100 sec.

This subroutine uses the X's and Y's as temporary storage and destroys the original data after plotting it.

The following subroutines,[1] written for using the SC 4020 plotter have been used in the PLOTGN subroutine.

Number	Subroutine Called
LA JE06	ADV, FRAME, EMPTY
LA JE07	DGA, DLNLG, SLLOG, SBLIN, PLOT
LA JE09	WLCV, WLCH

The more important variables used in this subroutine are listed in Table 14.

Table 14.

TABLE 14

SUBROUTINE PLOTGN VARIABLES

A(I)	labels for the plot axes
B(I)	best values of the parameters
IPLTFL	flag for PHICAL subroutine
LLEH	plot flag
NODP	number of data points
NOI	number of exponentials
TITT	title information
X(I)	independent variable
XL	left plot boundary
XR	right plot boundary
Y(I)	dependent variable
YB	$\log_{10}$ (bottom boundary)
YT	$\log_{10}$ (top boundary)

[1]Copies of these subroutines may be obtained by writing to C Division of the Los Alamos Scientific Laboratory.

Subroutine YP

This subroutine evaluates the function and calculates the partial derivatives of the function with respect to each parameter. The function is

$$Y(J) = P(1)*\sum_{I=1}^{NOI} P(I*2)*EXP(P(I*2+1)*X(J))$$

where J refers to the Jth data point and I refers to the Ith exponential. This subroutine is entered for each data point during each iteration performed by the MAZGN subroutine.

The more important variables used in this subroutine are listed in Table 15.

TABLE 15

SUBROUTINE YP VARIABLES

NOI	number of exponentials
P(I)	best values of the parameters
PART(I)	partial derivatives
YT	value of the function
ZZA	value of X where the function is evaluated

Sample Problem

Input for a sample problem and the output from it are presented on the following pages. This code is available for distribution from the author and will be copied and sent to those wishing to use it.

SAMPLE INPUT FOR DECURA CODE

```
THIN CARBON  3HE ACTIVATION.
  4  4  1  3  7  9
1.0       E+0
1.7080    E+4-.54759  E-3
6.5360    E+3-.12609  E-2
6.2965    E+2-.1050223E-3
5.0349    E+20.0        E+0
      2     25      1       1  1938
   150  1000
  2200  3050
2415.82       100.0                37    108

0.0       E+01.0       E+45.0       E+02.0       E+0      10
```

SAMPLE

OUTPUT

FOR

DECURA CODE

GROUP 1 CHANNEL 150 TO CHANNEL 1000

GROUP 2 CHANNEL 2200 TO CHANNEL 3050

X	Y	W	LIVE TIME
1938 2.41582E+03	1.21760E+04	5.00165E-03	6.09000E+01
1938 2.51796E+03	1.14380E+04	5.45694E-03	6.24167E+01
1939 2.62010E+03	1.06902E+04	6.01173E-03	6.42667E+01
1939 2.72224E+03	1.01033E+04	6.47148E-03	6.53833E+01
1939 2.82438E+03	9.65371E+03	6.83157E-03	6.59500E+01
1939 2.92652E+03	8.94121E+03	7.64438E-03	6.83500E+01
1940 3.02866E+03	8.49295E+03	8.15774E-03	6.92833E+01
1939 3.13080E+03	8.00661E+03	8.81980E-03	7.06167E+01
1940 3.23294E+03	7.55426E+03	9.50677E-03	7.18167E+01
1939 3.33508E+03	7.18114E+03	1.00982E-02	7.25167E+01
1940 3.43722E+03	6.80684E+03	1.08273E-02	7.37000E+01
1940 3.53936E+03	6.44414E+03	1.15893E-02	7.46833E+01
1940 3.64150E+03	6.21878E+03	1.19664E-02	7.44167E+01
1940 3.74364E+03	5.83070E+03	1.30831E-02	7.62833E+01
1941 3.84578E+03	5.61632E+03	1.35112E-02	7.58833E+01
1941 3.94792E+03	5.33452E+03	1.44280E-02	7.69667E+01
1940 4.05006E+03	5.02930E+03	1.56151E-02	7.85333E+01
1941 4.15220E+03	4.78771E+03	1.65737E-02	7.93500E+01
1941 4.25434E+03	4.54546E+03	1.75963E-02	7.99833E+01
1941 4.35648E+03	4.36329E+03	1.83921E-02	8.02500E+01
1941 4.45862E+03	4.14440E+03	1.96369E-02	8.13833E+01
1941 4.56076E+03	3.91192E+03	2.11149E-02	8.26000E+01
1941 4.66290E+03	3.79810E+03	2.16551E-02	8.22500E+01
1942 4.76504E+03	3.61209E+03	2.30614E-02	8.33000E+01
1941 4.86718E+03	3.47619E+03	2.39534E-02	8.32667E+01
1941 4.96932E+03	3.30395E+03	2.55149E-02	8.43000E+01

1942 5.07146E+03	3.23043E+03	2.57860E-02	8.33000E+01
1941 5.17360E+03	3.06146E+03	2.76012E-02	8.45000E+01
1942 5.27574E+03	2.89801E+03	2.97158E-02	8.61167E+01
1942 5.37788E+03	2.78304E+03	3.11351E-02	8.66500E+01
1941 5.48002E+03	2.68422E+03	3.22689E-02	8.66167E+01
1942 5.58216E+03	2.60488E+03	3.33157E-02	8.67833E+01
1941 5.68430E+03	2.50508E+03	3.45231E-02	8.64833E+01
1942 5.78644E+03	2.42754E+03	3.56465E-02	8.65333E+01
1942 5.88858E+03	2.29227E+03	3.87317E-02	8.87833E+01
1942 5.99072E+03	2.24599E+03	3.89583E-02	8.75000E+01
1942 6.09286E+03	2.14780E+03	4.10342E-02	8.81333E+01
1942 6.19500E+03	2.08989E+03	4.22032E-02	8.82000E+01
1942 6.29714E+03	2.00495E+03	4.43071E-02	8.88333E+01
1942 6.39928E+03	1.93959E+03	4.60063E-02	8.92333E+01
1943 6.50142E+03	1.89437E+03	4.67173E-02	8.85000E+01
1943 6.60356E+03	1.81319E+03	4.97465E-02	9.02000E+01
1942 6.70570E+03	1.77043E+03	5.07409E-02	8.98333E+01
1942 6.80784E+03	1.70462E+03	5.31594E-02	9.06167E+01
1942 6.90998E+03	1.67889E+03	5.34482E-02	8.97333E+01
1943 7.01212E+03	1.61451E+03	5.61057E-02	9.05833E+01
1943 7.11426E+03	1.56199E+03	5.79603E-02	9.05333E+01
1943 7.21640E+03	1.52514E+03	5.96119E-02	9.09167E+01
1942 7.31854E+03	1.47191E+03	6.23908E-02	9.18333E+01
1943 7.42068E+03	1.44193E+03	6.37226E-02	9.18833E+01
1943 7.52282E+03	1.41364E+03	6.46793E-02	9.14333E+01
1942 7.62496E+03	1.37368E+03	6.67185E-02	9.16500E+01
1942 7.72710E+03	1.33404E+03	6.90511E-02	9.21167E+01
1943 7.82924E+03	1.31159E+03	7.00551E-02	9.18833E+01
1943 7.93138E+03	1.28425E+03	7.13126E-02	9.15833E+01
1942 8.03352E+03	1.24728E+03	7.40949E-02	9.24167E+01
1943 8.13566E+03	1.22080E+03	7.58791E-02	9.26333E+01

1943			
8.23780E+03	1.20000E+03	7.68750E-02	9.22500E+01
1942			
8.33994E+03	1.17259E+03	7.90558E-02	9.27000E+01
1943			
8.44208E+03	1.14998E+03	8.04794E-02	9.25500E+01
1943			
8.54422E+03	1.12875E+03	8.20378E-02	9.26000E+01
1942			
8.64636E+03	1.09490E+03	8.51980E-02	9.32833E+01
1943			
8.74850E+03	1.09163E+03	8.47964E-02	9.25667E+01
1943			
8.85064E+03	1.07349E+03	8.63380E-02	9.26833E+01
1943			
8.95278E+03	1.03635E+03	9.05423E-02	9.38333E+01
1942			
9.05492E+03	1.03485E+03	8.99489E-02	9.30833E+01
1942			
9.15706E+03	1.01220E+03	9.19777E-02	9.31000E+01
1943			
9.25920E+03	1.00070E+03	9.33850E-02	9.34500E+01
1943			
9.36134E+03	9.83748E+02	9.45533E-02	9.30167E+01
1943			
9.46348E+03	9.72422E+02	9.55347E-02	9.29000E+01
1943			
9.56562E+03	9.54655E+02	9.81856E-02	9.37333E+01
1943			
9.66776E+03	9.44264E+02	9.85247E-02	9.30333E+01

1

1	1.0000000E+00	1.0000000E+00	1.0000000E+00	0.
2	1.7080000E+04	1.7080000E+04	3.5081448E+04	1.8001448E+04
3	-5.4759000E-04	-5.4759000E-04	-5.4759000E-04	0.
4	6.5360000E+03	6.5360000E+03	3.5821471E+04	2.9285471E+04
5	-1.2609000E-03	-1.2609000E-03	-1.2609000E-03	0.
6	6.2965000E+02	6.2965000E+02	7.5950347E+02	1.2985347E+02
7	-1.0502230E-04	-1.0502230E-04	-1.0502230E-04	0.
8	5.0349000E+02	5.0349000E+02	4.9072435E+02	-1.2765647E+01
9	0.	0.	0.	0.

2

1	1.0000000E+00	1.0000000E+00	1.0000000E+00	0.
2	1.7080000E+04	3.5081448E+04	3.5081448E+04	1.0930527E-07
3	-5.4759000E-04	-5.4759000E-04	-5.4759000E-04	0.
4	6.5360000E+03	3.5821471E+04	3.5821471E+04	-4.8629305E-07
5	-1.2609000E-03	-1.2609000E-03	-1.2609000E-03	0.
6	6.2965000E+02	7.5950347E+02	7.5950347E+02	-2.6744801E-08
7	-1.0502230E-04	-1.0502230E-04	-1.0502230E-04	0.
8	5.0349000E+02	4.9072435E+02	4.9072435E+02	9.9273071E-09
9	0.	0.	0.	0.

3

1	1.0000000E+00	1.0000000E+00	1.0000000E+00	0.
2	1.7080000E+04	3.5081448E+04	3.5081448E+04	7.8232239E-11
3	-5.4759000E-04	-5.4759000E-04	-5.4759000E-04	0.
4	6.5360000E+03	3.5821471E+04	3.5821471E+04	-3.2238470E-10
5	-1.2609000E-03	-1.2609000E-03	-1.2609000E-03	0.
6	6.2965000E+02	7.5950347E+02	7.5950347E+02	3.9019678E-12
7	-1.0502230E-04	-1.0502230E-04	-1.0502230E-04	0.
8	5.0349000E+02	4.9072435E+02	4.9072435E+02	2.1026878E-12

9	0.	0.	0.	0.
4				
1	1.0000000E+00	1.0000000E+00	1.0000000E+00	0.
2	1.7080000E+04	3.5081448E+04	3.5081448E+04	-9.5842729E-11
3	-5.4759000E-04	-5.4759000E-04	-5.4759000E-04	0.
4	6.5360000E+03	3.5821471E+04	3.5821471E+04	9.1558310E-10
5	-1.2609000E-03	-1.2609000E-03	-1.2609000E-03	0.
6	6.2965000E+02	7.5950347E+02	7.5950347E+02	5.1158139E-11
7	-1.0502230E-04	-1.0502230E-04	-1.0502230E-04	0.
8	5.0349000E+02	4.9072435E+02	4.9072435E+02	-1.9655624E-11
9	0.	0.	0.	0.
5				
1	1.0000000E+00	1.0000000E+00	1.0000000E+00	0.
2	1.7080000E+04	3.5081448E+04	3.5081448E+04	6.2354694E-11
3	-5.4759000E-04	-5.4759000E-04	-5.4759000E-04	0.
4	6.5360000E+03	3.5821471E+04	3.5821471E+04	1.9317457E-09
5	-1.2609000E-03	-1.2609000E-03	-1.2609000E-03	0.
6	6.2965000E+02	7.5950347E+02	7.5950347E+02	3.4884963E-12
7	-1.0502230E-04	-1.0502230E-04	-1.0502230E-04	0.
8	5.0349000E+02	4.9072435E+02	4.9072435E+02	1.3387086E-12
9	0.	0.	0.	0.
6				
1	1.0000000E+00	1.0000000E+00	1.0000000E+00	0.
2	3.5081448E+04	3.5081448E+04	3.6298332E+04	1.2168837E+03
3	-5.4759000E-04	-5.4759000E-04	-5.4759000E-04	0.
4	3.5821471E+04	3.5821471E+04	4.3242661E+04	7.4211896E+03
5	-1.2609000E-03	-1.2609000E-03	-1.4023161E-03	-1.4141607E-04
6	7.5950347E+02	7.5950347E+02	5.8921999E+02	-1.7028348E+02
7	-1.0502230E-04	-1.0502230E-04	-1.0502230E-04	0.
8	4.9072435E+02	4.9072435E+02	5.4886137E+02	5.8137014E+01
9	0.	0.	0.	0.
7				
1	1.0000000E+00	1.0000000E+00	1.0000000E+00	0.
2	3.5081448E+04	3.6298332E+04	3.6211364E+04	-8.6967857E+01
3	-5.4759000E-04	-5.4759000E-04	-5.4759000E-04	0.
4	3.5821471E+04	4.3242661E+04	4.6627804E+04	3.3851433E+03
5	-1.2609000E-03	-1.4023161E-03	-1.4238625E-03	-2.1546416E-05
6	7.5950347E+02	5.8921999E+02	5.9105791E+02	1.8379210E+00
7	-1.0502230E-04	-1.0502230E-04	-1.0502230E-04	0.
8	4.9072435E+02	5.4886137E+02	5.4867033E+02	-1.9103460E-01
9	0.	0.	0.	0.
8				
1	1.0000000E+00	1.0000000E+00	1.0000000E+00	0.
2	3.5081448E+04	3.6211364E+04	3.6222945E+04	1.1581428E+01
3	-5.4759000E-04	-5.4759000E-04	-5.4759000E-04	0.
4	3.5821471E+04	4.6627804E+04	4.6885162E+04	2.5735794E+02
5	-1.2609000E-03	-1.4238625E-03	-1.4255952E-03	-1.7327313E-06
6	7.5950347E+02	5.9105791E+02	5.8906264E+02	-1.9952654E+00
7	-1.0502230E-04	-1.0502230E-04	-1.0502230E-04	0.
8	4.9072435E+02	5.4867033E+02	5.4936881E+02	6.9847711E-01
9	0.	0.	0.	0.
9				
1	1.0000000E+00	1.0000000E+00	1.0000000E+00	0.
2	3.5081448E+04	3.6222945E+04	3.6224062E+04	1.1164241E+00
3	-5.4759000E-04	-5.4759000E-04	-5.4759000E-04	0.
4	3.5821471E+04	4.6885162E+04	4.6902058E+04	1.6896126E+01

```
 5   -1.2609000E-03   -1.4255752E-03   -1.4257914E-03   -1.9617232E-07
 6    7.5950347E+02    5.8906204E+02    5.8888244E+02   -1.8020123E-01
 7   -1.0502230E-04   -1.0502230E-04   -1.0502230E-04    0.
 8    4.9072435E+02    5.4936081E+02    5.4943142E+02    6.2613037E-02
 9    0.               0.               0.               0.

10
 1    1.0000000E+00    1.0000000E+00    1.0000000E+00    0.
 2    3.5081448E+04    3.6224062E+04    3.6224190E+04    1.2803566E-01
 3   -5.4759000E-04   -5.4759000E-04   -5.4759000E-04    0.
 4    3.5821471E+04    4.6902098E+04    4.6903934E+04    1.8759023E+00
 5   -1.2609000E-03   -1.4257914E-03   -1.4258140E-03   -2.2625112E-08
 6    7.5950347E+02    5.8888244E+02    5.8886186E+02   -2.0579870E-02
 7   -1.0502230E-04   -1.0502230E-04   -1.0502230E-04    0.
 8    4.9072435E+02    5.4943142E+02    5.4943857E+02    7.1470950E-03
 9    0.               0.               0.               0.

11
 1    1.0000000E+00    1.0000000E+00    1.0000000E+00    0.
 2    3.5081448E+04    3.6224190E+04    3.6224205E+04    1.4788058E-02
 3   -5.4759000E-04   -5.4759000E-04   -5.4759000E-04    0.
 4    3.5821471E+04    4.6903934E+04    4.6904150E+04    2.1586755E-01
 5   -1.2609000E-03   -1.4258140E-03   -1.4258166E-03   -2.6088988E-09
 6    7.5950347E+02    5.8886186E+02    5.8885948E+02   -2.3758598E-03
 7   -1.0502230E-04   -1.0502230E-04   -1.0502230E-04    0.
 8    4.9072435E+02    5.4943857E+02    5.4943939E+02    8.2505552E-04
 9    0.               0.               0.               0.

12
 1    1.0000000E+00    1.0000000E+00    1.0000000E+00    0.
 2    3.5081448E+04    3.6224205E+04    3.6224206E+04    1.7054925E-03
 3   -5.4759000E-04   -5.4759000E-04   -5.4759000E-04    0.
 4    3.5821471E+04    4.6904150E+04    4.6904175E+04    2.4885197E-02
 5   -1.2609000E-03   -1.4258166E-03   -1.4258169E-03   -3.0020077E-10
 6    7.5950347E+02    5.8885948E+02    5.8885921E+02   -2.7399091E-04
 7   -1.0502230E-04   -1.0502230E-04   -1.0502230E-04    0.
 8    4.9072435E+02    5.4943939E+02    5.4943949E+02    9.5147131E-05
 9    0.               0.               0.               0.

THIN CARBON  3HE ACTIVATION.

 K          GUESS              CALCULATED              DEVIATION
 1    1.0000000E+00    1.0000000E+00    0.  PHC
 2    3.5081448E+04    3.6224206E+04    8.0104198E+02
 3   -5.4759000E-04   -5.4759000E-04    0.  PHC
 4    3.5821471E+04    4.6904175E+04    1.1118254E+04
 5   -1.2609000E-03   -1.4258169E-03    1.3215100E-04
 6    7.5950347E+02    5.8885921E+02    1.4374753E+02
 7   -1.0502230E-04   -1.0502230E-04    0.  PHC
 8    4.9072435E+02    5.4943949E+02    5.1523437E+01
 9    0.               0.               0.  PHC

13 ITERATIONS

WEIGHTED VARIANCE = 1.0821365E+01

NUMBER OF DATA POINTS FIT =  74

NUMBER OF LINES =  4
```

I	WEIGHT	VARIABLE	VARIABLE	FUNCTION	DEVIATION	PREDICTED MEAN
1	5.0016453E-03	2.4138200E+03	1.2175994E+04	1.2152479E+04	2.3514887E+01	2.7455521E+00
2	5.4569398E-03	2.5419600E+03	1.1438035E+04	1.1419838E+04	1.8196796E+01	1.8069208E+00
3	6.0117324E-03	2.6621000E+03	1.0690207E+04	1.0743298E+04	-5.3090718E+01	1.6944816E+01
4	6.4714773E-03	2.7622400E+03	1.0103309E+04	1.0117579E+04	-1.4270327E+01	1.3178662E+00
5	6.8315723E-03	2.8243800E+03	9.6537074E+03	9.5379896E+03	1.1571772E+02	9.1478792E+01
6	7.6443755E-03	2.9695200E+03	8.9412143E+03	9.0003558E+03	-5.9141415E+01	2.6737785E+01
7	8.1577449E-03	3.0286600E+03	8.4929516E+03	8.5009561E+03	-8.0044532E+00	5.2267709E-01
8	8.8197977E-03	3.1398000E+03	8.0066084E+03	8.0364671E+03	-2.9858676E+01	7.8632073E+00
9	9.5067732E-03	3.2469400E+03	7.5542632E+03	7.6039149E+03	-4.9651727E+01	2.3436991E+01
10	1.0098217E-02	3.3390800E+03	7.1811354E+03	7.2006332E+03	-1.9497833E+01	3.8389940E+00
11	1.0823473E-02	3.4212200E+03	6.8068385E+03	6.8242270E+03	-1.7388502E+01	3.2737566E+00
12	1.1589337E-02	3.5036600E+03	6.4441419E+03	6.4725407E+03	-2.8398793E+01	9.3467015E+00
13	1.1966438E-02	3.6415000E+03	6.2187816E+03	6.1436301E+03	7.5151489E+01	6.7583907E+01
14	1.3083056E-02	3.7436400E+03	5.8306970E+03	5.8357384E+03	-5.0414611E+00	3.3252926E-01
15	1.3511222E-02	3.8457800E+03	5.6163189E+03	5.5472747E+03	6.9044203E+01	6.4409374E+01
16	1.4428048E-02	3.9479200E+03	5.3345171E+03	5.2767956E+03	5.7721525E+01	4.8071001E+01
17	1.5615150E-02	4.0560600E+03	5.0293039E+03	5.0229888E+03	6.3151119E+00	6.2274213E-01
18	1.6573676E-02	4.1562000E+03	4.7877127E+03	4.7846590E+03	3.0536879E+00	1.5454969E-01
19	1.7596314E-02	4.2543400E+03	4.5454595E+03	4.5607151E+03	-1.5255661E+01	4.0952818E+00
20	1.8392086E-02	4.3564800E+03	4.3632897E+03	4.3501596E+03	1.3130116E+01	3.1707954E+00
21	1.9636945E-02	4.4586200E+03	4.1443989E+03	4.1520784E+03	-7.6794664E+00	1.1580732E+00
22	2.1114925E-02	4.5607600E+03	3.9119249E+03	3.9656327E+03	-5.3707718E+01	6.0904400E+01
23	2.1655130E-02	4.6629000E+03	3.7981763E+03	3.7900511E+03	8.1251951E+00	1.4296456E+00
24	2.3061448E-02	4.7650400E+03	3.6120888E+03	3.6246234E+03	-1.2534545E+01	3.6232954E+00
25	2.3953408E-02	4.8671800E+03	3.4761930E+03	3.4686942E+03	7.4987363E+00	1.3466252E+00
26	2.5514913E-02	4.9693200E+03	3.3039502E+03	3.3216581E+03	-1.7707965E+01	8.0007629E+00
27	2.5786024E-02	5.0714600E+03	3.2304322E+03	3.1829549E+03	4.7477291E+01	5.8124098E+01
28	2.7601249E-02	5.1736000E+03	3.0614556E+03	3.0520652E+03	9.3903891E+00	2.4334618E+00
29	2.9715789E-02	5.2757400E+03	2.8980105E+03	2.9285074E+03	-3.0496936E+01	2.7637558E+01
30	3.1135072E-02	5.3778800E+03	2.7830352E+03	2.8118337E+03	-2.8798462E+01	2.5821915E+01
31	3.2268857E-02	5.4800200E+03	2.6842178E+03	2.7016276E+03	-1.7409741E+01	9.7806633E+00
32	3.3315699E-02	5.5821600E+03	2.6048780E+03	2.5975011E+03	7.3768999E+00	1.8129954E+00

33	3.4523129E-02	5.6853000E+03	2.5050838E+03	2.4990927E+03	5.9911233E+00	1.2391581E+00
34	3.5646534E-02	5.7004400E+03	2.4275385E+03	2.4060646E+03	2.1473922E+01	1.6437661E+01
35	3.6731692E-02	5.8885800E+03	2.2922658E+03	2.3181014E+03	-2.5835549E+01	2.5852454E+01
36	3.8958346E-02	5.9907200E+03	2.2459886E+03	2.2349080E+03	1.1080576E+01	4.7832724E+00
37	4.1034197E-02	6.0728600E+03	2.1478026E+03	2.1562084E+03	-8.4058070E+00	2.8993768E+00
38	4.2203246E-02	6.1490000E+03	2.0898866E+03	2.0817439E+03	8.1427474E+00	2.7987582E+00
39	4.4307104E-02	6.2271400E+03	2.0049456E+03	2.0112720E+03	-6.3264410E+00	1.7733412E+00
40	4.6006308E-02	6.3072800E+03	1.9395891E+03	1.9445654E+03	-4.9763321E+00	1.1392948E+00
41	4.6717307E-02	6.3914200E+03	1.8943729E+03	1.8814106E+03	1.2962306E+01	7.8490568E+00
42	4.9746500E-02	6.4735600E+03	1.8131929E+03	1.8216070E+03	-8.4140800E+00	3.5218501E+00
43	5.0740850E-02	6.5557000E+03	1.7704341E+03	1.7649662E+03	5.4678980E+00	1.5176453E+00
44	5.3159447E-02	6.6378400E+03	1.7046202E+03	1.7113112E+03	-6.6909946E+00	2.3799170E+00
45	5.3448153E-02	6.7199800E+03	1.6788856E+03	1.6604752E+03	1.8410388E+01	1.8115844E+01
46	5.6105658E-02	7.0121200E+03	1.6145133E+03	1.6123015E+03	2.2118873E+00	2.7449386E-01
47	5.7960318E-02	7.1142600E+03	1.5619882E+03	1.5666423E+03	-4.6540960E+00	1.2554958E+00
48	5.9611861E-02	7.2164000E+03	1.5251439E+03	1.5233587E+03	1.7851628E+00	1.8997144E-01
49	6.2390775E-02	7.3185400E+03	1.4719056E+03	1.4823197E+03	-1.0414114E+01	6.7664148E+00
50	6.3722626E-02	7.4206800E+03	1.4419264E+03	1.4434019E+03	-1.4754982E+00	1.3873020E-01
51	6.4679271E-02	7.5228200E+03	1.4136420E+03	1.4064887E+03	7.1532954E+00	3.3096147E+00
52	6.6718474E-02	7.6249600E+03	1.3736825E+03	1.3714705E+03	2.2119461E+00	3.2643386E-01
53	6.9051082E-02	7.7271000E+03	1.3340365E+03	1.3382439E+03	-4.2073139E+00	1.2223070E+00
54	7.0055072E-02	7.8292400E+03	1.3115872E+03	1.3067110E+03	4.8761481E+00	1.6656568E+00
55	7.1312636E-02	7.9313800E+03	1.2842511E+03	1.2767798E+03	7.4712999E+00	3.9806942E+00
56	7.4094859E-02	8.0335200E+03	1.2472750E+03	1.2483634E+03	-1.0883539E+00	8.7766406E-02
57	7.5879053E-02	8.1356600E+03	1.2208024E+03	1.2213795E+03	-5.7708222E-01	2.5269538E-02
58	7.6875000E-02	8.2378000E+03	1.2000000E+03	1.1957508E+03	4.2492148E+00	1.3880917E+00
59	7.9055833E-02	8.3399400E+03	1.1725890E+03	1.1714040E+03	1.1850441E+00	1.1102045E-01
60	8.0479395E-02	8.4420800E+03	1.1499838E+03	1.1482699E+03	1.7138845E+00	2.3640019E-01
61	8.2037848E-02	8.5442200E+03	1.1287473E+03	1.1262834E+03	2.4639389E+00	4.9805134E-01
62	8.5197974E-02	8.6463600E+03	1.0949008E+03	1.1053826E+03	-1.0481796E+01	9.3603355E+00
63	8.4796364E-02	8.7485000E+03	1.0916349E+03	1.0855095E+03	6.1253957E+00	3.1815796E+00
64	8.6338010E-02	8.8506400E+03	1.0734940E+03	1.0666088E+03	6.8851932E+00	4.0926298E+00
65	9.0542290E-02	8.9527800E+03	1.0363481E+03	1.0486286E+03	-1.2280436E+01	1.3654603E+01

66	8.9948892E-02	9.0549200E+03	1.0348469E+03	1.0315197E+03	3.3272506E+00	9.9578789E-01
67	9.1977694E-02	9.1570600E+03	1.0122019E+03	1.0152356E+03	-3.0336489E+00	8.4647309E-01
68	9.3385045E-02	9.2592000E+03	1.0006956E+03	9.9973241E+02	9.6314542E-01	8.6628554E-02
69	9.4553376E-02	9.3634400E+03	9.8374843E+02	9.8496864E+02	-1.2202045E+00	1.4078033E-01
70	9.5534659E-02	9.4534800E+03	9.7242196E+02	9.7090500E+02	1.5169561E+00	2.1984015E-01
71	9.8185552E-02	9.5096200E+03	9.5465505E+02	9.5750441E+02	-2.8493574E+00	7.9714254E-01
72	9.8524737E-02	9.6076600E+03	9.4426370E+02	9.4473177E+02	-4.6806340E-01	2.1585129E-02

APPENDIX B

SURFACE AND VOLUMETRIC CONCENTRATIONS FROM CHARGED-PARTICLE ACTIVATION CODE

Main Program SVCCPA

This code is written in FORTRAN IV for the CDC 6600 computer and calculates the surface concentration in g/cm^2 and the volumetric concentration in $atoms/cm^3$ for the passive ^3He activation analysis. Corrections are made for variations in the beam current during the irradiation.

The incident ^3He particles are followed in 0.01-MeV energy decrements into the sample as they are slowed by ionization energy losses. The calculation is terminated once the ^3He energy reaches 1 MeV. This 1 MeV cutoff energy is arbitrary but satisfactory for the reactions being considered because the cross sections are negligible below this energy.

Calculation of the volumetric impurity concentration is as follows:

$$\frac{dE}{dX} = s(E)$$

$$\Delta X_j = X_{j+1} - X_j = \int_{E_j}^{E_{j+1}} \frac{dE}{s(E)} \quad .$$

The integral, $\int_{E_j}^{E_{j+1}} \frac{dE}{s(E)}$, is determined from the numerical integration of the cubic spline interpolation function S(E), where $S(E) = 1/s(E)$.

The average cross section for each energy step is determined from

$$\bar{\sigma}_j = \frac{\int_{E_{j+1}}^{E_j} \sigma(E)\, dE}{E_{j+1} - E_j} \quad ,$$

where

$$\int_{E_1}^{E_2} \sigma(E)\, dE$$

is determined by numerical integration of the analytical function used to represent $\sigma(E)$.

The concentration of impurity atoms, N_v, is

$$N_v = \frac{R}{\Phi \cdot \sum \bar{\sigma}_j \cdot \Delta X_j} \quad ,$$

where

N_v is the volumetric concentration of impurity atoms (atoms/cm^3),

R is the total number of activation product atoms present,

Φ is the number of incident ^{3}He particles,

$\bar{\sigma}_j$ is the average cross section for the jth energy step, and

ΔX_j is the sample increment corresponding to the jth energy step.

A calculation is also made assuming that all of the impurity atoms are located in a thin layer on the surface of the material being irradiated. This calculation assumes that the energy loss of the ^{3}He particles is small as they pass through this layer. The concentration of surface impurity atoms, N_s (atoms/cm^2), is

$$N_s = \frac{R}{\Phi \cdot \sigma(E_I)} \quad ,$$

where $\sigma(E_I)$ is the cross section corresponding to the incident ^{3}He energy.

The current history of the target was recorded during the irradiations. This allowed corrections to be made for variations in the beam current during the run.

The following is a list of the input required. Most of the input is in the main program.

Card Sequence	Information
1	READ (10,125) (TIT(I),J=1,20)
	FORMAT (20A4)
	Title information 80 BCD characters
2	READ (10,65) (TIT(I),I=1,8)
	FORMAT (8A10)
	READ (10,75) E(J),X(J),M(J)
	FORMAT (3E12.5)
	The CALL TFOX (XX,YY,0) statement in the main program is to enter the TFOX subroutine to read in the title and $1.0/\frac{dE}{dX}$ versus E data for the material being irradiated. A blank card terminates this sequence.
3	READ (10,135) ZOHRS,ZOMIN,ZOSEC
	FORMAT (3F6.0)
	Time of day that run stopped
	ZOHRS hour
	ZOMIN minutes
	ZOSEC seconds
4	READ (10,150) NOISO
	FORMAT (I6)
	Number of impurity isotopes to be calculated: ($\leq$10)

Card Sequence	Information
5	READ (10,155) (AD(I,J),J=1,3),HL(I) FORMAT (3A4,E12.7) AD(I,J) Identification for Ith impurity isotope HL(I) Half-life (sec) for the Ith impurity isotope
6	READ (10,170) SMULT FORMAT (E12.7) Conversion for the current integrator (C/count)
7	READ (10,150) N(I) FORMAT (I6) Number of Gaussians used to represent the ^{3}He cross section for the Ith impurity isotope
8	READ (10,170) (B(I,J),I=1,IK) FORMAT (6E12.7) Parameters used to analytically represent the ^{3}He cross section for the Jth impurity isotope
9	READ (10,170) EMAX,EFF FORMAT (2E12.7) EMAX Maximum ^{3}He energy (MeV) EFF Efficiency of the detector system (%)
10	READ (10,170) (CNTSEC(J),J=1,NOISO) FORMAT (6E12.7) The counts/sec extrapolated to the time that the irradiation stopped for the Jth isotope. These numbers are obtained from the decay curve analysis code (DECURA)

Card Sequence	Information
11	READ (10,170) (DECAYC(J),J=1,NOISO)
	FORMAT (6E12.7)
	Branching ratio for the positron decay (or energy being analyzed) for the Jth isotope
12	READ (10,185) IDATA,THR,TMIN,TSEC,TSTDLT
	FORMAT (I6,4F6.0)
	This is the start of the current integrator history
	IDATA Number of data points in the data set that follows
	THR, TMIN, and TSEC Time of day for the first data point
	TSTDLT Time between integrator dumps (sec)
13	READ (10,180) (INC(I),I=1,IDATA)
	FORMAT (4X,16I4)
	Current integrator data (counts)

Card sequences 12 and 13 are repeated if more than one set of current integrator data is used. A blank card designates the end of the current integrator data.

The more important variables in the main program are listed in Table 16.

Function GFN (A,C,D,E)

This function calculates the number of activation product atoms that were present when the irradiation stopped from those that were born during some current integrator interval.

A Average ^{3}He current during the interval (particles/sec)

B Decay constant (sec^{-1})

TABLE 16

MAIN PROGRAM SVCCPA VARIABLES

AD(I,J)	identification for the Ith impurity isotope
ATOMS(I)	volumetric concentration of the Ith impurity in (atoms/cm^3)
B(J,I)	Jth parameter for the analytical representation of the Ith ^3He cross section
CNTSEC(I)	counts/sec extrapolated to the time the irradiation stopped for the Ith impurity
DECAYC(I)	branching ratio for the positron decay of the activation product from the Ith impurity
DELTT	time (sec) between current integrator dumps
EFF	detector efficiency (%)
EMAX	energy (MeV) of the incident ^3He ions
HL(I)	half-life (sec) of the activation product from the Ith impurity
ICASE	flag that is used to indicate whether or not the E and X data have been read into the memory
IDATA	number of current integrator dumps in the data set that follows
INC(I)	current integrator history data
LAM(I)	decay constant (sec^{-1}) for the reaction product from the Ith impurity
NG(I)	number of Gaussians used for the analytical representation of ^3He cross section for the Ith impurity
NOISO	number of impurities to be calculated
Q	average ^3He flux (particles/sec) striking the target during a current integrator dump
SIGBAR	average ^3He cross section over the energy interval being calculated
SIGDX(I)	average cross section of the irradiated sample volume for the Ith impurity
SMULT	conversion factor for the current integrator (C/count)
SUCAN	cross section for the surface layer

TABLE 16 - continued

SURF	concentration of the surface layer (atoms/cm^2)
TIT(I)	identification information
THR, TMIN, TSEC	time of day for the first integrator dump in the set of data that follows
TSTDLT	time between current integrator dumps (sec) for the set of data that follows
TZ	elapsed time (sec) from a current integrator data point to the end of the irradiation
W(I)	weights for the Gaussian-type numerical integration
X(I)	interval for the Gaussian-type numerical integration
ZION	electronic charge of the incident ion
ZOHRS, ZOMIN, ZOSEC	time of day when the irradiation stopped. For each midnight that was passed during the run, 24.0 should be added to ZOHRS

D Time (sec) between current integrator dumps

E Elapsed time (sec) from the dump until the irradiation stopped.

Subroutine FSIGE

This subroutine is used to evaluate the parameters for the analytical representations of the ^{3}He cross sections. The analytical representation consists of Gaussians with exponential tails on the high-energy side of the Gaussian. These parameters are determined using least-squares techniques and the code GHLET (see Appendix C).

The arguments in the subroutine call statement are:

X ^{3}He energy MeV,

YT Cross section (mb), and

IZ Index of the cross section to be calculated.

Subroutine TFOX

This subroutine solves the cubic spline interpolation function $y = S(E)$, where $S(E) = 1.0/\frac{dE}{dX}$. The data are usually stored from $E = 1.0$ to $E = 12.0$ MeV.

The arguments in the subroutine call statement and more important variables are:

ZZ ^{3}He energy (MeV),

YY Reciprocal of the stopping power (cm/MeV),

L Data input flag,

E(J) Energy of the Jth data point (MeV),

X(J) Reciprocal of the stopping power for the Jth data point (cm/MeV),

M(J) Second derivative at the Jth data point,

TIT(I) Title information for above data, and

NPTS Number of data points.

Sample Problem

Input for a sample problem and the output from it are presented on the following pages. This code is available for distribution from the author and will be copied and sent to those wishing to use it.

SAMPLE INPUT FOR SVCCPA CODE

```
 CARBON CALIBRATICN. 8.6 MEV HE3.
DE/DX  ALUMINUM  PRCTONS  E  1.0/F(E)  M
   1.000000 2.14903E-03 0.
   1.100000 2.27700E-03-2.50691E-04
   1.200000 2.40298E-03-1.95105E-04
   1.300000 2.52700E-03-1.40199E-04
   1.400000 2.64946E-03-1.82332E-04
   1.500000 2.77026E-03-1.29925E-04
   1.600000 2.88966E-03-1.38993E-04
   1.700000 3.00770E-03-1.24956E-04
   1.800000 3.12448E-03-1.16080E-04
   1.900000 3.24008E-03-1.21576E-04
   2.000000 3.35454E-03-8.56547E-05
   2.100000 3.46800E-03-1.27787E-04
   2.200000 3.58032E-03-9.32238E-05
   2.300000 3.69165E-03-9.05289E-05
   2.400000 3.80207E-03-9.01307E-05
   2.500000 3.91159E-03-8.85970E-05
   2.600000 4.02025E-03-7.71874E-05
   2.700000 4.12811E-03-7.38614E-05
   2.800000 4.23524E-03-7.35465E-05
   2.900000 4.34164E-03-6.44820E-05
   3.000000 4.44736E-03-7.72152E-05
   3.100000 4.55235E-03-7.09156E-05
   3.200000 4.65663E-03-5.92151E-05
   3.300000 4.76031E-03-5.40053E-05
   3.400000 4.86341E-03-6.66752E-05
   3.500000 4.96590E-03-5.30359E-05
   3.600000 5.06781E-03-6.95470E-05
```

3.700000	5.16907E-03-5.25549E-05
3.800000	5.26981E-03-3.78246E-05
3.900000	5.37009E-03-6.57015E-05
4.000000	5.46981E-03-4.14416E-05
4.200000	5.66785E-03-5.23306E-05
4.400000	5.86397E-03-3.58682E-05
4.600000	6.05830E-03-7.43066E-05
4.800000	6.25042E-03 2.40026E-06
5.000000	6.44174E-03-5.56028E-05
5.200000	6.63142E-03-2.52543E-05
5.400000	6.81985E-03-3.22893E-05
5.600000	7.00699E-03-3.75084E-05
5.800000	7.19270E-03-3.27753E-05
6.000000	7.37707E-03-3.29840E-05
6.200000	7.56017E-03-2.49344E-05
6.400000	7.74221E-03-2.61398E-05
6.600000	7.92321E-03-2.80925E-05
6.800000	8.10307E-03-3.09159E-05
7.000000	8.28179E-03-1.98440E-05
7.200000	8.45961E-03-2.42357E-05
7.400000	8.63650E-03-2.37040E-05
7.600000	8.81246E-03-1.95699E-05
7.800000	8.98757E-03-2.62008E-05
8.000000	9.16173E-03-1.75916E-05
8.200000	9.33511E-03-1.95497E-05
8.400000	9.50773E-03-2.00209E-05
8.600000	9.67961E-03-9.94760E-06
8.800000	9.85085E-03-3.71538E-05
9.000000	1.00210E-02 8.93602E-07
9.200000	1.01908E-02-2.26927E-05
9.400000	1.03599E-02-1.77455E-05
9.600000	1.05282E-02-2.41786E-05
9.800000	1.06957E-02-1.09897E-05
10.000000	1.08626E-02-1.49527E-05
10.200000	1.10290E-02-9.57263E-06
10.400000	1.11949E-02-2.10043E-05

```
   1C.600000 1.13600E-02-2.24120E-05
   1C.80C000 1.15244E-02 3.71713E-06
   11.000000 1.16886E-02-3.18689E-05
   11.200000 1.18518E-02-6.02679E-06
   11.400000 1.20147E-02 6.60040E-07
   11.600000 1.21774E-02-2.59382E-05
   11.80C000 1.23394E-02-1.70496E-05
   12.000000 1.25006E-02 0.

     6    15    37
     2
 OXYGEN      6.6       E+3
 CARBON      1.23      E+3
2.0       E-9
     1
1.6374    E+01.4613    E-22.6928    E-1-.1794    E+01.5658    E+36.7888    E+C
1.4989    E+0
     3
1.6       E+03.43      E-21.8292    E-1-.18      E+08.8700    E+28.9426    E+2
2.2175    E+25.1215    E+09.2220    E+01.5504    E+11.5       E+C
8.6       E+09.938     E+1
9.4       E+23.87      E+4
1.0       E+01.0       E+0
     1      5     53     47    137
  4878
 132      5     53     47     10
 1       218 220 237 199 135 245 264 259 253 249 241 238 248 364 363     CARBON
 2 368 382 392 395 397 398 426 423 421 414 401 423 426 421 429 424     CARBON
 3 422 425 427 420 424 422 423 422 425 419 421 425 426 424 421 416     CARBON
 4 438 447 450 452 454 457 447 457 455 453 456 454 448 453 453 456     CARBON
 5 451 451 458 456 454 454 459 454 457 455 453 453 455 461 463 463     CARBON
 6 463 456 461 461 459 460 465 460 460 463 454 455 456 455 452 453     CARBON
 7 452 454 459 451 452 448 455 455 456 445 447 454 450 447 454 455     CARBON
 8 451 449 450 407 454 459 457 456 453 452 453 455 450 447 450 453     CARBON
 9 450 451 449 447                                                     CARBON
```

SAMPLE

OUTPUT

FOR

SVCCPA CODE

CARBON CALIBRATION. 8.6 MEV HE3.

DE/DX ALUMINUM PROTONS E 1.0/F(E) M

RUN STOPPED AT 6 HRS 15 MIN 37 SEC

ISOTOPE	HALF-LIFE (SEC)
OXYGEN	6.6000E+03
CARBON	1.2300E+03

CLICK MULTIPLIER = 2.0000E-09

MAXIMUM ION ENERGY = 8.60

COUNTING EFFICIENCY = 99.38PERCENT

ISOTOPE	CNT/SEC	SIGDX	SUM	DECAY CORR.	ATOMS/CC	ATOMS/CM**2
OXYGEN	9.4000E+02	6.0917E+01	3.4913E+14	1.0000E+00	4.2348E+17	7.6254E+16
CARBON	3.8700E+04	7.6933E+01	2.6235E+16	1.0000E+00	3.4237E+18	7.9803E+17

APPENDIX C

GAUSSIAN WITH HIGH AND LOW EXPONENTIAL TAILS FIT CODE

Main Program GHLET

This program, written in FORTRAN IV for the 6600 computer, is similar to the DECURA code discussed in Appendix A and also to the computer code discussed in Ref. 25. The code does a least-squares fit of a Gaussian with high-energy and low-energy exponential tails. In addition to the analytical representation of the total ^{3}He cross sections used in this experiment, the code has been quite useful in the analysis of neutron cross-section data in the resonance region (Ref. 42).

The main program is quite simple and is used only to call subroutines. Subroutine DINSET reads the data into memory and sets up the initial values for the parameters. Subroutine MAZCS is the least-squares portion of the code. Subroutine OUTCS is the output portion of the code, and the PLTZ subroutine plots the data using the SC 4020.

Subroutines in the code that are identical to those mentioned elsewhere in this report will not be discussed.

Subroutine DATA

The data that is to be fitted is read into the computer by this code. The input cards read by this subroutine are:

Card Sequence	Information
1	READ (5,1) (TITLE(J),J=1,8)
	FORMAT (8A10)
	Title information (80 BCD characters)

Card Sequence	Information
2	READ (5,3) NODP FORMAT (I6) Number of data points
3	READ (5,4) XMIN, XMAX FORMAT (2E12.7) Minimum and maximum values of the independent variable to be fitted. If both of these values are zero, all of the data points will be fitted.
4	READ (5,4) ((XIN(I),YIN(I),WIN(I)),I=1,NODP) FORMAT (3E12.7) These are the dependent variable, the independent variable, and the statistical weight for the Ith data point. If the statistical weight is less than 1.0×10^{-10} (e.g., blank), the statistical weight is set equal to 1.0.

Subroutine DINSET

Most of the input to the code takes place in this subroutine. The input cards are:

Card Sequence	Information
1	READ (5,35) (TITLE(J),J=1,20) FORMAT (20A4) Title information (80 BCD characters)
2	READ (5,40) NOI, IM, IPR, LLEH FORMAT (4I3) NOI Number of Gaussians IM Number of fixed parameters

Card Sequence	Information
2 (cont.)	IPR List control flag = 0 list of each iteration ≠ 0 list only final results
	LLEH Plot control flag = 1 read input card for plot parameters ≠ 1 code generates plot parameters
3	READ (5,40) (IX(I),I=1,IM)
	FORMAT (18I3)
	Indexes of fixed parameters
4	READ (5,45) (PG(I),I=1,7)
	FORMAT (6E12.7)
	The first seven parameters
	PG(1) standard deviation of the Gaussian
	PG(2) amplitude of the flat tail on the high-energy side of the Gaussian
	PG(3) amplitude of the sloped tail on the high-energy side of the Gaussian
	PG(4) slope for above exponential tail
	PG(5) amplitude of the flat tail on the low-energy side of the Gaussian
	PG(6) amplitude of the sloped tail on the low-energy side of the Gaussian
	PG(7) slope for the above exponential tail
5	READ (5,45) (PG(I),I=8,IA)
	FORMAT (6E12.7)
	Areas of the Gaussians
6	READ (5,45) (PG(I),I=IA,IB)
	FORMAT (6E12.7)
	Mean energies of the Gaussians

Card Sequence	Information
7	READ (5,45) PG(IK)
	FORMAT (E12.7)
	Rate of convergence of the exponential tails under the Gaussians
8	READ (5,30) (A(I),I=1,16)
	A(1) through A(8) label for the vertical plot axis
	A(9) through A(16) label for the horizontal plot axis
9	CALL DATA (X,Y,W,NODP)
	See previous section on DATA subroutine

Subroutine MAZCS

This subroutine is similar to the MAZGN subroutine discussed in Appendix A. The variables are generally the same, with the exception being the bounds and restrictions on the parameters to insure convergence.

One of two corrective actions is taken if a parameter tries to change sign during an iteration. Parameters 1, 4, 7, and the mean energies are fixed at their initial values, and all parameters are reinitialized if one of them tries to change sign. The just-calculated value for the parameter PC(I) is set to P(I)/2.0 if parameters 2, 3, 5, 6, or the Gaussian areas try to change sign. For the latter case, the sign checks are then continued.

The bounds on the parameters and the corrective action taken if a bound is violated are listed in Table 17.

TABLE 17

BOUNDS ON PARAMETERS MAZCS

Parameter	Bound	Corrective Action
1	None	
2	$>1.0 \times 10^{-4}$	Fixed at initial value All parameters reinitialized
3	$>1.0 \times 10^{-4}$	Same as 2
4	None	
5	Same as 2	Same as 2
6	Same as 2	Same as 2
7	None	
Areas	>X(N)/10000.0	Fixed at lower bound Checks continued
Energies	<X(N) & >X(1)	Same as 2

Subroutine OUTCS

Most of the output is generated by this subroutine. The initial value, best least-squares value, and the standard deviation associated with the fitted value are listed. In addition, the integrals under each of the sloped exponential tails are numerically determined. The sum of the Gaussian area and the two exponential tail areas associated with it are summed and listed. In many applications, this total area is more nearly the area of interest. The sum of the zero slope exponential tails on the low-energy side of all the Gaussians is calculated and also the corresponding sum on the high-energy side of Gaussians. The values are listed as the low-energy background and the high-energy background.

Subroutine PLTZ

This subroutine is quite similar to the PLOTGN subroutine listed and discussed in Appendix A.

Subroutine SITRE

The numerical integration that is used to determine the integral under the exponential tails is performed by this code. It assumes that 100 evenly spaced values for the dependent variable are stored as Y(I) and that X1 and X2 are the independent variables corresponding to Y(1) and Y(100). The cubic spline interpolation function is calculated, and the integral of this function between X1 and X2 is determined. The value of the integral is stored as SX in COMMON/LIMBO/. The cubic spline is discussed in Appendix E.

Subroutine YP

The variables in this subroutine are similar to the variables in the YP subroutine discussed in Appendix A. The function that is being fitted to the data, however, is quite different. The analytical function and its parameters are

$$Y(J) = \sum_{I=1}^{NOI} G(I,J) + HT(I,J) + LT(I,J) \quad ,$$

where NOI is the number of Gaussians in the energy region being analyzed. The J subscript refers to the Jth data point, and the I subscript refers to the Ith resonance. The Gaussian contribution to the function is

```
G(I,J) = P(I+7)*EXP(0.5*(PEP(I,J)/P(1))**2)/(0.39894*P(1))
PEP(I,J) = X(J)-P(I+NOI+7)    .
```

The high-energy exponential tails are

$$HT(I,J) = P(I+7)*(P(3)*EXP(P(4)*PEP(I,J)) + P(2))*CONV(I,J)*\delta(I,J)$$

$$CONV(I,J) = (1.0-EXP(-0.5*(PEP(I,J)*DUM)**2))$$

$$DUM = P(2*NOI+8)/(P(1)**2) \quad ,$$

$$\delta(I,J) = 1 \quad PEP(I,J) \leq 0.0$$
$$= 0 \quad PEP(I,J) > 0.0$$

Sample Problem

Input for a sample problem and the output from it are presented on the following pages. This code is available for distribution from the author and will be copied and sent to those wishing to use it.

SAMPLE

INPUT

FOR

GHLET CODE

```
  CARBON CROSS-SECTION   COMPOSITE DATA.
  3  6  0  1
  5  6  7  1 14  4
1.6       E+03.3       E-21.9       E-1-.18      E+00.0       E+C0.0       E+C
1.0       E+0
8.9       E+28.9       E+22.2       E+2
5.1       E+09.2       E+01.5       E+1
1.5       E+0
CROSS-SECTION  (MILLIBARNS)
HE3 ENERGY  (MEV)
  CARBON DATA.
    19

2.0       E+03.25      E+1
3.0       E+09.25      E+1
4.0       E+01.78      E+2
5.0       E+02.33      E+2
6.0       E+02.3       E+2
8.0       E+03.1       E+2
9.0       E+03.5       E+2
1.0       E+13.0       E+2
1.1       E+12.65      E+2
1.2       E+12.35      E+2
1.3       E+12.1       E+2
1.4       E+11.9       E+2
1.5       E+12.0       E+2
1.6       E+12.0       E+2
1.7       E+11.65      E+2
1.8       E+11.45      E+2
2.C       E+11.2       E+2
2.2       E+11.08      E+2
2.4       E+19.4       E+1
C.C       E+02.0       E+13.0       E+01.0       E+0       8
```

SAMPLE

OUTPUT

FOR

GHLET CODE

CARBON DATA.
CARBON CROSS-SECTION COMPOSITE DATA.

K	GUESS	CALCULATED	DEVIATION
1	1.6000000E+00	1.6000000E+00	0.
2	3.3000000E-02	3.3527851E-02	4.9919875E-03
3	1.9000000E-01	1.8968939E-01	3.1024785E-02
4	-1.8000000E-01	-1.8000000E-01	0.
5	0.	0.	0.
6	0.	0.	0.
7	1.0000000E+00	1.0000000E+00	0.
8	8.9000000E+02	8.7302791E+02	3.1286875E+01
9	8.9000000E+02	8.9928933E+02	6.3966439E+01
10	2.2000000E+02	2.2654831E+02	4.1462012E+01
11	5.1000000E+00	5.0581995E+00	9.9029291E-02
12	9.2000000E+00	9.1521487E+00	1.2109902E-01
13	1.5000000E+01	1.5548666E+01	3.7938159E-01
14	1.5000000E+00	1.5000000E+00	0.

ENERGY	LOW TAIL	GAUSSIAN	HIGH TAIL	TOTAL
5.058200E+00	1.210108E-26	8.730279E+02	6.382964E+02	1.511324E+03
9.152149E+00	1.246509E-46	8.992893E+02	6.574969E+02	1.556786E+03
1.554867E+01	3.140197E-27	2.265483E+02	1.656362E+02	3.921845E+02

LOW ENERGY BACKGROUND = 0.
HIGH ENERGY BACKGROUND = 6.701767E+01

12 ITERATIONS

WEIGHTED VARIANCE = 8.5444012E+01

NUMBER OF DATA POINTS FIT = 19

NUMBER OF GAUSSIANS = 3

I	WEIGHT	INDEPENDENT VARIABLE	DEPENDENT VARIABLE	CALCULATED FUNCTION	DEVIATION
1	1.0000000E+00	2.0000000E+00	3.2500000E+01	3.5045317E+01	-2.5453171E+00
2	1.0000000E+00	3.0000000E+00	9.2500000E+01	9.5306275E+01	-2.8062754E+00
3	1.0000000E+00	4.0000000E+00	1.7800000E+02	1.7617427E+02	1.8257303E+00
4	1.0000000E+00	5.0000000E+00	2.3300000E+02	2.2526821E+02	7.7317884E+00
5	1.0000000E+00	6.0000000E+00	2.3000000E+02	2.3913308E+02	-9.1330753E+00
6	1.0000000E+00	8.0000000E+00	3.1000000E+02	3.1126483E+02	-1.2648280E+00
7	1.0000000E+00	9.0000000E+00	3.5000000E+02	3.3673557E+02	1.3264433E+01
8	1.0000000E+00	1.0000000E+01	3.0000000E+02	3.1318003E+02	-1.3180035E+01
9	1.0000000E+00	1.1000000E+01	2.6500000E+02	2.6983392E+02	-4.8339191E+00
10	1.0000000E+00	1.2000000E+01	2.3500000E+02	2.2700056E+02	7.9994352E+00
11	1.0000000E+00	1.3000000E+01	2.1000000E+02	2.0363946E+02	6.3605416E+00
12	1.0000000E+00	1.4000000E+01	1.9000000E+02	1.9966175E+02	-9.6617450E+00
13	1.0000000E+00	1.5000000E+01	2.0000000E+02	1.9991358E+02	8.6417282E-02
14	1.0000000E+00	1.6000000E+01	2.0000000E+02	1.8816309E+02	1.1836913E+01
15	1.0000000E+00	1.7000000E+01	1.6500000E+02	1.7004126E+02	-5.0412639E+00
16	1.0000000E+00	1.8000000E+01	1.4500000E+02	1.5038322E+02	-5.3832211E+00
17	1.0000000E+00	2.0000000E+01	1.2000000E+02	1.2203875E+02	-2.0387532E+00
18	1.0000000E+00	2.2000000E+01	1.0800000E+02	1.0520763E+02	2.7923670E+00
19	1.0000000E+00	2.4000000E+01	9.4000000E+01	9.3661840E+01	3.3816039E-01

APPENDIX D

C24HE3P COMPUTER CODE

Sections of this code are similar or identical to the DECURA code discussed in Appendix A and the code discussed in Ref. 1. Those sections that are similar will not be discussed. This code is written in FORTRAN IV for the CDC 6600 computer.

Main Program C24HE3P

The masses and Q values for several reactions are defined. AM1 is the mass of the incident particle (^{3}He). AM3 is the mass of the light reaction product (proton). AM2(I) is the target mass for the Ith reaction. AM4(I) is the mass of the heavy product for the Ith reaction. GSQ(I) is the Q value for the Ith reaction. The reactions defined are listed in Table 18.

TABLE 18

REACTIONS DEFINED IN C24HE3P CODE

Index	Reaction
1	$^{12}C(^{3}He,p)^{14}N$
2	$^{13}C(^{3}He,p)^{15}N$
3	$^{14}N(^{3}He,p)^{16}O$
4	$^{15}N(^{3}He,p)^{17}O$
5	$^{16}O(^{3}He,p)^{18}F$
6	$^{17}O(^{3}He,p)^{19}F$
7	$^{18}O(^{3}He,p)^{20}F$

Subroutine DATAIN

One of the major modifications between this subroutine and the similar subroutine that was discussed in Ref. 25 is the number of regions that can be analyzed in a spectrum. Only one region is defined in each spectrum. The following upper bounds exist on variable storages: proton peaks - 20, data points analyzed - 512, and reactions - 10.

The bounds on the data region that is being fitted in the spectrum are controlled by the code. The lower bound will be CBLOW channels less than the peak channel of the lowest energy proton peak. The upper bound is the lesser of the peak channel number of the highest energy proton peak plus 13 and 512. Those channels containing zero counts are ignored.

Card Sequence	Information
1	READ (10,340) (TITLE(J),J=1,8)
	FORMAT (8A10)
	Identification information (80 BCD characters)
2	READ (10,280) NFOIL,FOILTH,CBLOW,SAM,IPUNF
	FORMAT (I6,3F12.0,I6)
	NFOIL Number of absorber foils between target and detector
	FOILTH Thickness of absorber foils (cm)
	CBLOW Number of channels to fit below the lowest energy proton peak
	SAM Lowest proton energy (after absorber foils) to be used in the fit
	IPUNF Punch output flag
3	READ (10,350) ICYCLE,MAXIT
	FORMAT (2I3)

Card Sequence	Information
3 (cont.)	ICYCLE = 0 Use just-calculated values as input for analyzing next set of spectral data. Read only ^{3}He energy from card input file.
	= 1 Complete set of input cards for next set of spectral data.
	MAXIT Maximum number of iterations before forced convergence
4	READ (10,350) NOI,IM,KEJ
	FORMAT (3I3)
	NOI Number of proton peaks
	IM Number of fixed parameters
	KEJ Number of free prompt gamma-ray energies
5	READ (10,350) (IXJ(L),L=1,K)
	FORMAT (24I3)
	These are the indexes of the fixed parameters
6	READ (10,285) PGAS(L),IREAT(L)
	FORMAT (F12.0,I6)
	PGAS(L) Prompt gamma-ray energy for the Lth proton peak
	IREAT(L) Reaction index for the Lth proton peak
7	READ (10,350) (KEEJ(L),L=1,M)
	FORMAT (24I3)
	These are the indexes of the free prompt gamma-ray energies
8	READ (10,355) (PG(J,L),L=1,9)
	FORMAT (6E12.7)
	These are the same nine parameters as defined in Ref. 1

Card Sequence	Information
9	READ (10,355) (PAS(L),L=1,NOII) FORMAT (6E12.7) These are the Gaussian areas as defined in Ref. 1
10	READ (10,300) CLCNN,N6,N7,N8,N9,N10,N11 FORMAT (E12.7,6I3) CLCNN Counts/C for the current integrator N6 through N11 Information on the tape identifying the first spectrum to analyze (m, d, y, h, min, and sec that the spectrum was dumped). For ICYCLE = 0, the first spectrum is searched for the above information. Subsequent spectra are analyzed in the order that they appear on the tape.
11	READ (10,290) EHE3 FORMAT (F12.0) Energy of the incident particles (MeV). This card is repeated for each additional spectrum that is to be analyzed under the ICYCLE = 0 option.
12	Additional card input is read in the PIONIZ subroutine. These are the inputs for the cubic spline functions used to represent X = f(E) and the inverse function E = f(X) for protons in the absorber foil material. Data is usually stored for proton energies from 1 to 12 MeV. READ (10,120) E(J),X(J),M(J),MI(J) FORMAT (4E12.5) E(J) Energy of proton (MeV) X(J) Depth in absorber material (cm) M(J) Second derivative of function (from cubic spline interpolation) MI(J) Second derivative of inverse function (from cubic spline interpolation)

Subroutine LSRMZ

Quite similar to the code discussed in Ref. 25. Some of the bounds and restrictions on the parameter value have been changed to ones that correspond to the resolution of the proton peaks.

Subroutine OUTRAN

Similar to other output subroutines. (See Ref. 25 and Appendix A.)

Subroutine PHICAL

See Ref. 25 and Appendix A.

Subroutine PIONIZ

This subroutine is used to calculate the proton energy losses in the absorber foils. The depth versus energy has been calculated for 12-MeV protons incident on a thick absorber foil. The resulting function and the inverse of this function are interpolated using cubic splines. These functions are then used in the code to calculate the energy losses in the absorber foil.

The function is first solved to determine the material depth to give the incident proton energy. The foil thickness is then added to this value of X, and the inverse function is evaluated at this sum. The result is the proton thickness after passing through the foil.

The more important variables used in this subroutine are listed in Table 19.

Subroutine PLTZ

This subroutine is similar to other plotting subroutines. (See Ref. 25 and Appendix A.) The left and right plot boundaries are fixed at 0.0 and 8.0.

TABLE 19

LIST OF VARIABLES IN PIONIZ SUBROUTINE

E(J)	Energy (MeV) of Jth interpolation point
FOILTH	Thickness of an absorber foil (cm)
L	Card input data flag, = 0 read new data, ≠ 0 use old data
M(J)	Second derivative of Jth interpolation point for the function X = f(E)
MI(J)	Second derivative of the Jth interpolation point for the inverse function E = f(X)
NFOIL	Number of absorber foils
NPTS	Number of interpolation points
X(J)	Depth in absorber to reach energy E(J) for the Jth interpolation point (cm)
YY	Absolute value of energy loss in the absorber foil
ZZ	Incident particle energy (MeV)

Subroutine PROMPT

This subroutine is used to calculate the prompt gamma-ray energy from the iterated least-squares energy for the proton. The kinematics equations solved are from Ref. 30. Both the relativistic and nonrelativistic equations are coded. The more important variables used in this subroutine are listed in Table 20.

Subroutine PRTNEY

This subroutine is used to calculate the proton energy for a given set of reaction parameters. The kinematics equations solved are from Ref. 30. The more important variables used in this subroutine are listed in Table 21.

TABLE 20

LIST OF VARIABLES IN PROMPT SUBROUTINE

I	Reaction index
EHE3	Incident ^{3}He energy
E3	Proton energy
EPG	Prompt gamma-ray energy
IRELV	= 0 use nonrelativistic equation
	= 1 use relativistic equation

TABLE 21

LIST OF VARIABLES IN PRTNEY SUBROUTINE

I	Reaction index
EHE3	Energy of incident ^{3}He particle (MeV)
E3	Proton energy (MeV)
EPG	Prompt gamma-ray energy (MeV)
AMZ(I)	Target masses (amu)
AM4(I)	Heavy product masses (amu)
AM1	^{3}He mass (amu)
AM3	Proton mass (amu)
GSQ(I)	Ground-state Q values (MeV)
EZ	Conversion factor (MeV/amu)
DETANG	Detector angle (°)

Subroutine YP

This subroutine is similar to other function subroutines. (See Ref. 25.)

Sample Problem

Input for a sample problem and the output from it are presented on the following pages. This code is available for distribution from the author and will be copied and sent to those wishing to use it.

SAMPLE INPUT FOR C24HE3P CODE

```
  CARBON CALIBRATION.  3 FOILS.  160 DEGREES.  26.12 MICRON/FOIL.
     3.002612       5.0          1.0                    0
   1  4C
  11   2   0
   6   8
13.0                  1
2.319                 1
3.952                 1
4.927                 1
5.117                 1
5.713                 1
5.885                 1
6.224                 1
6.468                 1
7.036                 1
7.974                 1
-.5465    E+05.2973    E+31.6725    E+1-.1058    E+36.9328    E+30.0       E+C
4.3289    E-5-.25      E+02.3253    E-4
3.1728    E+71.3878    E+72.4474    E+76.3022    E+63.3856    E+73.1248    E+7
1.0773    E+71.1920    E+75.6196    E+71.0       E+41.0       E+51.0       E+5
2.0       E-9   8 15 69   6 15 24
8.5931
 1.20000E+01 0.             0.             0.
 1.18000E+01 2.48401E-03-1.59881E-03-5.40932E+02
 1.16000E+01 4.93570E-03-1.11975E-03-4.19585E+02
```

SAMPLE INPUT FOR C24HE3P CODE (continued)

```
1.14000E+01  7.35492E-03-1.21219E-03-4.77690E+02
1.12000E+01  9.74157E-03-1.15648E-03-4.87151E+02
1.10000E+01  1.20956E-02-1.13688E-03-5.13319E+02
1.08000E+01  1.44169E-02-1.12099E-03-5.34597E+02
1.06000E+01  1.67054E-02-1.09915E-03-5.63202E+02
1.04000E+01  1.89609E-02-1.08240E-03-5.89701E+02
1.02000E+01  2.11833E-02-1.06626E-03-6.17553E+02
1.00000E+01  2.33725E-02-1.05756E-03-6.52883E+02
9.80000E+00  2.55283E-02-1.03350E-03-6.80473E+02
9.60000E+00  2.76507E-02-1.03344E-03-7.20821E+02
9.40000E+00  2.97395E-02-1.01274E-03-7.56217E+02
9.20000E+00  3.17946E-02-1.00562E-03-8.01729E+02
9.00000E+00  3.38158E-02-9.94793E-04-8.42688E+02
8.80000E+00  3.58030E-02-9.85208E-04-8.96692E+02
8.60000E+00  3.77560E-02-9.74373E-04-9.38917E+02
8.40000E+00  3.96748E-02-9.67298E-04-1.00568E+03
8.20000E+00  4.15591E-02-9.61435E-04-1.06107E+03
8.00000E+00  4.34088E-02-9.46961E-04-1.13182E+03
7.80000E+00  4.52237E-02-9.50720E-04-1.20207E+03
7.60000E+00  4.70037E-02-9.35159E-04-1.27365E+03
7.40000E+00  4.87487E-02-9.33644E-04-1.37699E+03
7.20000E+00  5.04583E-02-9.25264E-04-1.46413E+03
7.00000E+00  5.21324E-02-9.15301E-04-1.56625E+03
6.80000E+00  5.37709E-02-9.18532E-04-1.67613E+03
6.60000E+00  5.53736E-02-9.00569E-04-1.82674E+03
6.40000E+00  5.69401E-02-9.09191E-04-1.93904E+03
6.20000E+00  5.84704E-02-8.92668E-04-2.12363E+03
6.00000E+00  5.99641E-02-8.90137E-04-2.27833E+03
5.80000E+00  6.14211E-02-8.86786E-04-2.48356E+03
5.60000E+00  6.28411E-02-8.87720E-04-2.71149E+03
5.40000E+00  6.42238E-02-8.72333E-04-2.94435E+03
5.20000E+00  6.55690E-02-8.72949E-04-3.25640E+03
5.00000E+00  6.68763E-02-8.70872E-04-3.53848E+03
4.80000E+00  6.81456E-02-8.63563E-04-3.93047E+03
4.60000E+00  6.93765E-02-8.64877E-04-4.34488E+03
4.40000E+00  7.05687E-02-8.51928E-04-4.82466E+03
4.20000E+00  7.17219E-02-8.57409E-04-5.40127E+03
4.00000E+00  7.28357E-02-8.48435E-04-6.06647E+03
3.80000E+00  7.39097E-02-8.48850E-04-6.85786E+03
3.60000E+00  7.49435E-02-8.41164E-04-7.76000E+03
3.40000E+00  7.59367E-02-8.41495E-04-8.96202E+03
3.20000E+00  7.68887E-02-8.32858E-04-1.02051E+04
3.00000E+00  7.77992E-02-8.37074E-04-1.19793E+04
2.80000E+00  7.86675E-02-8.28847E-04-1.39865E+04
2.60000E+00  7.94931E-02-8.27540E-04-1.65847E+04
2.40000E+00  8.02754E-02-8.25995E-04-1.99023E+04
2.20000E+00  8.10137E-02-8.18481E-04-2.42665E+04
2.00000E+00  8.17072E-02-8.20081E-04-3.00132E+04
1.80000E+00  8.23552E-02-8.10694E-04-3.72597E+04
1.60000E+00  8.29567E-02-8.30145E-04-5.08730E+04
1.40000E+00  8.35107E-02-7.54228E-04-5.60891E+04
1.20000E+00  8.40161E-02-1.02344E-03-1.21224E+05
1.00000E+00  8.44714E-02 0.          0.
```

SAMPLE

OUTPUT

FOR

C24HE3P CODE

HOLLERT
BOND
50% COTTON
25%

CARBON CALIBRATION. 3 FOILS. 160 DEGREES. 28.12 MICRON/FOIL.

CARBON ACTIVATION CALLIBRATION RUN RUN 8

TOTAL CHARGE ON TARGET (COUL) = 1.2000E-04

DATE = 8/13/59 TIME = 6.15.24

DEAD TIME FACTOR = 1.00170

TOTAL COUNTS = 4853

LOST COUNTS = 76

CLOCK TIME = 24.1500 MINUTES.
NO SOLUTION. SET F4 TO 0.0.
XX GREATER THAN X(56).
XX GREATER THAN X(56).

REGION 1 HAS 1 SUBREGIONS
SUBREGION 1 IS CHANNEL 91 (1416.2 KEV) TO 371 (6099.2 KEV)

HELIUM-3 ENERGY = 8.5931 MEV

*	GUESS	CALCULATED	DEVIATION
1	-5.4650000E-01	-5.6807347E-01	4.4108800E-02
2	5.2973000E+03	5.4056465E+03	2.6208659E+02
3	1.5717757E+01	1.6721089E+01	1.1952637E-02
4	-1.0580000E+02	-1.0470599E+02	2.6973011E+00
5	1.2347385E+03	6.8193228E+03	3.6277675E+02
6	0.	0.	0. PHC
7	4.3289000E-05	4.3289000E-05	0. PHC
8	-2.5000000E-01	-2.5000000E-01	0. PHC
9	4.4857095E-05	4.4857095E-05	0. PHC

ENERGY (KEV)	CHANNEL NUMBER	GAUSSIAN AREA GUESSED	GAUSSIAN AREA CALCULATED	DEVIATION GAUSSIAN AREA	EXPONENTIAL TAIL TOTAL	TOTAL AREA GAUSS + EXP	DEVIATION GAUSS + EXP
5991.133	356.58	1.690215E+07	1.598748E+07	8.326710E+05	0.	1.598748E+07	8.326710E+05
4325.527	264.47	2.057543E+07	2.401215E+07	9.909681E+05	0.	2.401215E+07	9.909681E+05
3334.291	205.59	4.373166E+06	5.449722E+06	5.799770E+05	0.	5.449722E+06	5.799770E+05
3132.640	193.61	2.850413E+07	3.307724E+07	1.160973E+06	0.	3.307724E+07	1.160973E+06
2469.556	153.05	2.643670E+07	3.010494E+07	1.132894E+06	0.	3.010494E+07	1.132894E+06
2266.656	141.42	7.410759E+06	1.115001E+07	7.765497E+05	0.	1.115001E+07	7.765497E+05
1843.637	116.52	8.145887E+05	1.204973E+07	7.607839E+05	0.	1.204973E+07	7.607839E+05
1511.501	96.66	5.209179E+07	5.657105E+07	1.571116E+06	0.	5.657105E+07	1.571116E+06

17 ITERATIONS

WEIGHTED VARIANCE = 4.3523335E+00

ENERGY = 15.72107*CHANNEL + -104.706 KEV

NUMBER OF DATA POINTS FIT = 281

NUMBER OF LINES = 8

NUMBER OF FOILS = 3. FOIL THICKNESS = 26.1200 MICRONS.

HELIUM-3 ENERGY = 4.5931 MEV

INDEX	PROTON ENERGY CALC-MEV	GAMMA ENERGY GUESS-MEV	GAMMA ENERGY CALC-MEV	AREA COUNTS PER 10-6 COUL	FOIL ENERGY MEV	GROUND STATE Q-MEV
1	6.90370	2.31900	2.31900	15.98748	1.01257	4.77860
2	5.55364	3.95200	3.95200	24.01215	1.22792	4.77860
3	4.75650	4.92700	4.92700	5.44972	1.42102	4.77860
4	4.60210	5.11700	5.11700	33.07724	1.46942	4.77860
5	4.11999	5.71300	5.71300	30.10494	1.65044	4.77860
6	3.98154	5.88500	5.88500	11.15001	1.71489	4.77860
7	3.70946	6.22600	6.22600	12.04973	1.86602	4.77860
8	3.51480	6.46800	6.46800	56.57105	2.00330	4.77860

APPENDIX E

INTERPOLATORY CUBIC SPLINES

Interpolatory cubic splines were used to interpolate and smooth much of the data presented in this paper. The derivation of the equations necessary to do these interpolations is given below.

Figure 55 shows the initial assumptions for solving the cubic spline problem. Data have been obtained at $x_o,\ldots,x_{j-1},x_j,x_{j+1},\ldots,x_n$. It is assumed that the second derivative is linear between all x_{k-1},x_k, such that

$$\frac{d^2y}{dx^2} = M(x) = \frac{M_k(x - x_{k-1}) + M_{k-1}(x_k - x)}{h} \quad , \tag{1}$$

where $h = x_k - x_{k-1}$.

The above differential equation is solved using the following boundary conditions:

1) $\left.\frac{dy}{dx}\right|_{x_j,h_1} = \left.\frac{dy}{dx}\right|_{x_j,h_2}$

2) $y\Big|_{x_j,h_1} = y\Big|_{x_j,h_2}$

3) $y_{j-1} = f(x_{j-1})\Big|_{h_1}$

4) $y_{j+1} = f(x_{j+1})\Big|_{h_2}$

5) $\left.\frac{d^2x}{dy^2}\right|_{x_o} = 0$

6) $\left.\frac{d^2x}{dy^2}\right|_{x_n} = 0$

BASIC ASSUMPTIONS FOR CUBIC SPLINE

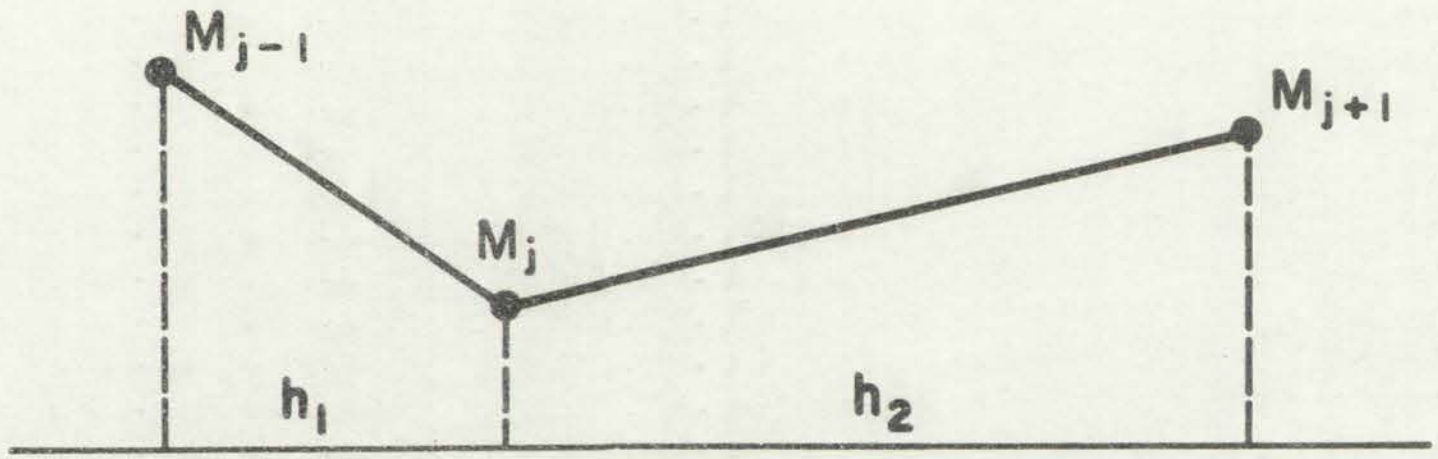

$$h_1 = X_j - X_{j-1}$$

$$h_2 = X_{j+1} - X_j$$

$$\frac{d^2y}{dx^2} = M(X) = \frac{M_j(X - X_{j-1}) + M_{j-1}(X_j - X)}{h_1}$$

Fig. 55. Basic assumptions for the cubic spline problem.

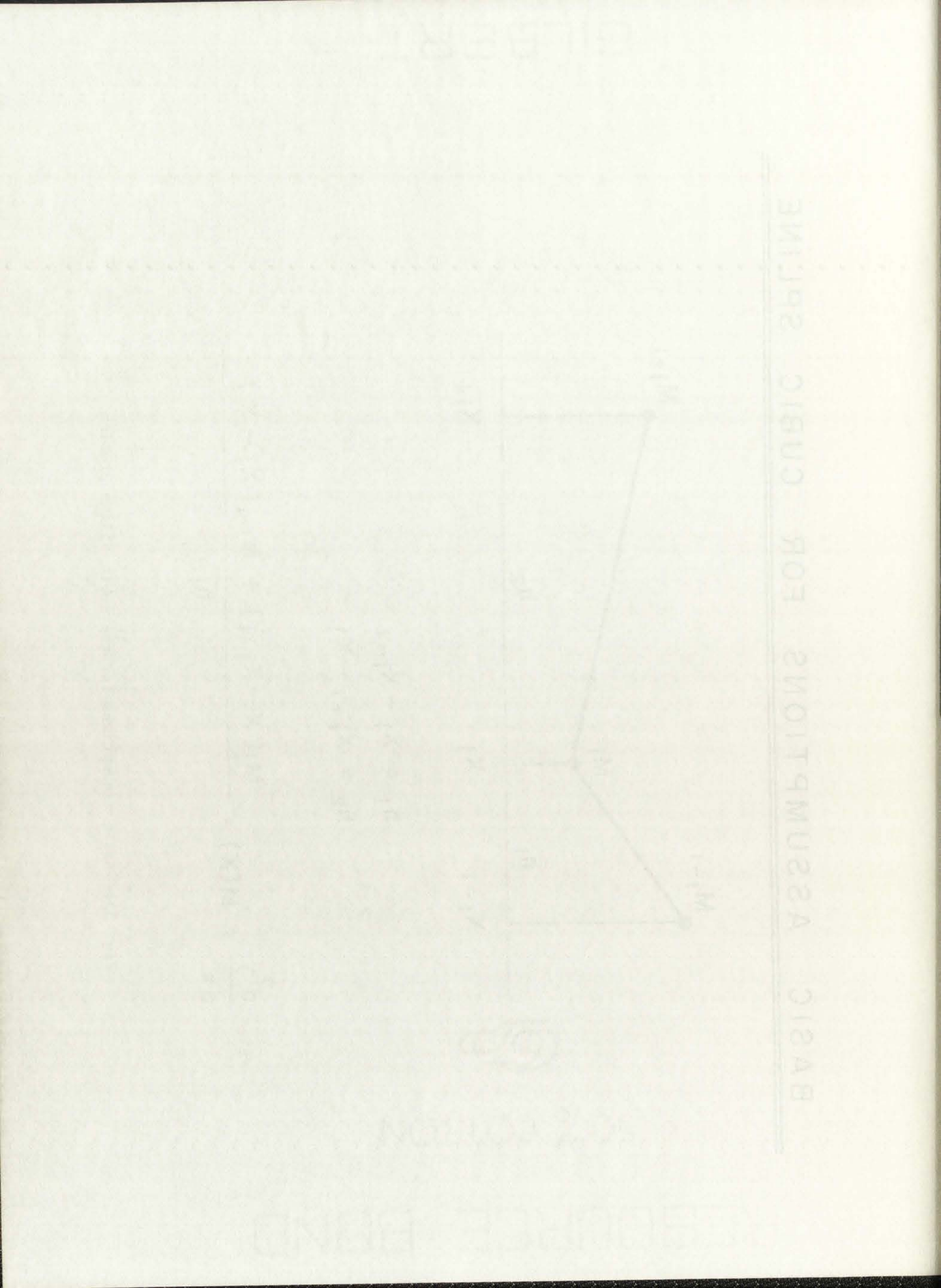
BASIC ASSUMPTIONS FOR CUBIC SPLINE

The solution of the above differential equation for n data points yields a set of equations that form a tridiagonal matrix which can be solved for M_j.

$$\frac{(y_j - y_{j+1})}{h_2} + \frac{(y_j - y_{j-1})}{h_1} = -\frac{M_j}{3}(h_1 + h_2) - \frac{M_{j-1}}{6} h_1 - \frac{M_{j+1}}{6} h_2 . \qquad (2)$$

x_j, y_j, and M_j can be used to calculate the value of the interpolation function, and also its first and second derivatives.

The corresponding values of $y(x)$, $y'(x)$, and $y''(x)$ for the interval between x_{j-1} and x_j are

$$y(x) = \frac{M_{j-1}(x_j - x)^3 + M_j(x - x_{j-1})^3 + (6y_{j-1} - M_{j-1} h^2)(x_j - x)}{6h}$$

$$+ \frac{(6y_j - M_j h^2)(x - x_{j-1})}{6h} , \qquad (3)$$

$$y'(x) = \frac{-M_{j-1}(x_j - x)^2 + M_j(x - x_{j-1})^2}{2h} , \qquad (4)$$

and

$$y''(x) = \frac{M_j(x - x_{j-1}) + M_{j-1}(x_j - x)}{h} . \qquad (5)$$

REFERENCES

1. R. J. Fox, "Lithium Drift Rates and Oxygen Contamination in Germanium," IEEE Transactions on Nuclear Science, Vol. NS-13, No. 3, pp. 367-369, 1966.

2. Samuel S. Markowitz and John D. Mahony, "Activation Analysis for Oxygen and Other Elements by Helium-3-Induced Nuclear Reactions," Analytical Chemistry, Vol. 34, No. 3, pp. 329-335, 1962.

3. Philippe Albert, "Rapport de Mission Aux Etats-Unis, Voyage d'etude au Lawrence Radiation Laboratory et Berkeley, du 2 Sept., au Oct. 1964,"--Directeur Scientifique au C.N.R.S. Laboratory de Radiochimie Analytique du Centre d'Etudes de Chimie Metallurgique 15, Rue Georges Urbain, Vitry-sur-Seine, France.

4. E. Ricci and R. L. Hahn, "Theory and Experiment in Rapid, Sensitive Helium-3 Activation Analysis," Analytical Chemistry, Vol. 37, No. 6, pp. 743-748, 1965.

5. Georges Amsel and David Samuel, "Microanalysis of the Stable Isotopes of Oxygen by Means of Nuclear Reactions," Analytical Chemistry, Vol. 39, No. 14, pp. 1689-1698, 1967.

6. J-C. Duclot, J. Giroux, L. Mazagol, L. Porte, M. Talvat, J-P. Thomas and J. Tousset," Analyse par Activation par Particles Chargees," Rapport Annuel, Institute de Physique Nucleaire, Lycen - 7101, pp. 74-75, 1971.

7. Dale M. Holm, John A. Basmajian and Wm. Mort Sanders, "Observation of the Microscopic Distribution of Oxygen and Carbon in Metals by He^3 Activation," Los Alamos Scientific Laboratory Report LA-3515, 1966.

8. Jack L. Parker and Dale M. Holm, "Measurement of Carbon Gradient in Stainless Steel by ^3He Activation and Autoradiography," Los Alamos Scientific Laboratory Report LA-4008, 1968.

9. J. A. Davies, "The Penetration of keV Projectiles in Solids," Atomic Energy of Canada Ltd. Report AECL-2757, 1967.

10. Charles Engelmann, "Sur 1'Utilisation des Particules α Pour 1e Dosage de 1'Oxygène et du carbon," Comptes Rendus, Vol. 258, pp. 4279-4281, 1964.

11. Harry L. Rook and Emile A. Schweikert, "Ultra-Trace Determination of Oxygen and Carbon by Charged Particle Activation Analysis," Analytical Chemistry, Vol. 41, No. 7, pp. 958-963, 1969.

REFERENCES - continued

12. Dale M. Holm, William L. Briscoe, Jack L. Parker, Wm. Mort Sanders and Sam H. Parker, "The Determination of Oxygen and Carbon in Germanium by ^{3}He Activation," Proc. 2nd Meeting on Practical Aspects of Activation Analysis with Charged Particles and Gamma Photons, pp. 239-259, Liege, Belgium, 1967. Published by EURATOM, EUR 3896 d-f-e, 1968.

13. Judith M. Gursky, Los Alamos Scientific Laboratory, private communication.

14. T. Gardiner and J. Levin, "The LASL Tandem Accelerator Facility Data System," IEEE Transactions on Nuclear Science, Vol. NS-13, No. 1, pp. 151-157, 1966.

15. J. S. Levin, M. P. Kellogg, R. B. Perkins and E. T. Ritter," Parasitic Use of an On-Line Computer-Based Data System," Proceedings for the Skytop Conference on Computer Systems in Experimental Nuclear Physics, CONF-690301, pp. 367-374, 1969.

16. S. T. Picraux and J. U. Andersen, "Measurements and Calculations of Critical Angles for Planar Channeling," The Physical Review, Vol. 186, No. 2, 1969.

17. C. Maples, G. W. Goth and J. Cerny, "Nuclear Reaction Q-Values," Nuclear Data, Section A, Vol. 2, pp. 429-612, 1966.

18. D. R. F. Cochran and J. D, Knight, "Excitation Functions of Some Reactions of 6 to 24 MeV ^{3}He Ions with Carbon and Aluminum," The Physical Review, Vol. 128, No. 3, pp. 1281-1286, 1962.

19. R. D. Evans, The Atomic Nucleus, McGraw-Hill Book Company, Inc., pp. 629-630, 1955.

20. T. Mankamo and P. Jauho, "Measurements of the Momentum Correlation in Three-Photon Annihilation of Positronium, "Nuclear Physics, Vol. A158, pp. 487-496, 1970.

21. R. W. P. Drever, A. Moljk and J. Scobie, "The Ratio of K-Capture to Positron Emission in Fluorine 18," The Philosophical Magazine, Vol. 1, No. 10, pp. 942-948, 1956.

22. F. Kover and M. J. Musselin, "A Comparative Study of Anodic Oxide Films on Titanium, Niobium and Tantalum," Thin Solid Films, Vol. 2, pp. 211-234, 1968.

23. J. A. Davies et al., "The Migration of Metal and Oxygen during Anodic Film Formation," Journal of the Electrochemical Society, Vol. 112, No. 7, 1965.

24. L. C. Northcliffe and R. F. Schilling, "Range and Stopping-Power Tables for Heavy Ions," Nuclear Data Tables, A7, pp. 233-463, 1970.

REFERENCES - continued

25. W. M. Sanders and D. M. Holm, "An Analytical Method for Unfolding Gamma-Ray Spectra," Los Alamos Scientific Laboratory Report LA-4030, 1969.

26. Hans Bichsel and Christoph Tschalaer, "A Range-Energy Table for Heavy Particles in Silicon," Nuclear Data, Vol. 3, No. 3, 1967.

27. C. H. Holbrow, R. Middleton and W. Focht, "Study of ^{14}N by Several Transfer Reactions," The Physical Review, Vol. 183, No. 4, pp. 880-887, 1969.

28. L. M. Polsky, C. H. Holbrow and R. Middleton, "Nuclear Structure of F^{18}," The Physical Review, Vol. 186, No. 4, pp. 966-977, 1969.

29. J. H. Ahlberg, E. N. Nilson and J. L. Walsh, The Theory of Splines and Their Applications, Academic Press, New York, New York 10003, 1967.

30. J. B. Marion, Ed., 1960 Nuclear Data Tables, Part 3, National Academy of Sciences, National Research Council, Washington, D. C., pp. 161-163, 1960.

31. Mark T. Robinson and Ordean S. Oen, "Computer Studies of the Slowing Down of Energetic Atoms in Crystals," The Physical Review, Vol. 132, No. 6, pp. 2385-2398, 1963.

32. Jens Lindhard, "Influence of Crystal Lattice on Motion of Energetic Charged Particles," Matematisk-fysiske Meddelelser, Vol. 34, No. 14, 1965.

33. Hans Henrik Andersen and Peter Sigmund, "A Simple Nonbinary Scattering Model Applicable to Atomic Collisions in Crystals at Low Energies," Matematisk-fysiske Meddeleser, Vol. 34, No. 15, 1966.

34. G. Dearnaley, I. V. Mitchell, R. S. Nelson, B. W. Farmery and M. W. Thompson, "Proton Channelling Through Thin Crystals," The Philosophical Magazine, Vol. 18, No. 154, pp. 985-1016, 1968.

35. Allan R. Sattler and G. Dearnaley, "Channeling in Diamond-Type and Zinc-Blende Lattices: Comparative Effects in Channeling of Protons and Deuterons in Ge, GaAs, and Si," The Physical Review, Vol. 161, No. 2, pp. 244-252, 1967.

36. W. M. Gibson, "The Role of Particle Channelling in Detector Systems," IEEE Transactions on Nuclear Science, Vol. NS-13, No. 3, pp. 162-175, 1966.

37. B. R. Appleton, C. Erginsoy and W. M. Gibson, "Channeling Effects in the Energy Loss of 3-11-MeV Protons in Silicon and Germanium Single Crystals," The Physical Review, Vol. 161, No. 2, pp. 330-349, 1967.

REFERENCES - continued

38. J. C. Poizat, J. Remillieux, V. Boninchi and R. Kirsch," Etude des Phenomenes de Canalisation," Rapport Annuel, Institut de Physique Nucleaire, Lycen-7101, pp. 79-86, 1971.

39. C. B. Finch and G. Wayne Clark, "Single-Crystal Growth of Thorium Dioxide from Lithium Ditungstate Solvent," Journal of Applied Physics, Vol. 36, No. 7, pp. 2143-2145, 1965.

40. Dale M. Holm and W. Mort Sanders, "Interference Reduction and Sensitivity Improvement in Activation Analysis," Nuclear Applications, Vol. 3, pp. 308-313, 1967.

41. R. H. Moore and R. K. Zeigler, "Solution of the General Least Squares Problem with Special Reference to High-Speed Computers," Los Alamos Scientific Laboratory Report LA-2367, 1959.

42. Marvin M. Hoffman, George J. Berzins, Wm. Mort Sanders, Leon J. Brown and Donald D. Phillips, "Neutron Scattering Cross Section of $^{197}_{79}Au$," Third Conference on Neutron Cross Sections and Technology, to be published in the proceedings, March 1971.

CURRICULUM VITAE

The author was born on a farm near Burlington, Kansas, on August 8, 1939. He graduated from Burlington High School in May 1957. He then attended Kansas State University, Manhattan, Kansas, and received the degree of Bachelor of Science in Nuclear Engineering in June 1961.

The author was employed by the Aerophysics Group at General Dynamics/ Astronautics in San Diego, California, from June 1961 until May 1962. From May 1962, until the present, the author has been employed by the Los Alamos Scientific Laboratory of the University of California. While at Los Alamos, he worked with the Fast Reactor Division until October 1969 when that project was terminated due to restrictions on government spending. Since then, the author has worked with the Nuclear Test Division.

The author is married to the former Claudia Faye Ewing and has two sons, William Duward and Jeffrey Raymond.

The author received the Master of Science degree in Nuclear Engineering from the University of New Mexico in June 1966 through the Los Alamos Graduate Center of the University of New Mexico.

The author studied on the campus at the University of New Mexico during the 1967-1968 school year supported by the Advanced Study Program of the Los Alamos Scientific Laboratory.

He is a member of Sigma Tau (engineering honorary) and Phi Eta Sigma (scholastic honorary).